MOLECULAR DYNAMICS SIMULATIONS OF SUPERCOOLED WATER IN SOLUTIONS WITH PERCHLORATES:

The Effect of Martian Solutes on Thermodynamics and Structure

Dipartimento di Matematica e Fisica
Dottorato di ricerca in Fisica

Paolo La Francesca

Docente guida	Coordinatore
Prof.ssa Paola Gallo	Prof. Giorgio Matt

Ciclo XXXVI

Paolo La Francesca: *Molecular Dynamics Simulations of Supercooled Water in Solutions with Perchlorates: The Effect of Martian Solutes on Thermodynamics and Structure,* Tesi di dottorato in Fisica, © 2024.

Parte di questi risultati sono pubblicati in La Francesca and Gallo, 2023 e parte pianificati per la pubblicazione in La Francesca and Gallo, 2024.

CONTENTS

III MAGNESIUM PERCHLORATE IN AQUEOUS SOLUTIONS

IV CONCLUSIONS

V APPENDIX

Bibliography

LIST OF FIGURES

LIST OF TABLES

ACRONYMS

LLCP	Liquid Liquid Critical Point
LDL	Low-Density Liquid
HDL	High-Density Liquid
MD	Molecular Dynamics
TMD	Temperature of Maximum Density

TmD	Temperature of Minimum Density
LG-LMS	Liquid-Gas Limit of Mechanical Stability
LDA	Low-Density Amorphous
HDA	High-Density Amorphous
VHDA	Very High Density Amorphous
RDF	Radial Distribution Functions
ST2	Stillinger and Rahaman potential
SPC	Simple Point Charge
SPC/E	Simple Point Charge Extended
TIP4P	Transferable Intermolecular Potential with Four Points
TIP4P/2005	Transferable Intermolecular Potential with Four Points

I'm so ignorant now with all that I've learnt.

— Black Country, New Road

RINGRAZIAMENTI

> *"There was a button," Holden said. "I pushed it."*
> *"Jesus Christ. That really is how you go through life, isn't it?"*
>
> — James S.A. Corey, Nemesis Games

Un primo sincero ringraziamento va alla mia supervisor, la professoressa Gallo, per i suoi preziosissimi consigli, per avermi trasmesso l'interesse per il suggestivo campo di ricerca dell'acqua sottoraffreddata, per il sostegno e i suggerimenti fornitimi in questo corso di studi.

Grazie anche alla mia famiglia, per avermi sostenuto in questi tre anni.

Tre anni che sembrano tre epoche diverse: un primo anno in piena pandemia, un secondo anno con restrizioni che andavano e venivano, un terzo anno segnato da uno strano e poco credibile ritorno alla normalità... e fondamentalmente penso che il 90% dei dottorandi degli ultimi tre cicli debba un riconoscimento a Marco, ancora di salvezza dell'81, nonché praticamente l'unico di noi ad aver conosciuto il mondo accademico pre-COVID e senza di cui nessuno tra noi avrebbe neanche saputo come dottorarsi. Grazie, senza alcun ordine particolare, anche a Romy per i suoi scambi di idee per nulla impegnativi, per le caramelle fantastiche e per avermi insegnato a raggiungere a piedi posti che nemmeno credevo appartenessero a un insieme semplicemente connesso. Grazie a Massimo e Giulia (*Giulia*) per gli innumerevoli passaggi a casa e per il fantamorto, a Matteo per i caffè insieme e per le discussioni su quanto andava male la Ferrari, a Raul per tutti i kebab che abbiamo preso (e anche per quelli che non abbiamo preso), a Sacha per le partite a beach volley, a Maxime e Vittoria anche se sono palesemente degli agenti sotto copertura dei servizi segreti francesi, a Cintia e Leo per i preziosi aiuti. Grazie a Gabriele, Daniele e Roberto, malgrado - sappiate - fingerò di non conoscervi quando l'esercito della cancel culture sarà venuto a prendervi (sotto mia indicazione). Grazie a Simone anche se dovrebbe smetterla di credersi il brasiliano, ad Andrea per le innumerevoli cose che mi ha fatto apprendere contro la mia volontà, a Betta per le sue storie fantastiche e dove trovarle (sugli aerei, apparently), a Ivano che ha provato a convincermi a fare la traversata dello stretto di Messina, fallendo miseramente. E grazie a Lorenzo, Silvia, Rita, Dario, Francesca, Alessio, Filippo, Nina, Chloe e a tutti gli altri dottorandi per i pranzi insieme, le (fin troppo poche) giornate al mare, le partite a carte e i biscotti dell'acquario per spezzare le interminabili (per qualcuno letteralmente, visto che ci è rimasto chiuso dentro) giornate di studio e di lavoro in via della Vasca Navale.

Un particolare ringraziamento va agli amici conosciuti dentro e fuori l'università, a Ada per i suoi fondamentali consigli anche su roba di cui in teoria non sapeva niente, a Luca e Francesco, quando non mi ghostano, a Seb e Mauro, anche se ci siamo visti troppo poco, a Angelo e Vito le cui frequenti chat di gruppo hanno reso sopportabili gli anni di pandemia e con cui spero potremo rivederci dal vivo più spesso, a Elga per le pizze insieme da Mangianapoli, ai cornetti e ai miei coinquilini per questi ultimi due anni in cui hanno dovuto sopportare la mia musica e le partite di Formula 1 ad alto volume.

Roma, 31 gennaio 2024
Paolo

1

INTRODUCTION

Water features an outstanding variety of anomalies which are more pronounced when supercooled.

Primarily due to the significant number of unexplained anomalies it exhibits, the study of the structural and the thermodynamic behaviour of water is one of the most interesting topics in contemporary statistical mechanics and condensed matter physics (Gallo et al., 2016; Gallo and Stanley, 2017; Angell, 1983; Debenedetti, 2003; Gallo and Rovere, 2021).

By investigating the thermodynamic response functions it was experimentally observed that these anomalies are even more prominent when water is supercooled, i.e., when maintained in the liquid form below its freezing temperature.

However, as the water-ice transition is first order (Parisi, 1998; Debenedetti, 1996), it is exposed to all the challenges associated with nucleation (Debenedetti, 2003). Supercooled water, indeed, exists in a metastable state, and, when a thermal fluctuation within the system is large enough to overcome the free energy barrier separating the metastable and the stable state, the homogeneous nucleation takes place (Parisi, 1989, 1992).

Nucleation makes the supercooling process experimentally challenging, hence the crucial role of simulations.

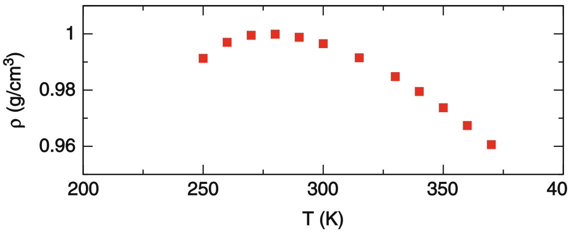

Figure 1.1: Density of water at ambient pressure. The presence of a maximum represents one of the most famous anomalies. Picture adapted from Gallo and Rovere, 2021.

The presence of impurities makes the nucleation process accelerate as water molecules order more easily around them, effectively reducing the aforementioned barrier (Debenedetti, 2003) and hence causing the nucleation. For this reason, considerable efforts were put over the years into purifying experimental water samples used to study the supercooled phase (Mishima, 1996; Kanno et al., 1975; Tombari et al., 1999; Krämer et al., 1999, 1996).

Besides impurities, another significant challenge is posed by the existence of a region of water's phase diagram where homogeneous nucleation occurs too quickly for water to be supercooled. This region is known as *no man's land*.

Recently the boundaries of the no man's land have been found to be narrower than previously estimated (Kim et al., 2017, 2020; Seidl et al., 2015) and it is known that no thermodynamic constraints prevent liquid water to reach the glassy state through supercooling (Speedy et al., 1996). Nonetheless, due to the challenges posed by the emergence of homogeneous nucleation, numerical simulations (Allen and Tildesley, 2017) keep playing a crucial role in understanding the unique behaviour of water to date.

Indeed, the onset of homogeneous nucleation is a kinetic limitation linked to the experimental times of observation exceeding the time taken by water to crystallise. To address this issue, numerical simulations can implement faster cooling rates that allow to explore the whole supercooled region of water.

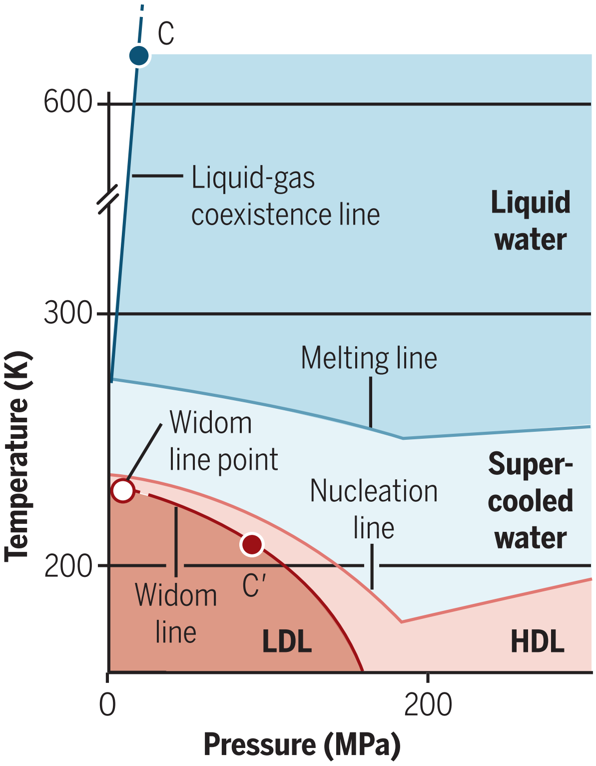

Figure 1.2: Schematic phase diagram of non-crystalline water. Figure from Gallo and Stanley, 2017.

The prevailing explanation for water anomalies, supported by numerical simulations, centres around the hypothesis of existence of a second-order Liquid-Liquid Critical Point.

Moreover, in this context, molecular dynamics (MD) simulations have been pivotal in the development of theories that offer explanations for the anomalies of water: the prime instance of these is provided by the formulation, by Poole, Sciortino, Essmann and Stanley [1992], of the hypothesis that water anomalies emerge due to the existence in the no man's land of a second-order liquid-liquid critical point (LLCP). This hypothesis, grounded in the results derived from MD simulations performed on the water-like ST2 potential (Stillinger and Rahman, 1974), is currently by far the most widely credited explanation for the anomalies of water.

The LLCP scenario predicts that below the critical temperature two separate phases of water are supposed to exist: high-density and low-density liquid (HDL and LDL), which in turn develop upon heating from the already known glassy phases (HDA and LDA), and they are separated by a first-order line of phase transitions, the HDL-LDL coexistence curve. This curve's prosecution in the one-phase region is the Widom line, a line of state points on which the correlation length maxima lie. This line is emanated from the LLCP and the lines of maxima of the thermodynamic response function converge to it close to the critical point.

The LLCP hypothesis has been rigorously confirmed for the ST2 model (Palmer et al., 2014; Liu et al., 2012, 2009; Sciortino et al., 2011; Kesselring et al., 2013; Smallenburg and Sciortino, 2015), for the Jagla model (Gallo and Sciortino, 2012), a short-range potential for water (Jagla, 2001) and for the most realistic numerical water potentials: TIP4P/2005 (Abascal and Vega, 2005) and TIP4P/Ice (Abascal et al., 2005) by Debenedetti, Sciortino and Zerze [2020]. In the specific case of TIP4P/2005, simulations performed in Debenedetti et al., 2020 have located the LLCP at $T_C = 172\,\mathrm{K}, p_C = 186\,\mathrm{MPa}$ and established the phase transition occurring in its correspondence to be of the same universality class as the Ising model, as previously found for the ST2.

Remarkable experimental evidence supporting the LLCP hypothesis has been provided (Kim et al., 2017, 2020; Mishima and Stanley, 1998a; Woutersen et al., 2018; Winkel et al., 2011).

Water is often easier to supercool in solutions.

The computational research on supercooled water behaviour has given particular attention to aqueous solutions (Corradini et al., 2010, 2012), due to their common occurrence in nature and to water being often easier to supercool in them. Importantly, for instance, MD simulations on aqueous solutions of NaCl have shown the LLCP shifting to higher temperatures and lower pressures upon increasing the solute concentrations (Corradini et al., 2011), indicating that more physically accessible conditions for studying the liquid-liquid transition are achievable.

Perchlorate solutes and the potential role of water anomalies on the presence of liquid water on Mars

Within this context, this work will focus on aqueous solutions of sodium perchlorate ($NaClO_4$) and magnesium perchlorate ($Mg(ClO_4)_2$). These solutions are currently of great relevance, as their behaviour is considered to provide an explanation for the recent detection on Mars through dielectric permittivity measurements of unusually bright basal reflections, connected to the existence of liquid water underneath the Martian South Pole surface (Orosei et al., 2018; Lauro et al., 2021). Perchlorates are known to be abundant on Mars and recent experiments have also shown that supercooled aqueous perchlorate solutions can remain liquid down to 150 K (Toner et al., 2014).

The aim of this PhD thesis was to determine what role water anomalies can play on the presence of liquid water on Mars and assess if, how and to what extent the unique properties of water are retained upon increasing the concentrations of the solutes. To do so, the thermodynamic and structure of aqueous solutions of sodium perchlorate and magnesium perchlorate was explored with MD simulations.

In particular:

CHAPTER 2 outlines the research context, focusing on the characteristics of the water molecule and its hydrogen bond network. It explores the stability and metastability of liquid water, particularly in the supercooled domain. Key anomalies of water are detailed, followed by a discussion on theoretical models for their occurrence, emphasising the Liquid-Liquid Critical Point (LLCP) theory, pivotal to the presented results. Finally, properties of solutions relevant to this study are presented.

CHAPTER 3 focuses on the essential aspects of the MD technique in the microcanonical ensemble. It introduces MD's fundamental principles, then details integration algorithms and the use of thermostats for canonical ensemble simulations. The chapter also covers the force-fields for water. Among these is the TIP4P/2005 employed in this thesis.

CHAPTER 4 outlines the simulations' general methodology, emphasising the strategies implemented, including generating the initial conditions based on the chosen concentrations for the system alongside a description of the potentials used. It then presents thermodynamic findings for sodium perchlorate solutions at 1.63 wt% and 15.4 wt%, detailing estimations of the temperature of maximum and minimum density curves, isothermal compressibility peaks with the estimated position of the Widom Line, and the boundary of liquid-gas limit of mechanical stability (LG-LMS). The chapter then shows the phase diagrams in the supercooled region extrapolated from the simulations and concludes with schematic phase diagrams for the two solutions to focus on the changes on the interplay between LDL and HDL upon increasing the concentration and with respect to the bulk.

IN CHAPTER 5 a structural analysis of the sodium perchlorate aqueous solutions is undertaken through the examination of the water-water, ion-ion, and ion-water radial distribution functions (RDFs), along with the study of first-shell coordination numbers for the water-water interaction. This analysis demonstrates the ions' effects on the interplay between the HDL and the LDL phases of the system.

CHAPTER 6 presents the thermodynamic results for aqueous magnesium perchlorate solutions, alongside a description of the potential used and the key differences from sodium perchlorate. By estimating the position of the system's density anomaly region, the peaks of isothermal compressibility and the LG-LMS, the phase diagram of solutions at concentrations of 2.95 wt% and 24.4 wt% is calculated. The chapter concludes with a comparison of the thermodynamic results obtained from the four studied solutions.

CHAPTER 7 presents the structural results of the aqueous solutions of magnesium perchlorate by mean of the water-water, ion-water and ion-ion RDFs and the first-shell coordination numbers for the water-water interaction. A structural comparisons among the four solutions concludes the chapter.

CHAPTER 8 summarises the results for the four systems.

All the simulations were performed using GROMACS (Hess et al., 2008) on the *GRID-Roma Tre cluster*, employing the potentials defined in Nieszporek et al., 2016; Agieienko et al., 2014 and the TIP4P/2005 model of water (Abascal and Vega, 2005). A total number of 2937 state points were studied. The total single-CPU computation time was approximately 100 years. I personally coded the algorithms applied to carry out the data analysis of the systems. The graphs were generated using gnuplot (Williams and Kelley, 2023). System snapshots were graphed using VMD (Humphrey et al., 1996).

Part I

NUMERICALLY EXPLORING AQUEOUS SOLUTIONS: ANOMALIES OF WATER AND COMPUTATIONAL METHODS

2

SUPERCOOLED WATER AND AQUEOUS SOLUTIONS

2.1 STABLE WATER

The water molecule (Fig. 2.1) is a V-shaped and planar molecule, consisting of an oxygen atom at its centre and two hydrogen atoms at its outer vertices. The O–H distance is 0.09578 nm while the central angle is 104.5° (Császár et al., 2005; Hasted, 1972).

Oxygen and hydrogens form a covalent bond. The orbitals of the oxygen atom, whose outer shell is made up of six electrons, undergo hybridisation, leading to four equivalent sp^3 orbitals: two of which accommodate lone pairs, each consisting of two electrons while the other two form sigma bonds with the two hydrogen atoms. The sp^3 hybridisation results in a tetrahedral structure among the oxygen, the two hydrogens and the two lone pairs. Due to its high electronegativity, the oxygen exerts a strong attraction toward the electron that the hydrogen shares with it. Because of this, the hydrogen partially exposes the nucleus and the water molecule is polar. For this reason the hydrogen is often referred to as 'protonated' and we can attribute partial charges of approximately $\delta q \approx -0.7e$ for the oxygen atom and $\delta q \approx +0.35e$ for each hydrogen atom (Martin and Zipse, 2005).

Lone pairs can form so-called *hydrogen bonds* with the hydrogen atoms of neighbouring water molecules, while protonated hydrogens can attract lone electron pairs from an adjacent water molecule's oxygen, thereby creating a network of intermolecular interactions (Gallo and Rovere, 2021). Each water molecule can engage in four hydrogen bonds, two as a donor and two as an acceptor, resulting in a tetrahedral arrangement of hydrogen bonds around the central oxygen atom (Fig. 2.2).

At ambient temperature, the estimate of the energy associated with the hydrogen bond is about 20 kJ/mol. Notably, the energy associated with dipole-dipole interactions is considerably lower, around 1 kJ/mol. As a result, the hydrogen bond stands out as a relatively strong force in liquid phases, despite being markedly weaker than covalent bonds, which usually have an energy close to 400 kJ/mol.

2.1.1 *The Phase Diagram of Stable Water*

Figure 2.3 shows the phase diagram of stable water. When compared to most substances, water can be found in a liquid phase for a very wide range of temperatures and pressures, including ambient conditions $T = 300\,\text{K}$ and $p = 1\,\text{atm}$.

In the liquid state near the melting point, the local tetrahedral symmetry discussed in the previous section is only partially maintained, with

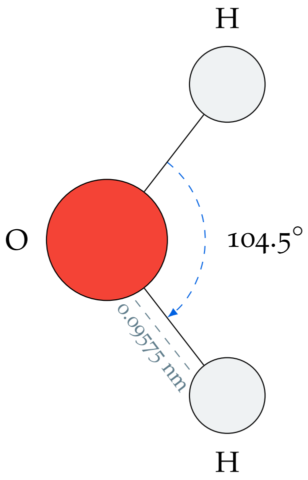

Figure 2.1: A water molecule.

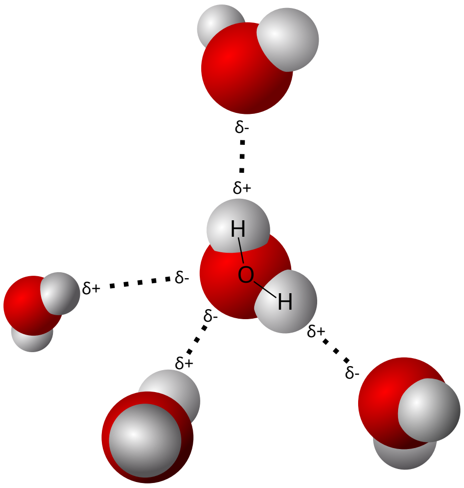

Figure 2.2: The tetrahedral hydrogen bond network locally formed by water.

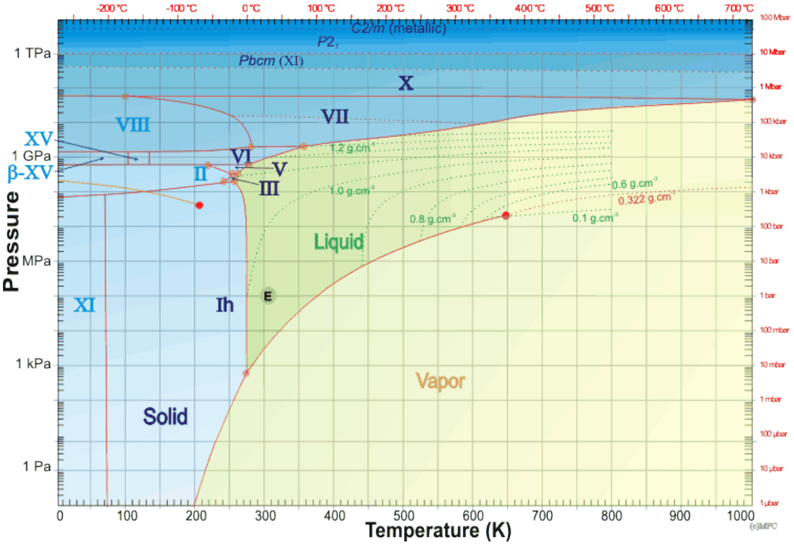

Figure 2.3: Phase diagram of the stable phases of water. Picture from Chaplin, 2022.

short-range order. As a result of this, the liquid form of water exhibits a higher density compared to its crystalline (ice) state, representing one of the most well-known anomalies of water, related to the *density anomaly* (see also Sec. 2.4).

This feature is highlighted by the negative slope of the coexistence line between the liquid and the solid phases, for which the Clausius-Clapeyron equation

$$\frac{dp}{dT} = \frac{1}{T}\frac{\lambda}{\Delta V}$$

implies, λ being the latent heat of fusion, its increase in volume upon freezing.

Another important feature of water is its polymorphism (Bachler et al., 2019). If the temperature is lowered below 273.15 K, the solid phase is the ice I_h but this is not the only solid phase of water existing. Up to today, nineteen stable and four metastable crystalline phases are known (Debenedetti, 2003; Chaplin, 2022; Petrenko and Whitworth, 1999; Salzmann et al., 2009).

2.2 METASTABILITY, SUPERCOOLING AND NUCLEATION

Phase transitions (Parisi, 1998) constitute a collective change in the behaviour of a system with a high number of particles and are perhaps the most important example of critical phenomena in condensed matter physics.

The water-to-ice transition that occurs at $T_F = 273.15$ K under standard atmospheric pressure is arguably the most familiar example of a first-order phase transition. This classification refers to transitions involving a latent heat and a sudden change in the system's energy landscape and can be identified by a discontinuity in the first derivative of the free energy.

The main features that characterise first-order phase transitions are:

- discontinuities in several thermodynamic quantities (such as the density or internal energy in the case of water);

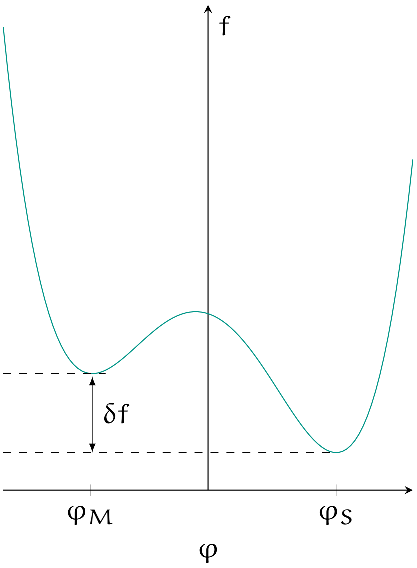

Figure 2.4: Schematic example of a free-energy density function exhibiting a metastable and a stable state as a function of one order parameter.

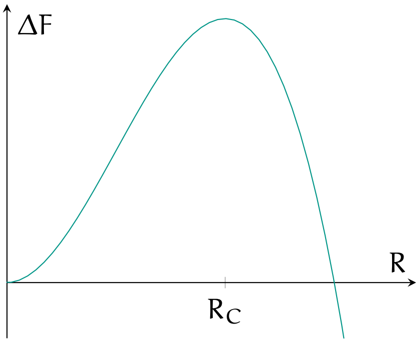

Figure 2.5: Free energy and the critical radius.

- the lack of precursor signs, meaning the change occurs without any gradual transformation or early indicators in the system's properties;
- the ability, possibly with highly accurate procedures, to bring the system into a metastable state, that is, a state with a (potentially very) long life time which is mechanically stable but not in a state of thermodynamic equilibrium.

Supercooled Water

Water stands out among the systems that exhibit metastability: it can retain its liquid state at temperatures below its freezing point. This phenomenon is referred to as 'supercooling'.

A metastable state is a local minimum point of the free energy.

From the perspective of statistical mechanics, a metastable state is a local minimum in the free energy landscape as a function of the degrees of freedom.

2.2.1 *Nucleation*

As a function of the order parameter, when known, an example of free energy of a system with a stable and a metastable state can be shaped as in figure 2.4.

Upon crossing a first-order phase transition, a system generally does not instantly transition into a new stable phase. Instead, the former stable state becomes metastable and thermal fluctuations favour the formation of nuclei of the stable phase within the metastable state (Parisi, 1992). Considering the system's total free energy, the new stable phase is naturally preferred. However, the free energy balance of a stable spherical bubble of radius R is expressed as:

$$\Delta F = -\delta f \cdot V(R) + \delta F_I(R), \tag{2.1}$$

where δf is the free energy density difference between the stable and the metastable minima, $V(R) \sim R^D$ is the volume of the bubble and the interfacial free energy $\delta F_I(R)$ can grow at most as (Cavagna, 2009):

$$\delta F_I(R) = O(\sigma \cdot \Sigma(R)),$$

with σ being the surface tension and $\Sigma(R) \sim R^{D-1}$ describing the surface area of the bubble.

Therefore, for minor fluctuations, resulting in smaller values of R, the free energy of the stable state initially increases until a critical radius R_C is reached (Fig. 2.5). By differentiating the eq. (2.1), this radius can be obtained from the maximum of ΔF using the equation

$$(D-1)\,\sigma\, {R_C}^{D-2} - D\,\delta f\, {R_C}^{D-1} = 0$$

providing

$$R_C = \frac{D-1}{D}\frac{\sigma}{\delta f}$$

from which we can determine the homogeneous nucleation barrier

$$\Delta F_C \sim \frac{\sigma^D}{\delta f^{D-1}}.$$

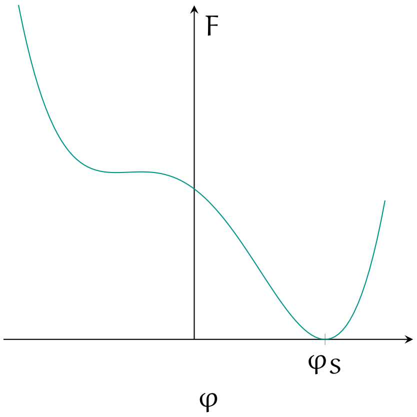

Figure 2.6: Schematic example of a free-energy function exhibiting a spinodal.

The probability of the necessary fluctuation for nucleation to occur can be determined by the Arrhenius law

$$P \sim e^{-\beta \Delta F_C}. \tag{2.2}$$

The nucleation time

$$\tau \sim e^{\beta \Delta F_C} \tag{2.3}$$

can vary significantly depending on the specific characteristics of the system being considered and potentially be very long.

When the temperature changes, so does the shape of the free energy and therefore the metastable state can disappear: the state point of the system where this happens is called spinodal (Fig. 2.6).

The role of impurities

Impurities can reduce the nucleation time by providing a surface for crystals to form on (Debenedetti, 2003). This can reduce the free energy barrier ΔF_C.

For example, when water freezes, it usually nucleates more easily on dust particles or other impurities in the water.

2.2.2 *Second-Order Phase Transitions*

In second-order phase transitions (Parisi, 1998, 1989), also known as continuous transitions, at the critical temperature T_C the internal energy is continuous, hence there is no latent heat, while the specific heat is singular. There are precursor signs and no trace of metastability. The prime example of a second-order transition is the ferromagnetic transition, and the prototype model in theoretical physics exhibiting such a transition is the Ising model (see for example Parisi, 1998).

The precursor phenomena of second-order transitions are related to the singular behaviours of the response functions near the critical point. These behaviours are linked to the existence of a correlation length ξ within the system and to its thermal fluctuations: at $|T - T_C| \gg 0$ the connected correlation functions of the system have a local behaviour $G(r) = f(r/\xi)$, such as

$$G(r) \sim e^{-r/\xi},$$

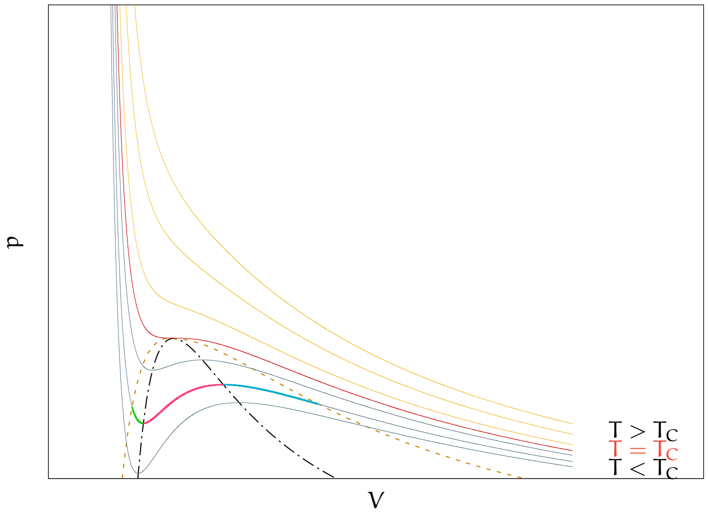

Figure 2.7: Generic system undergoing a phase transition in the van der Waals theory. The critical isotherm is highlighted in red. In the multi-coloured isotherm below T_C the metastable states are highlighted in green and cyan. Purple-coloured is the nonphysical curve.

while they are scale-invariant at the critical point

$$G(r)|_{T=T_C} \sim r^{-(D-2+\eta)},$$

D being the dimension of the system.

Near the critical point, the fluctuations start correlating over progressively larger scales, ultimately diverging at the critical point itself. The correlation length exhibits a singular behaviour as it approaches the critical temperature T_C, described by

$$\xi \sim T \to T_C (T - T_C)^{-\nu}.$$

As a consequence, several thermodynamic quantities exhibit a power-law singular *critical* behaviour near the critical point. In the case of ferromagnetism, for example, the magnetic susceptibility for $T \to T_C$ behaves as:

$$\chi \sim (T - T_C)^{-\gamma}.$$

Here, ν, η and γ are examples of *critical exponents*.

Due to the divergence of the correlation length, the specific details of the system at the critical point become irrelevant: systems apparently very different from each other can have the same critical behaviour, i.e. the same critical exponents, and are said to belong to the same *class of universality*.

2.2.3 *Mechanical Stability*

We now focus on a generic system undergoing a second-order phase transition in the van der Waals theory at a critical temperature T_C. In Fig. 2.7 the critical isotherm is shown in red, the isotherms at $T > T_C$ are shown in yellow and those at $T < T_C$ are shown in grey.

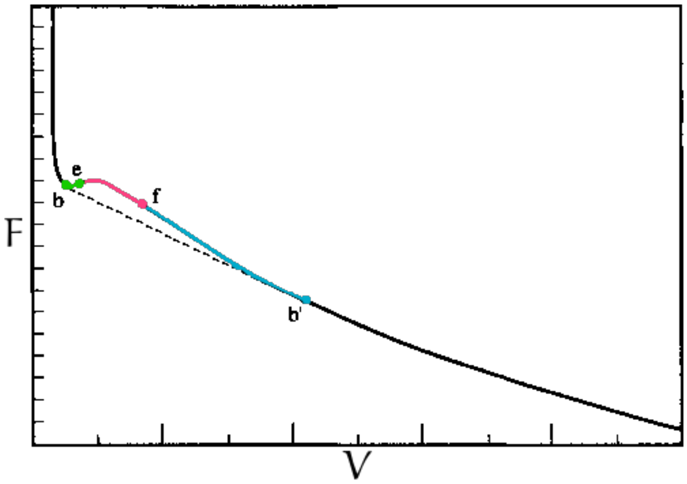

Figure 2.8: Helmholtz free energy of a generic system in the van der Waals theory at $T < T_C$. Figure adapted from Debenedetti, 1996.

While the stable behaviour, which in this work we are *not* interested in, would be obtained by the Maxwell construction, the metastable phases are those in the two areas on either side of the critical point delimited by the dotted and the dash-dotted curves.

For clarity, one of the isotherms below T_C has been highlighted with different colours. Two stable phases (one on each side, grey-coloured) exist outside the dashed orange coexistence curve. The green and the cyan arcs represent metastable phases. The minimum in green and the maximum in cyan are spinodals satisfying $\partial^2 F/\partial V^2 = 0$ (Debenedetti, 1996), hence the dash-dotted black line is the spinodal curve. The purple arc is non-physical and for those values of p and V the liquid is unstable.

In Fig. 2.8, maintaining the same colour coding used in Fig. 2.7, the Helmholtz free energy of a generic van der Waals system along an isotherm at $T < T_C$ is represented. The dashed line represents the stable thermodynamic equilibrium of the system. The system becomes metastable if it follows the green or cyan curve.

From the point of view of aqueous solutions, the states we are considering are metastable, i.e. they are not in a phase of thermodynamic equilibrium (meaning state points in which the system can stay for an infinite time) but *there is mechanical stability*. For this reason the spinodal in this context is called limit of mechanical stability (LMS).

2.3 SUPERCOOLED WATER

Normally, water is liquid between 273 K and 373 K at standard atmospheric pressure. Under certain conditions (Gallo et al., 2016; Gallo and Stanley, 2017; Angell, 1983; Debenedetti, 2003; Gallo and Rovere, 2021), such as lack of impurities and extremely isolated environments, however, this liquid phase can exist down in temperature to as low as 227 K (Kim et al., 2017).

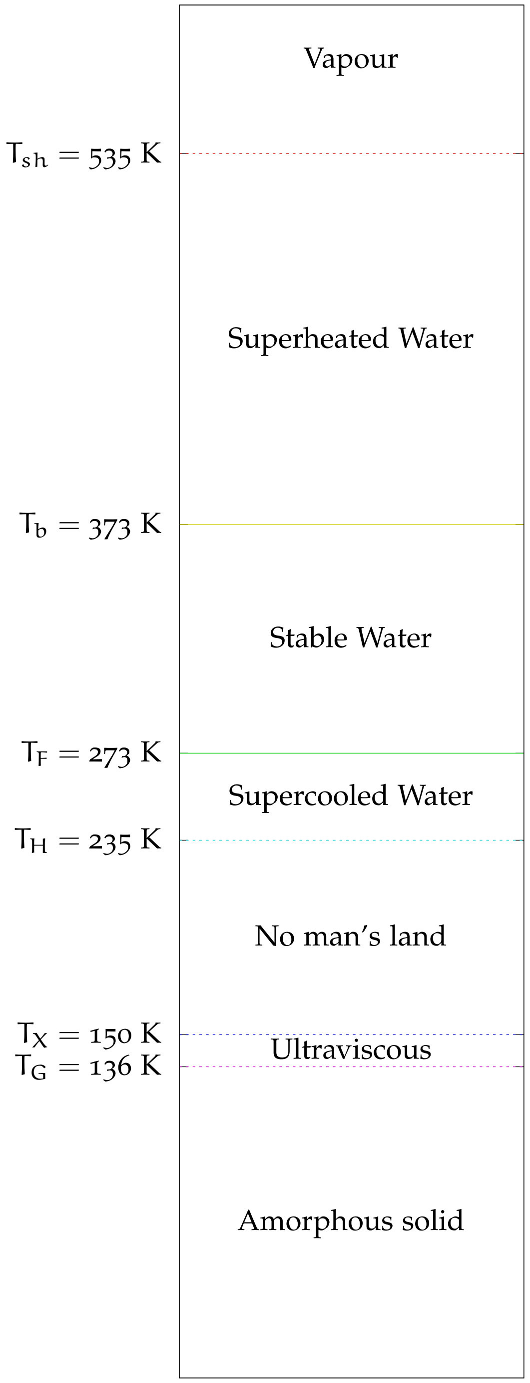

Figure 2.9: Schematic thermodynamic (solid lines) and kinetic (dashed lines) boundaries of non-crystalline water at $p = 1$ atm adapted from Debenedetti and Stanley, 2003.[1]

In this context, metastable water that retains its liquid nature below its freezing point is known as *'supercooled'*.

A scheme of the boundaries of the regions of noncrystalline water adapted from Debenedetti and Stanley, 2003 is reported in Fig. 2.9.

One typical process to experimentally explore the supercooled phase of water and avoid nucleation involves purifying the sample and dividing it into small droplets (Mishima, 1996; Kanno et al., 1975; Tombari et al., 1999; Krämer et al., 1999, 1996).

By reducing the concentration of impurities that trigger crystallisation to approximately 10^{15} per m^3, a droplet measuring 5 µm is likely to contain less than one impurity (Angell, 1983).

These droplets can be supercooled down to temperatures at which the intrinsic crystallisation rate is so high that the droplet's lifespan becomes negligible.

For instance, the lifespan of a 5 µm *droplet is around* 10^{-5} s *when the nucleation rate is at* 10^{21} m^{-3}.

This scenario set a pressure-dependent experimental threshold for supercooling, known as *homogeneous nucleation temperature* T_H, which has hence commonly been located at 235 K.

It must be underlined that at T_H no thermodynamic spinodal occurs. In fact, if water is supercooled below $T_X = 150$ K, for fast enough cooling rates, an ultraviscous supercooled liquid is obtained (Debenedetti, 2003).

The region $T \in (T_H, T_X)$ is called *no man's land* (Mishima and Stanley, 1998b), because inside it nu-

---

[1] The values of T_H and T_X conventionally adopted in literature were used.

cleation occurs too quickly for existing experimental methods to allow the observation of supercooled water.

However, recent experimental observations, performed by using evaporative cooling of micron sized water droplets, reached a new upper end of the no man's land at around 227 K (Kim et al., 2017).

Another metastable form in which water can occur is glassy water. From a structural point of view there is no difference between a supercooled liquid and a glass, yet typically in glasses a dramatic dynamic slowdown takes place in a very small temperature span, with the viscosity of the system increasing abruptly by as much as 12 orders of magnitude or more. This feature, although from the point of view of the critical phenomena the glass transition is not a transition at all, makes it possible to operatively define the glass transition temperature T_G as that at which the viscosity is 10^{12} Pa s (Debenedetti, 2003; Gallo and Rovere, 2021; Cavagna, 2009; Angell, 2002).

Glassy forms of water include low-density amorphous (LDA), high-density amorphous (HDA) and very high density amorphous (VHDA, Loerting et al., 2001).

The metastable LDA and HDA phases have been shown to be separated by a first-order-like phase transition (Mishima et al., 1985; Winkel et al., 2008) and can be obtained through vapour deposition (LDA) or through compression from the solid phase (HDA). LDL (low-density liquid) and HDL (high-density liquid) metastable phases have been theorised to exist in the no man's land (Sec. 2.7).

The lower end region of the no man's land was also accessed (Seidl et al., 2015) via techniques such as laser heating amorphous ice up to 205 K on femtosecond scales (Kim et al., 2020).

2.4 THERMODYNAMIC ANOMALIES OF WATER

Despite being Earth's most prevalent liquid, water is known (Gallo et al., 2016; Gallo and Stanley, 2017; Angell, 1983; Debenedetti, 2003; Gallo and Rovere, 2021) for featuring a significant amount of anomalies compared to the others.

Density Anomaly

Over 75 such anomalies have been identified to date (Chaplin, 2022). Among them the best-known is the *density anomaly*. As previously discussed in Sec. 2.1.1, the liquid-solid coexistence line has a negative slope. At atmospheric pressure, the density of water does not follow a monotonic decrease with increasing temperature. Instead, it exhibits a maximum at 277 K. This Temperature of Maximum Density (TMD) exhibits a range of values as the pressure varies leading to a TMD curve in the water phase diagram. Experimental TMD points for D_2O from Angell and Kanno, 1976 are reported in Fig. 2.10.

In deep supercooled confined water, a Temperature of Minimum Density (TmD) was also observed experimentally (Liu et al., 2007; Mallamace et al., 2007), at temperatures below which water resumes the behaviour of a conventional liquid with the density decreasing upon cooling. The behaviour

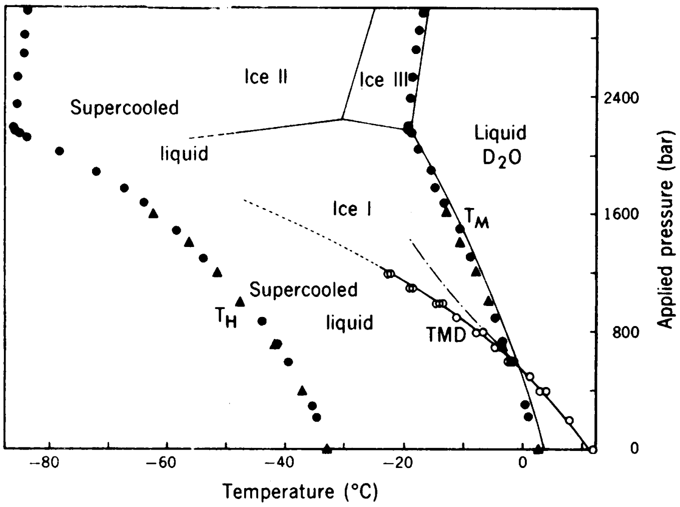

Figure 2.10: TMD line for D_2O from Angell and Kanno, 1976.

of such confined water has been shown to be very similar to the bulk (Gallo et al., 2010, 2000a,b). Simulation studies show that the TmD might also exist in bulk water (Paschek, 2005).

Thermodynamic Response Functions

We now consider the thermodynamic response functions and their connection to fluctuations (Landau and Lifshitz, 1958) which link the macroscopic thermodynamic features to the microscopic behaviour described by statistical mechanics.

ISOTHERMAL COMPRESSIBILITY

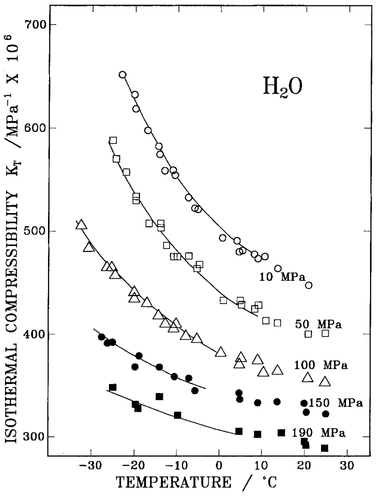

Figure 2.11: Supercooled water's isothermal compressibility. Figure from Debenedetti, 2003.

The isothermal compressibility

$$\kappa_T = -\frac{1}{V}\frac{\partial V}{\partial p}\bigg|_T \qquad (2.4)$$

is connected to the fluctuations of volume of a system with a fixed number of particles by

$$\langle (V - \langle V \rangle)^2 \rangle = V k_B T \kappa_T\,;$$

Fig. 2.11 shows experimental measurements of κ_T along isobars.
While in simple liquids κ_T typically shows a decreasing behaviour upon lowering the temperature, in the case of water it reaches a minimum prior to an increase. At ambient pressure, the minimum is at $T = 319$ K.
This increase is particularly noticeable in the supercooled phase.

ISOBARIC SPECIFIC HEAT

The isobaric specific heat

$$c_p = \frac{T}{N}\left.\frac{\partial S}{\partial T}\right|_p \tag{2.5}$$

is connected to the entropy fluctuations of N molecules at fixed p

$$\langle (S - \langle S \rangle)^2 \rangle = N\, k_B\, C_p$$

and to the isochoric specific heat by

$$c_p - c_V = \frac{VT}{N}\frac{\alpha_p^2}{\kappa_T}\,.$$

Fig. 2.12 shows its similar trend to κ_T upon lowering T, with a minimum and a consequent steady increase. The minimum is at $T = 308$ K at ambient pressure.

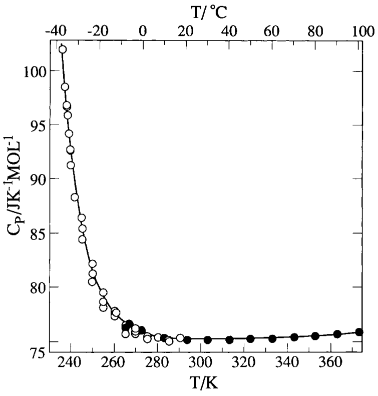

Figure 2.12: Supercooled D_2O isobaric heat capacity. Figure from Debenedetti, 2003.

COEFFICIENT OF THERMAL EXPANSION

The coefficient of thermal expansion (see Fig. 2.13 for D_2O)

$$\alpha_p = \frac{1}{V}\left.\frac{\partial V}{\partial T}\right|_p \tag{2.6}$$

is connected to the fluctuations of volume and entropy

$$\langle (V - \langle V \rangle)(S - \langle S \rangle) \rangle = V\, k_B T\, \alpha_p\,.$$

$$\begin{cases} \alpha_p > 0 & T > \mathrm{TMD} \\ \alpha_p = 0 & T = \mathrm{TMD} \\ \alpha_p < 0 & T < \mathrm{TMD}. \end{cases}$$

At ambient pressure, TMD = 277 K. In a simple liquid α_p decreases monotonically upon decreasing T but satisfies $\alpha_p > 0$.

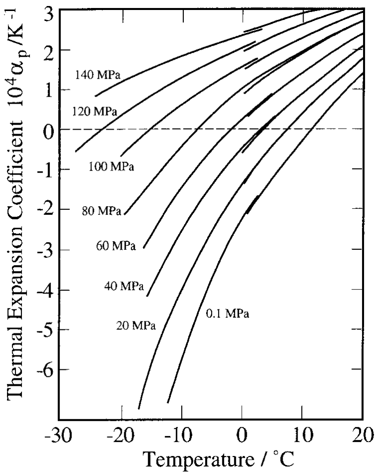

Figure 2.13: Supercooled D_2O coefficient of thermal expansion. Figure from Debenedetti, 2003.

2.4.1 *Apparent singularities*

Schematic reproductions of the behaviour of water's density and of its thermodynamic response functions at ambient pressure are reported in Fig. 2.14 and Fig. 2.15.

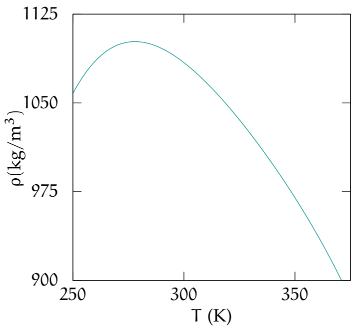

Figure 2.14: Density of water at ambient pressure. Data adapted from Chaplin, 2022.

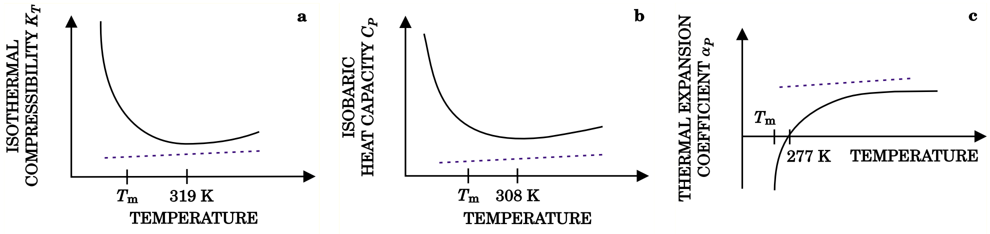

Figure 2.15: Thermodynamic response functions compared to simple liquids at ambient pressure, with T_m being the melting temperature: isothermal compressibility (a), isobaric specific heat (b), coefficient of thermal expansion (c). Figure from Debenedetti and Stanley, 2003.

Specifically, the behaviour of isothermal compressibility and isobaric specific heat highlighted in such figures implies that unlike common liquids, at low temperatures, thermal fluctuations in volume and entropy increase rather than decrease.

Moreover, these fluctuations are anticorrelated, being $\alpha_p < 0$. The observed anticorrelation is a result of the formation of an open network of hydrogen bonds. In this network, a reduction in orientational entropy is coupled with an increase in volume.

All the response functions show an (at least) apparent singular behaviour

$$\chi \sim (T - T_S)^{\gamma_\chi}. \tag{2.7}$$

Several hypotheses have been formulated to account for the presumed divergences in the physical properties of supercooled water, their underlying causes remain a subject of ongoing debate.

Among these, Speedy and Angell [1976] have suggested the existence of a singular temperature at $T_S = 228$ K. However, by far the most widely accepted explanation for the anomalies of water centres around the hypothesis of existence of a second-order Liquid-Liquid Critical Point (LLCP) located within the "no man's land (see Sec. 2.7).

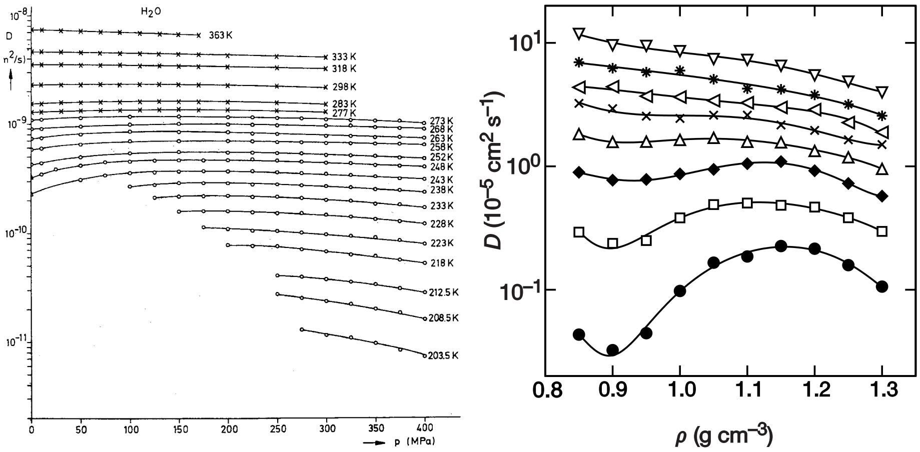

(a) D(p)

(b) D(ρ)

Figure 2.16: Experimental self-diffusion coefficient of water D along isotherms as a function of pressure (a) and density (b). Fig. (a) from Debenedetti, 2003. Fig. (b) from Errington and Debenedetti, 2001.

2.5 DYNAMIC ANOMALIES OF WATER

Diffusion anomaly

Figure 2.16 shows the experimental behaviour of water self-diffusion coefficient D. In typical liquids, D decreases with increasing compression. However, water exhibits an anomalous behaviour at approximately 283 K, where its diffusivity initially increases with rising pressure, reaching a peak around 150 MPa. Computer simulations have further revealed that as the temperature decreases beyond this point, water's diffusivity reverts to the normal behaviour, thus passing through a minimum. By connecting these points of maximum and minimum diffusivity, one can draw a line of diffusivity extrema in the phase diagram (Errington and Debenedetti, 2001; Xu et al., 2006; de Oliveira et al., 2008).

2.6 STRUCTURAL ANOMALIES

The thermodynamic and dynamic anomalies of water have frequently been attributed to the structure of water and its hydrogen bond network. Theoretical and computational studies have shown that these anomalies are both contained within a broader region of structural anomalies (Errington and Debenedetti, 2001; Yan et al., 2007; Nilsson and Pettersson, 2015).

This region was defined using a local orientational order parameter q, which measures the degree of tetrahedral order in the arrangement of water molecules in the first shell, and a translational order parameter t, which measures the tendency of two water molecules to occupy a preferred separation.

An anomalous region emerges where both order parameters simultaneously decrease with increasing pressure. The line of structural anomalies is then defined by identifying the loci of maxima in orientational order at low densities and minima in translational order at high densities. Within this zone of structural anomalies, water exhibits an increase in disorder upon compression. Therefore it has been shown that upon increasing the degree of order, structural, dynamic and thermodynamic anomalies of water occur in a cascade (Fig. 2.17, Errington and Debenedetti, 2001).

2.7 THE LIQUID-LIQUID CRITICAL POINT SCENARIO

2.7.1 *The LLCP hypothesis*

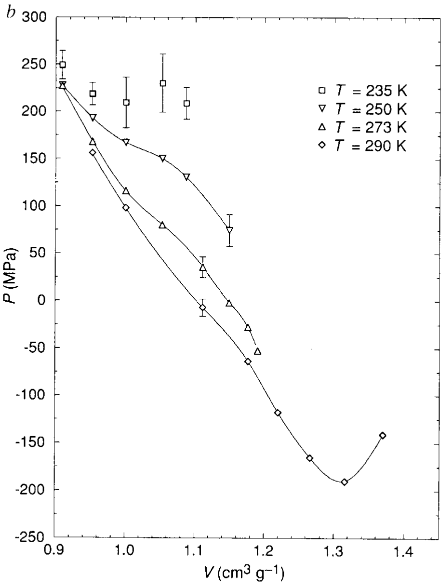

Figure 2.18: Low-temperature isotherms in the (p, V) plane for the ST2 model of water. Figure from Poole et al., 1992.

The Liquid-Liquid Critical Point (LLCP) scenario was theorised in 1992 in a paper by Poole, Sciortino, Essmann and Stanley in which, upon investigation of the thermodynamic and structural features of the supercooled ST2 model of water through molecular dynamics (MD) simulations, the occurrence of the aqueous anomalies were ascribed to the existence of a second-order liquid-liquid phase transition. The LLCP would occur in the no man's land.

In the LLCP framework, below the critical temperature T_C, two phases of water arise: high-density liquid (HDL) and low-density liquid (LDL). Like their amorphous counterparts, in this scenario, the HDL and the LDL phases are separated by a manifold of first-order phase transitions ending at the LLCP, where the distinction between the two phases disappears with

$$\rho_{HDL} - \rho_{LDL} \xrightarrow{T \to T_C^-} 0. \tag{2.8}$$

This is a very common occurrence in critical phenomena, linked to the existence of a diverging correlation length at the second-order critical point. Above T_C, a line of state points corresponding to the maxima of the correlation length develops, the *Widom line* (Xu et al., 2005; Franzese and Stanley, 2007). This line is the extension in the one-phase region of the HDL-LDL coexistence curve (see also Fig. 1.2) and has also been observed for the liquid-vapour critical point (Anisimov et al., 2004; Gallo et al., 2014).

The divergence of the correlation length provides an explanation for the polynomial increases observed in the thermodynamic response functions and discussed in Sec. 2.4, as they behave as precursors of the second-order transition, themselves exhibiting maxima along or close to the Widom Line and a singular behaviours near the critical point.

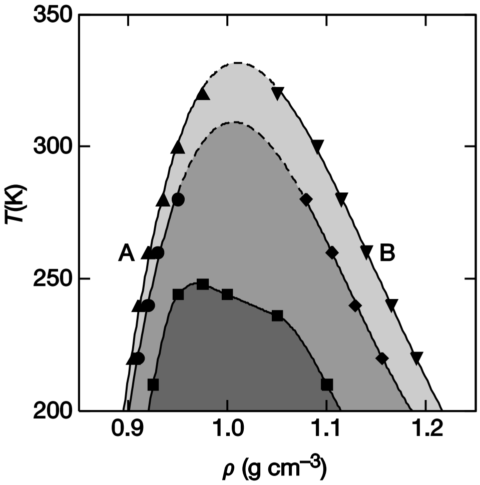

Figure 2.17: Loci of structural, dynamic and thermodynamic anomalies for the SPC/E model of water from Errington and Debenedetti, 2001: q maxima (triangles up) and t minima (triangles down) locate the structural anomaly region, where water's degree of order decreases upon compression; D maxima (circles) and minima (diamonds) locate the diffusivity anomaly region, where the diffusion coefficient increases upon increasing density; the TMD points (squares) locate the region of density anomaly, where ρ increases upon isobaric heating.

In the simulations performed in Poole et al., 1992 on the ST2 model of water

- the occurrence of van der Waals loops and a flex point in the isotherm curves were observed in the low-temperature phase diagram, signalling the occurrence of two distinct phases at temperatures below a second-order critical point: Fig. 2.18 and 2.19(a);
- one of the two phases structurally resembled that of the HDA, the other one that of the LDA. Therefore they were named HDL and LDL: Fig. 2.19(b);
- experimental anomalies of water were reproduced by the ST2 model: Fig. 2.19(c) and 2.19(d).

Following the publication of the seminal paper by Poole et al. [1992], a significant amount of work has been undertaken across experimental, theoretical, and computational physics to further develop and contribute to the current understanding of this concept (see for example Mishima and Stanley, 1998a,b; Errington and Debenedetti, 2001; Ito et al., 1999).

All major contributions regarding the implications of an LLCP in the phase diagram of supercooled water, along with both supporting and contesting studies, were comprehensively reviewed by Gallo et al. in 2016.

The phase diagram of water in the LLCP scenario adapted from Gallo et al., 2016 is reported in Fig. 2.20 showing the second-order LLCP, the HDL and the LDL phases with the HDL-LDL coexistence line in the no man's land, the ultraviscous liquids, and the amorphous HDA and LDA phases.

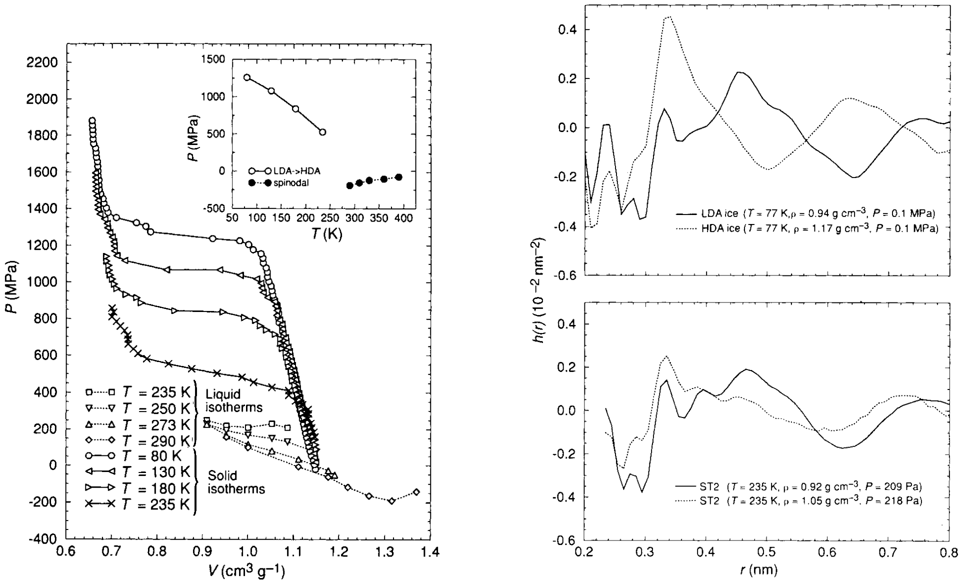

(a) Isothermal compression

(b) Structural comparison: HDL-LDL vs HDA-LDA

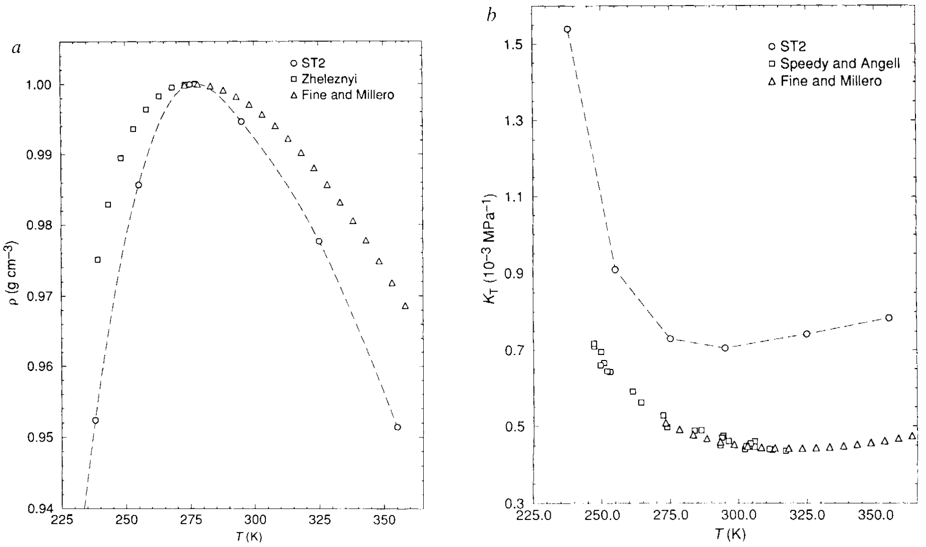

(c) Density

(d) Response functions

Figure 2.19: Thermodynamic and structural results of MD calculations performed on the supercooled ST2 model of water: figures from Poole et al., 1992.

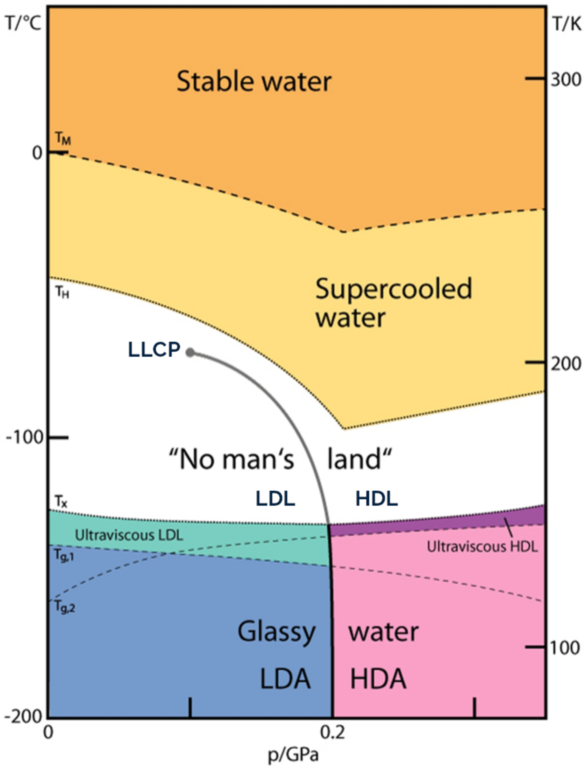

Figure 2.20: Phase diagram of non-crystalline water (adapted from Gallo et al., 2016) highlighting the 'no-man's land', a region currently observed to contain only crystalline ices, bounded by the homogeneous nucleation line T_H above and the crystallisation line T_X below. Located in the no man's land is the Liquid-Liquid Critical Point (LLCP) at temperatures below which two distinct phases of water, separated by a coexistence first-order phase transition line, exist: high-density liquid (HDL) and low-density liquid (LDL). The coexistence line ends at the LLCP. Situated just beneath T_X are two ultra-viscous liquid domains, namely HDL and LDL ultraviscous liquids. The glass transition temperatures $T_{g,1}$ and $T_{g,2}$, which demarcate the transition from the glassy solids LDA and HDA to the ultra-viscous liquids LDL and HDL, are also reported.

2.7.2 *Experimental Results*

The hypothesised location of the critical point in the no man's land renders its experimental investigation extremely challenging, being constrained by the emergence of homogeneous nucleation. However, it has been shown that the amorphous phase can be linked to normal liquid water via a reversible thermodynamic path (Speedy et al., 1996), and notably, the experimental boundary of the no man's land has been recently observed to be narrower than historically thought (Kim et al., 2017; Seidl et al., 2015; Nilsson, 2022).

Kim et al. [2017], in particular, were able to measure the structure as well as the maxima in isothermal compressibility and correlation length. The presence of a maximum in the correlation length is a characteristic feature of the Widom line. Therefore, their findings unambiguously confirm the existence of this line, and consequently, provide evidence for a second-order critical point (Gallo and Stanley, 2017).

Also, while investigating the melting lines induced by decompression in various high-pressure ice phases within small emulsified droplets, a discontinuity in the melting line of ice IV was observed at the position suggested for the liquid-liquid transition which Mishima and Stanley predicted to happen at $T_c \approx 220$ K, and $p_c \approx 100$ MPa (Mishima and Stanley, 1998a,b).

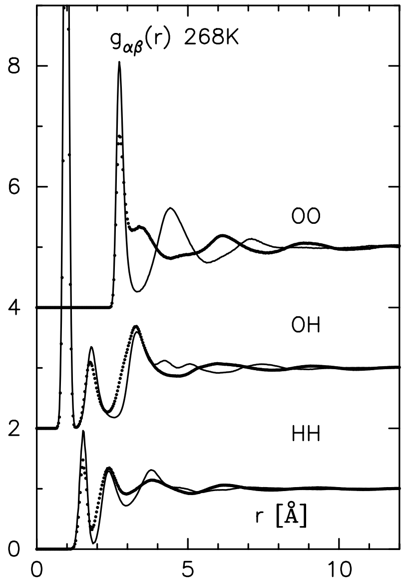

Figure 2.21: Radial distribution functions for LDL (lines) and HDL (circles) water at T = 268 K. Figure from Soper and Ricci, 2000.

By electron spin resonance experiments, Banerjee et al. [2009] identified results in bulk water that align with the LDL-HDL coexistence in the deeply supercooled region.

Experimental results from neutron scattering on water confined in silica MCM-41 pores are consistent with the LLCP hypothesis (Liu et al., 2007; Liu et al., 2005, 2006; Zhang et al., 2011a).

The structural properties of the hypothesised LDL and HDL phases were investigated by studying the water radial distribution functions (RDFs) through neutron diffraction scattering experiments. Soper and Ricci's research revealed that in the HDL phase, the second shell of the oxygen-oxygen RDF collapses in comparison to the LDL phase, indicating a significant disruption of hydrogen bonds between the first and second shell of water molecules. Furthermore, in the HDL phase, the hydrogen bonds within the first shell become more linear. Figure 2.21 from Soper and Ricci, 2000 illustrates the oxygen-oxygen, oxygen-hydrogen, and hydrogen-hydrogen RDFs.

2.7.3 *Numerical Simulations*

Computer simulations have been instrumental in investigating the LLCP, not only because its hypothesis emerged from computational studies but also because they circumvent experimental challenges associated with nucleation by employing faster cooling rates. This approach enables the exploration of the no-man's land.

The existence and classification of the LLCP have been rigorously proved to be of the second-order Ising universality class in various water models, specifically ST2 in Palmer et al., 2014; Liu et al., 2012, 2009; Sciortino et al., 2011; Kesselring et al., 2013; Smallenburg and Sciortino, 2015, TIP4P/2005 (Abascal and Vega, 2005) and TIP4P/Ice (Abascal et al., 2005) in Debenedetti et al., 2020, and Jagla (Jagla, 2001) in Gallo and Sciortino, 2012.

In these three models the isothermal compressibility and the correlation length of the TIP4P/2005 were found, for $T \to T_C$, to have a critical behaviour

$$\kappa_T \sim (T - T_C)^{-\gamma} \qquad \xi \sim (T - T_C)^{-\nu} \tag{2.9}$$

with $\gamma = 1.26$ and $\nu = 0.63$ which are the same exponents numerically obtainable for the 3D Ising Model with Monte Carlo techniques (see for example Parisi, 1998) for the magnetic suceptibility χ (γ) and the correlation length ξ (ν).

It is important to note that the TIP4P/2005 and TIP4P/Ice models are particularly renowned for their accuracy in exploring the thermodynamics of water.

Simulation results compatible with the LLCP theory were also obtained for SPC/E (Harrington et al., 1997), TIP4P (Corradini et al., 2010; Poole et al., 1993; Sciortino et al., 1997; Tanaka, 1996), TIP5P (Xu et al., 2005; Kumar et al., 2005; Yamada et al., 2002), TIP5P/E (Paschek, 2005), TIP4P-Ew (Paschek et al., 2008) and BSV (Jedlovszky and Vallauri, 2005) models of water.

A recent line of research has focused on investigating the liquid-liquid transition in ab initio deep neural network models for water. While there are already results consistent with the LLCP hypothesis (Gartner III et al., 2020), no rigorous evidence has yet been obtained.

2.7.4 *Other scenarios*

Notwithstanding the numerous evidences supporting the LLCP theory, it is worth mentioning other scenarios that have been proposed to explain the occurence of water anomalies in supercooled water. The most popular ones over the years have been:

THE SINGULARITY-FREE SCENARIO Sastry et al. [1996] suggested that the density anomaly alone can be considered responsible for the increase in thermodynamic response functions. This increase would give rise to maxima without leading to any divergence (Rebelo et al., 1998). Furthermore, the c_p peaks do not increase upon decreasing the temperature;

THE CRITICAL POINT-FREE SCENARIO Angell [2008] proposed a scenario in which the liquid-liquid transition would be order/disorder first-order-like, with a coexisting phase extending to the region of negative pressures and ending on the LG-LMS line without any occurence of second-order critical points.

Nevertheless, the LLCP hypothesis remains by far the most credited one (Gallo et al., 2016).

2.8 AQUEOUS SOLUTIONS

Water, known for its exceptional properties, is not only a remarkable liquid but also an extraordinary solvent (Gallo et al., 2016; Angell, 2002). Therefore the study of water in solution holds significant importance. Besides, notably, in natural settings, water is primarily found in solutions.

Both experimental analyses and computer simulations have demonstrated that the addition of solutes affects several key thermodynamic properties of water. These include, among many others, the melting and boiling points, viscosity, the TMD, the location of the LLCP and the Widom Line.

The study of water anomalies in ionic solutions is particularly important for their enhanced supercooling capabilities compared to bulk water due to the lowering of the homogeneous nucleation temperature as ion concentration increases (Miyata et al., 2002). Additionally, ions appear to be more favourably solvated in the HDL phase (Souda, 2006; Mishima, 2007).

Research conducted by Archer and Carter (Archer and Carter, 2000; Carter and Archer, 2000) has shown that aqueous solutions of NaCl retain the anomalous behaviour of thermodynamic response functions and the presence of a TMD up to a moderate concentration of 2 mol/kg. However, at higher NaCl concentrations, this anomalous behaviour in heat capacity disappears, though this does not rule out the possibility of a liquid-liquid transition in supercooled NaCl aqueous solutions. In this context, MD simulations by Corradini et al. [2010; 2011] on NaCl in TIP4P water across various concentrations have analysed the LLCP both in bulk water and in solutions, revealing a shift in the thermodynamic plane towards higher temperatures and lower pressures upon salt addition (Fig. 2.22).

Moreover, Mishima's research (Mishima, 2007, 2005) has provided experimental evidence supporting the potential for a liquid-liquid transition in LiCl(aq). This hypothesis has gained additional support from subsequent experimental (Ruiz et al., 2014) and simulation data (Paschek, 2005; Le and Molinero, 2011). Recent simulations by Perin and Gallo [2023] have shown the LLCP in supercooled TIP4P/2005-aqueous solutions of LiCl persist at a concentration of 0.678 mol/kg but no evidence of a critical point at 2.034 mol/kg has been observed, with it possibly having shifted to lower temperatures (Fig. 2.23).

The classification of ions in aqueous solutions as either structure-makers or structure-breakers has been a topic of interest in understanding how ions influence water structure (Hribar et al., 2002). Structure-making ions

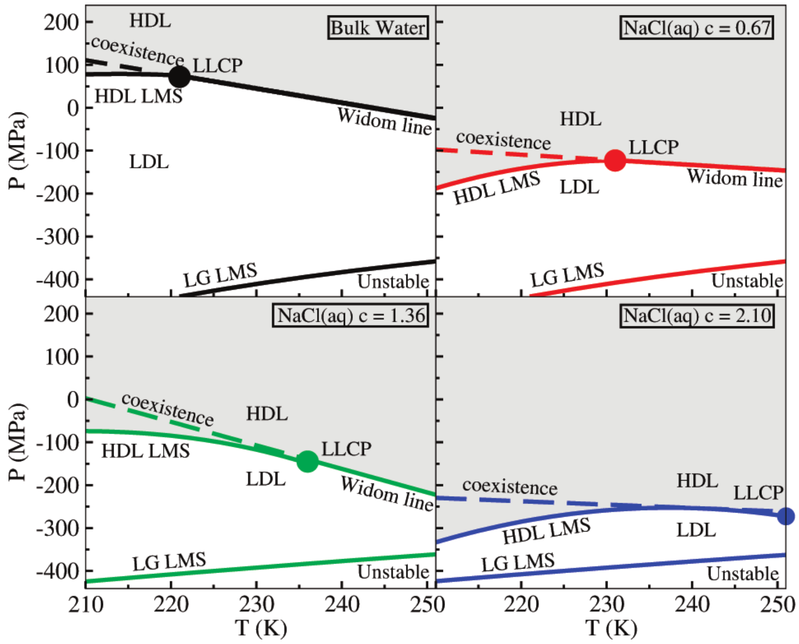

Figure 2.22: Phase diagram of NaCl aqueous solutions in supercooled water, derived from MD simulations. With a rise in salt concentration, the LDL region contracts and the LLCP moves towards higher temperatures and lower pressures. Figure from Corradini and Gallo, 2011.

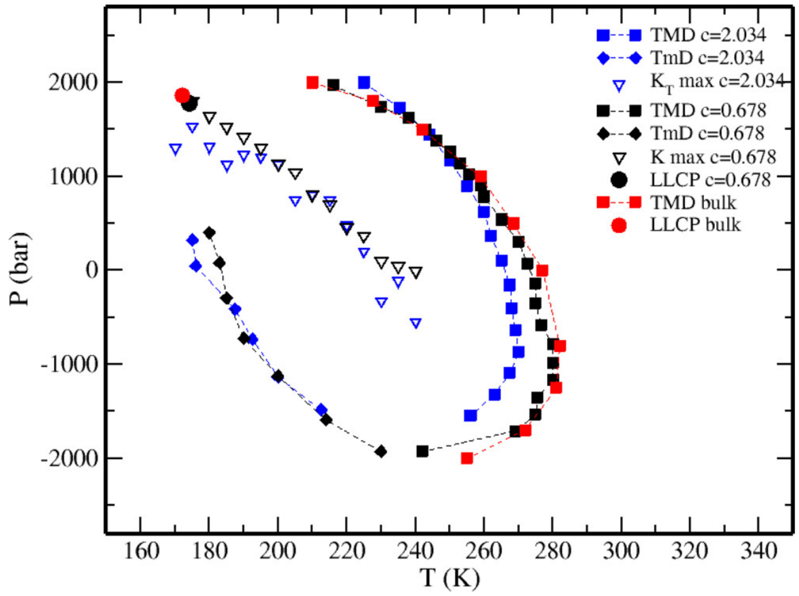

Figure 2.23: Phase diagram of LiCl aqueous solutions in supercooled TIP4P/2005 water, derived from MD simulations. Figure from Perin and Gallo, 2023.

are thought to cause a rearrangement of nearby water molecules, resulting in an ordered hydration structure. Structure-breaking ions are considered to weaken or distort the hydrogen bonds of surrounding water molecules. However, this classification is only qualitative and its validity has been challenged over the years (Gallo et al., 2011; Smith et al., 2007; Soper and Weckström, 2006).

In summary, research across experiments, theory, and simulations on supercooled aqueous solutions indicates their potential as a viable pathway for resolving the complexities of supercooled water. These solutions not only provide easier access to the supercooled state of this anomalous liquid but also suggest the possibility of shifting the LLCP to more experimentally accessible regions of the phase diagram.

2.8.1 *Aqueous Perchlorate Solutions*

Water anomalies are notably linked to its role as a "matrix for life" (Franks, 2000), and in this context, the study of water in solutions is crucial. Aqueous solutions are widespread and, as discussed in the previous section, water often tends to supercool more easily in such environments (Corradini et al., 2010, 2012; Archer and Carter, 2000), leading to significant research focus on the structure and thermodynamics of water in solution.

Regarding aqueous solutions, the hypothesis of liquid water existing in perchlorate solutions beneath the Martian South Pole crust has been put forward to explain anomalously bright basal reflections detected through dielectric permittivity measurements on Mars (Orosei et al., 2018; Lauro et al., 2021). Perchlorate salts of magnesium, sodium, calcium and potassium are ubiquitous on Mars and therefore deemed to be the natural candidates to provide an explanation for these findings.

Notably, the subsoil temperature at the Martian South Pole, where the liquid solutions were discovered, is about 180 K, considerably lower than the freezing point of water in such solutions (Orosei et al., 2018; Chevrier et al., 2009). This implies that it is due to the solutes properties that water is enabled to remain liquid at temperatures lower than its freezing point.

Experiments (Toner et al., 2014) have shown that sodium perchlorate solutions can be supercooled down to approximately 220 K, while magnesium and calcium perchlorate can reduce this temperature to at least 150 K.

The ability of water to retain its liquid form upon supercooling in perchlorate solutions is potentially also due to its anomalies. The local structural ordering affects not only water's anomalies but also ice nucleation (Gallo et al., 2016). Thus, studying the thermodynamics of supercooled aqueous solutions of perchlorates is highly topical.

Experimental studies have investigated the structure-making or structure-breaking properties of perchlorate ions in water, particularly under conditions akin to those underneath Martian soil. These studies show that even at high concentrations, the hydrogen-bond network of water is only partially disrupted by perchlorate ions (Laurent et al., 2020, 2019; Lenton et al., 2017).

Recent findings by Calvagna et al. [2021] indicate that water anomalies persist in dilute sodium perchlorate solutions up to 2M.

This thesis will focus on the study of the thermodynamics and structure of aqueous solutions of sodium perchlorate (Chapters 4 and 5) and magnesium perchlorate (Chapters 6 and 7) in order to understand the effect of Martian solutes on supercooled water and what role water anomalies play in this context.

Further details on perchlorates and perchlorate aqueous solutions are reported in Sec. 4.1.1 and in Chapter 6's introduction.

3

NUMERICAL SIMULATIONS OF AQUEOUS SOLUTIONS

3.1 MOLECULAR DYNAMICS

The core principle of classical Molecular Dynamics (MD) involves solving the Hamiltonian equations of motion for a many-body system through the application of finite difference integration algorithms (Allen and Tildesley, 2017). These algorithms provide the basis for the computational study of the physics of liquid matter and will be extensively employed in this thesis to analyse the thermodynamics and the structure of aqueous perchlorate solutions.

Our focus will be on simulated systems with a constant total number N of particles, for which, in terms of the Cartesian positions of the particles and their momenta, the Hamiltonian can be expressed as

$$H(\mathbf{r},\mathbf{p}) = \sum_{i=1}^{N} \frac{\vec{p_i}^{\,2}}{2m_i} + U(\mathbf{r})\,. \tag{3.1}$$

where the notations

$$\mathbf{r} = (\vec{r}_1, \vec{r}_2, \dots, \vec{r}_N)$$
$$\mathbf{p} = (\vec{p}_1, \vec{p}_2, \dots, \vec{p}_N)$$

were introduced to facilitate reading.

Assuming that the potential $U(\mathbf{r})$ is a pairwise function, Eq. (3.1) can be rewritten as

$$H(\mathbf{r},\mathbf{p}) = \sum_{i=1}^{N} \frac{\vec{p_i}^{\,2}}{2m_i} + \frac{1}{2}\sum_{i}\sum_{j\neq i} U(\vec{r}_i - \vec{r}_j) \tag{3.2}$$

and the Hamiltonian equations (Goldstein, 2002; Arnold et al., 1989) are

$$\begin{cases} \dot{\vec{p}}_i = -\vec{\nabla}_{\vec{r}_i} H(\mathbf{r},\mathbf{p}) = -\vec{\nabla}_{\vec{r}_i} U \\ \dot{\vec{r}}_i = \vec{\nabla}_{\vec{p}_i} H(\mathbf{r},\mathbf{p}) = \dfrac{\vec{p}_i}{m_i} \end{cases} \tag{3.3}$$

which allows, given the initial conditions $(\mathbf{r}_0, \mathbf{p}_0)$, to deterministically obtain the positions $\vec{r}_i$ and the velocities $\vec{v}_i = \vec{p}_i/m_i$ of any particle in the system by iterative discrete integrations from a time t to a time $t+\Delta t$. Details regarding integration algorithms can be found in Sec. 3.2.

Assuming that in the system there are no integrals of motion other than the energy E, the equilibrium condition can be defined by the probability distribution

$$P_{eq}\left(H(\mathbf{r},\mathbf{p})\right) \sim \delta(H(\mathbf{r},\mathbf{p}) - E) \tag{3.4}$$

which, for a system with known and fixed E, V, N (energy, volume and number of molecules) also serves as a proper definition of the *microcanonical ensemble* in statistical mechanics (see Parisi, 1998; Huang, 1987).

TIME AVERAGES For a generic observable $A(\mathbf{r}, \mathbf{p})$, i.e. any thermodynamic quantity, a measurement of A is defined by its time average

$$\bar{A} = \lim_{t \to \infty} \frac{1}{t} \int_0^t dt' \, A(\mathbf{r}(t'), \mathbf{p}(t')) \,. \tag{3.5}$$

ENSEMBLE AVERAGE An ensemble average can be also considered

$$\langle A \rangle = \int d\mathbf{r} \, d\mathbf{p} \, P_{eq}(H(\mathbf{r}, \mathbf{p})) A(\mathbf{r}, \mathbf{p}) \,. \tag{3.6}$$

ERGODICITY As long as the simulations run over timescales much higher than the characteristic time of molecular motion, in MD the *ergodic hypothesis* is assumed (see for example Gallavotti, 2014; Cencini et al., 2010):

$$\langle A \rangle = \bar{A} \,, \tag{3.7}$$

i.e. that the time average does not depend on the initial condition of the system and its value is the same as the one obtained by the ensemble average.

In the microcanonical ensemble, pressure and temperature are thermodynamic observables and can be computed by means of the (generalised) equipartition theorem (Huang, 1987)

$$\left\langle x_\alpha \frac{\partial H}{\partial x_\beta} \right\rangle = \delta_{\alpha\beta} k_B T \tag{3.8}$$

where x_α is any one-dimensional canonical coordinate and $k_B = 1.38 \times 10^{-23}\,\mathrm{J\,K^{-1}}$ is the Boltzmann constant.

- The temperature can be computed from

$$\sum_{i=1}^{N} \langle \vec{p}_i \cdot \vec{\nabla}_{\vec{p}_i} H(\mathbf{r}, \mathbf{p}) \rangle = 2 \underbrace{\sum_{i=1}^{N} \frac{1}{2m_i} \langle \vec{p}_i^{\,2} \rangle}_{\langle E_K \rangle} = 3N k_B T \,,$$

  E_K being the kinetic energy, hence

$$T = \frac{2}{3} \frac{\langle E_K \rangle}{N k_B} . \tag{3.9}$$

- The pressure can be computed from the virial

$$\sum_{i=1}^{N} \langle \vec{r}_i \cdot \vec{\nabla}_{\vec{r}_i} H(\mathbf{r}, \mathbf{p}) \rangle = - \underbrace{\sum_{i=1}^{N} \langle \vec{r}_i \cdot \dot{\vec{p}}_i \rangle}_{\text{virial}} = \underbrace{\sum_{i=1}^{N} \langle \vec{r}_i \cdot \vec{F}_i^{(ext)} \rangle}_{-PV} + \underbrace{\sum_{i=1}^{N} \langle \vec{r}_i \cdot \vec{F}_i^{(int)} \rangle}_{\mathcal{W}} = \\ = 3N k_B T \,,$$

  where $\mathcal{W}$ is the internal virial (Allen and Tildesley, 2017), hence

$$P = \frac{N k_B T}{V} + \frac{\mathcal{W}}{V} . \tag{3.10}$$

3.2 ALGORITHMS

As discussed in the previous section, MD algorithms are a discrete integration of the equations of motion. The simplest way to proceed for $\dot{\vec{r}}_i = \vec{v}_i$ and $\dot{\vec{p}}_i = m\vec{a}_i$ is to introduce Euler's method by expanding up to the first order:

$$\begin{cases} \vec{v}_i(t+\Delta t) = \vec{v}_i(t) + \vec{a}_i(t)\Delta t + \mathcal{O}\left(\Delta t^2\right) \\ \vec{r}_i(t+\Delta t) = \vec{r}_i(t) + \vec{v}_i(t)\Delta t + \mathcal{O}\left(\Delta t^2\right) . \end{cases}$$

This algorithm, while simple, does not preserve the Hamiltonian properties of the system. However, this problem may be remedied by considering the Euler-Cromer method, in which $\vec{r}_i(t+\Delta t) = \vec{r}_i(t) + \vec{v}_i(t+\Delta t)\Delta t + \mathcal{O}\left(\Delta t^2\right)$ and can work well for simple systems (see for example Barone et al., 2013).

3.2.1 *Verlet Algorithms*

For more accurate computations, higher-order algorithms must be considered. Examples of these include the Verlet class of algorithms.

By summing both the following equations (Verlet, 1967)

$$\begin{cases} \vec{r}_i(t+\Delta t) = \vec{r}_i(t) + \vec{v}_i(t)\Delta t + \frac{1}{2}\vec{a}_i(t)\Delta t^2 + \mathcal{O}\left(\Delta t^3\right) \\ \vec{r}_i(t-\Delta t) = \vec{r}_i(t) - \vec{v}_i(t)\Delta t + \frac{1}{2}\vec{a}_i(t)\Delta t^2 + \mathcal{O}\left(\Delta t^3\right) \end{cases} \tag{3.11}$$

we can obtain

$$\vec{r}_i(t+\Delta t) = 2\vec{r}_i(t) - \vec{r}_i(t-\Delta t) + \vec{a}_i(t)\Delta t^2 + \mathcal{O}(\Delta t^4)$$

since the parity of the result implies the Δt^3 term is null.

By subtracting the equations in (3.11)

$$\vec{v}_i(t) = \frac{\vec{r}_i(t+\Delta t) - \vec{r}_i(t-\Delta t)}{2\Delta t} + \mathcal{O}\left(\Delta t^2\right)$$

is obtained.

Despite being fast and accurate in computing positions, this method does not allow for an equally precise calculation of velocities. Moreover, it is not self-sufficient, since in addition to the initial condition $\vec{r}_0, \vec{v}_0$ it is necessary to know $\vec{r}(\Delta t)$ in order to proceed (Gallo and Rovere, 2021; Allen and Tildesley, 2017; Barone et al., 2013).

LEAPFROG VERLET ALGORITHM To allow for a better computation of the velocities, the leapfrog (Hockney, 1970) Verlet algorithm can be considered, in which, at a time $t + \frac{1}{2}\Delta t$, they are computed from $\vec{r}(t), \vec{a}(t), \vec{v}(t - \Delta t/2)$

$$\vec{v}_i\left(t + \frac{1}{2}\Delta t\right) = \vec{v}_i\left(t - \frac{1}{2}\Delta t\right) + \vec{a}_i(t)\Delta t + \mathcal{O}(\Delta t^2)$$

while the positions are

$$\vec{r}_i(t+\Delta t) = \vec{r}_i(t) + \vec{v}_i\left(t + \frac{1}{2}\Delta t\right)\Delta t + \mathcal{O}(\Delta t^4) .$$

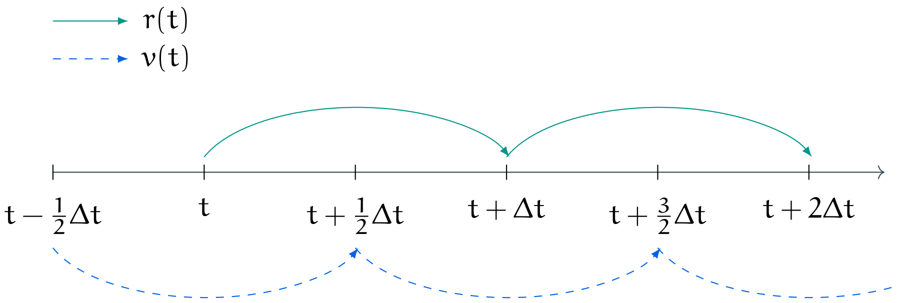

Figure 3.1: Scheme of the leapfrog Verlet algorithm.

Finally $v(t)$ is obtained from

$$\vec{v}_i(t) = \frac{\vec{v}_i\left(t+\frac{1}{2}\Delta t\right) + \vec{v}_i\left(t-\frac{1}{2}\Delta t\right)}{2} + \mathcal{O}(\Delta t^2)\,.$$

A scheme of the algorithm, which was used in the MD simulations performed during the whole PhD programme, is reported in Fig. 3.1.

3.3 MD IN THE CANONICAL ENSEMBLE

MD algorithms are defined in the microcanonical ensemble, which requires the system to be isolated and the knowledge of E, V, N: the equivalence of the ensemble with thermodynamics is established by proving that assuming the equilibrium, the maximisation of entropy follows.

A closer alignment with experimental conditions would require the system to be in contact with an external source of heat at a known absolute temperature T. It is easy to prove that the only equilibrium probability distribution of a system, given T, V, N, can be expressed as:

$$P_{eq}(H(\mathbf{r},\mathbf{p})) = \frac{e^{-\beta H(\mathbf{r},\mathbf{p})}}{Z(T,V,N)} \tag{3.12}$$

provided that $\beta^{-1} = k_B T$ is imposed. The distribution just defined is the canonical probability distribution, and the normalisation $Z(T,V,N) = e^{-\beta F(T,V,N)}$ is the partition function of the system that holds the link between statistical mechanics and thermodynamics, $F(T,V,N)$ being the Helmholtz free energy of the system.

In the canonical ensemble, the energy is not constant but has fluctuations of the order $\Delta E = \mathcal{O}(\sqrt{N})$.

In order to simulate a system in the canonical ensemble a notion of *thermostat* must be introduced, whose role is to alter the energy of the system to obtain the wanted temperature.

A straightforward but rather nonphysical way to do so is to directly rescale the velocities to fix the temperature at a desired value. If Eq. (3.9) is considered without the average brackets, one obtains the instantaneous temperature

$T(t)$. After each iteration of the integration algorithm the atomic velocities $\vec{v}_i$ are rescaled by

$$\vec{v}_i' = \left[\frac{T}{T(t)}\right]^{\frac{1}{2}} \vec{v}_i. \tag{3.13}$$

This algorithm is not actually equivalent to the canonical ensemble since it forbids fluctuations in $T(t)$.

3.3.1 *The Berendsen Thermostat*

A slightly more physical approach to this issue introduced by Berendsen et al. [1984] consists in applying a weak coupling with an external thermal bath, hence slowly correcting the deviation from a reference temperature T by considering

$$dT(t) = \frac{dt}{\tau}(T - T(t)) \tag{3.14}$$

which means that the deviation of the system from T decays exponentially

$$T(t) - T \sim e^{-\frac{t}{\tau}}.$$

The equivalent equation to the (3.13) is obtained by considering a generic

$$\vec{v}_i' = \chi \vec{v}_i$$

and computing the variation in the kinetic energy after rescaling

$$\Delta E_K = \frac{1}{2}\sum_{i=1}^{N}(\chi - 1)m_i\vec{v}_i^2 = \frac{3}{2}(\chi - 1)Nk_B T(t),$$

hence

$$\vec{v}_i' = \left[1 + \frac{\Delta t}{\tau}\left(\frac{T}{T(t)} - 1\right)\right]^{\frac{1}{2}} \vec{v}_i\,.$$

3.3.2 *Velocity-rescaling Temperature Coupling*

The main benefit of the Berendsen algorithm is its high efficiency in controlling the temperature. However, the exponential relaxation of the temperature differentiates it significantly from both the canonical and the microcanonical ensembles. At long times, this translates again into a suppression of the kinetic energy fluctuations (Gallo and Rovere, 2021; Zhou and Liu, 2022; Abraham et al., 2023): hence, $T(t)$ is not a fluctuating quantity in the Berendsen thermostat while it is in the canonical ensemble (with $\Delta T(t)^2 / \langle T(t) \rangle^2 = \mathcal{O}(1/N)$, see for example Frenkel and Smit, 2023). For this reason, the Berendsen thermostat is typically no longer used in MD simulations.

In order to obtain a thermostat that actually enforces a canonical distribution, Bussi et al. [2007] modified the Berendsen thermostat by introducing a stochastic differential equation for the kinetic energy

$$dE_K(t) = \underbrace{\frac{dt}{\tau}\left[E_K - E_K(t)\right]}_{\text{Berendsen}} + 2\frac{dW}{\tau}\left[\frac{E_K E_K(t)}{N_f}\right]^{\frac{1}{2}} \tag{3.15}$$

where

N_f is the number of degrees of freedom;

dW is a Wiener process (Gardiner, 1985; Boffetta and Vulpiani, 2012).

This thermostat, called *velocity-rescaling temperature coupling* (or `v-rescale`) in GROMACS (Hess et al., 2008; Bekker et al., 1993; Berendsen et al., 1995) but usually referred to as the Bussi-Donadio-Parrinello thermostat, was used in all the MD simulations carried out during the PhD programme.

3.3.3 *Equilibration in the Canonical Ensemble*

The overall idea of the ergodic hypothesis introduced in sec. 3.1 is that over the course of a measurement, the system will explore the entire hypersurface of constant energy E, except for regions of measure zero.

In a numerical simulation in the canonical ensemble, being in a steady state is also a requirement to ensure that the measured observables do not depend on the initial conditions. For this reason, each production run, in which thermodynamic quantities are measured, must be preceded by an equilibration run also lasting on a timescale that far exceeds the characteristic time of molecular motion (Allen and Tildesley, 2017).

In this thesis, I will focus on MD simulations of supercooled water and of aqueous solutions.

The role of local minima in supercooled systems

Numerical simulations allow the exploration of regions of the aqueous phase diagram which are typically inaccessible experimentally (Gallo et al., 2016; Gallo and Stanley, 2017; Debenedetti, 2003). However, as mentioned in Chapter 2, supercooled water is a metastable system and therefore characterised by existing in a local minimum of the free energy.

The free energy landscape of such a system is typically given by a very large number of local minima. See for example Fig. 3.2. The equilibration process allows the system, through fluctuations, to reach the non-crystalline metastable minimum $\mathbf{x}_0$ with the lowest free energy.

When the temperature is very low, if the dynamics carried out on the system during the MD equilibration run leads it into the wrong valley and if this basin has a very low free energy, the necessary fluctuation to escape from it may never occur, thus leaving the system trapped into that state without ever reaching $\mathbf{x}_0$.

In a real system, unless nucleation arises first, such a fluctuation typically always occurs but the actual time for the it to take place is a random variable,

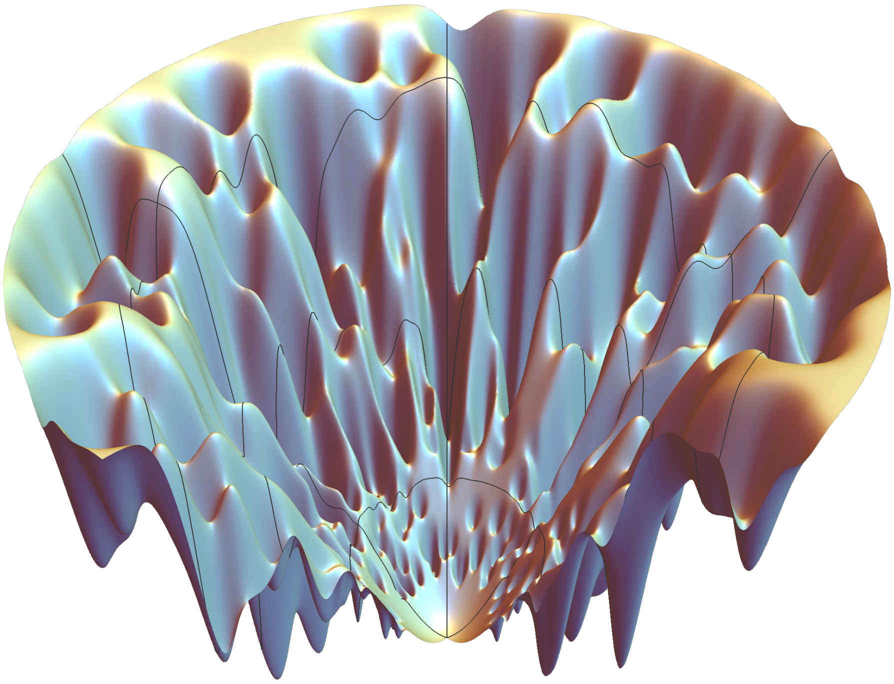

Figure 3.2: Ideal representation of a 3D projection of a system with a free energy landscape decomposed into sub-basins: a typical occurrence in supercooled and amorphous systems in the low-temperature limit. Picture from Altieri et al., 2021.

itself subject to significant fluctuations and therefore can be arbitrarily long. Moreover, as eq. 2.3 implies, it is expected to diverge with the inverse temperature $\beta \to \infty$.

For a completely arbitrary system, the equilibration time may even exceed the age of the universe.

In conclusion, the temperature of a system undergoing molecular dynamics simulations cannot be arbitrarily lowered. Instead, there is a lower limit which can be operatively determined by supercooling the system at very low temperatures, heating it and then verifying, upon recooling, down to what temperature it explores the same equilibrium states it visited before.

In the systems introduced in the following chapters, this lower limit for the temperature has been estimated to be 170 K.

3.4 FORCE FIELDS

Potential energy terms are commonly assumed to be additive (Allen and Tildesley, 2017)

$$U(\mathbf{r}) = U_b(\mathbf{r}) + U_{nb}(\mathbf{r})$$

where

$U_b(\mathbf{r})$ gives the intramolecular *bonded* interactions:

- COVALENT BOND-STRETCHING represents the oscillations around the equilibrium bond length,
- ANGLE-BENDING corresponds to the oscillations of three atoms around an equilibrium bond angle,
- TORSION characterises the torsional rotation of four atoms around a central bond;

$U_{nb}(\mathbf{r})$ gives the intermolecular *non-bonded* interactions:

- LENNARD-JONES

$$U_{LJ}(r_{ij}) = 4\epsilon_{ij}\left[\left(\frac{\sigma_{ij}}{r_{ij}}\right)^{12} - \left(\frac{\sigma_{ij}}{r_{ij}}\right)^{6}\right]$$

- COULOMB

$$U_{Coul.} = \frac{q_i q_j e^2}{r_{ij}}.$$

3.4.1 *Periodic Boundary Conditions and cut-off radius*

While considering the forces acting on a system, boundary interactions must be taken into account. Macroscopic systems with $\mathcal{O}\left(N_{Avogadro}\right)$ particles have negligible boundary terms. Theoretical models in which critical phenomena (such as the liquid-liquid transition) are studied satisfy the thermodynamic limit $N \to \infty$ with a finite N/V.

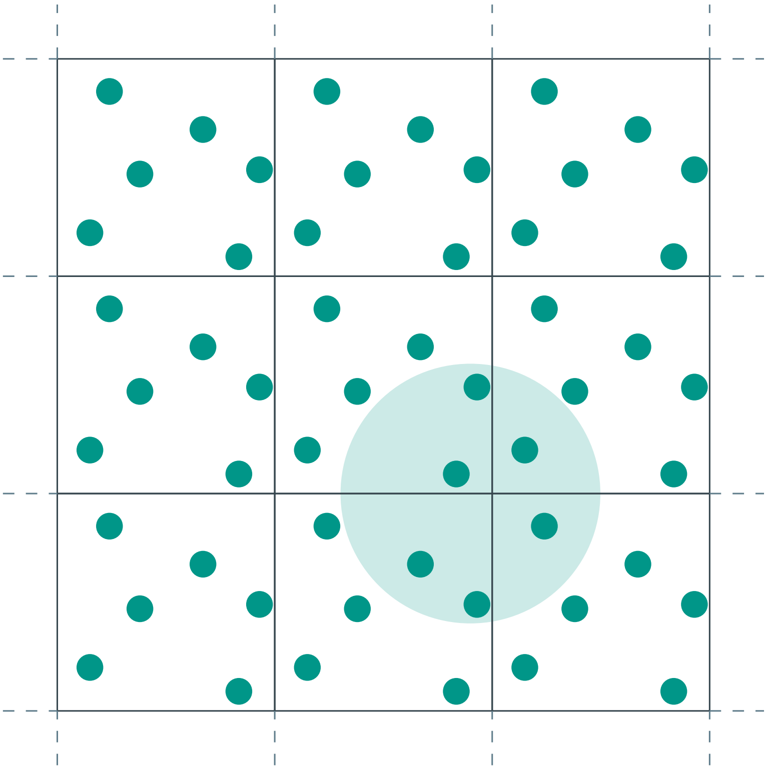

Figure 3.3: 2D system with PBC and a cut-off radius.

Since a typical numerical simulation involves significantly fewer particles, managing the boundary interactions is crucial to prevent them from influencing the system's behaviour.

This issue can be solved by introducing the *periodic boundary conditions* (PBC) in which the simulation box is replicated identically on each side.

As a result, the boundaries are eliminated and the system becomes effectively infinite. To avoid introducing artificial correlations (including every molecule interacting with itself) and very long computational times, the *minimum image convention* (see Gallo and Rovere, 2021) can be assumed: the interactions are computed up to a cut-off $r_c \leqslant L/2$, L being the linear size of the box (Fig. 3.3).

3.4.2 *Models of Water*

In MD simulations, a variety of potentials can be employed. These include the ST2 (Stillinger and Rahman, 1974), SPC (Simple Point Charge, Berendsen et al., 1981), SPC/E (SPC Extended, Berendsen et al., 1987), TIP5P (Transferable Intermolecular Potential with Five Points, Mahoney and Jorgensen, 2000), the TIP4P (Transferable Intermolecular Potential with Four Points Jorgensen et al., 1983) and all of its variants such as TIP4P/Ew (Horn et al., 2004), TIP4P/Ice (Abascal et al., 2005) and TIP4P/2005 (Abascal and Vega, 2005). Among these, the TIP4P/2005 model is known for being the most accurate at replicating the main features of water phase diagram.

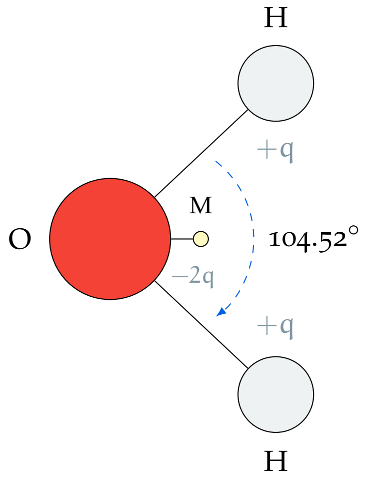

Figure 3.4: Schematic geometry of the TIP4P potentials. Colour coding is red for oxygen, grey for hydrogen, yellow for the dummy site. O−H distance is 0.9572 Å, the O−M distance is 0.1546 Å.

$$U(r_{ij}) = 4\epsilon_{ij}\left[\left(\frac{\sigma_{ij}}{r_{ij}}\right)^{12} - \left(\frac{\sigma_{ij}}{r_{ij}}\right)^{6}\right] + \frac{q_i q_j e^2}{r_{ij}}$$

	MASS (a.m.u.)	z_j (e)	σ_{ij}(nm)	ϵ_{ii}(kJmol^{-1})
H	1.00794	0.5564	0	0
O	15.9994	0	0.31589	0.77490
M	0	-1.1128	0	0

Table 3.1: Force-field details for the TIP4P/2005 model of water.

3.4.2.1 *The TIP4P/2005*

The TIP4P models all share the same rigid geometry reported in Fig. 3.4, with an OH distance of 0.9572 Å and an O−H−O angle of 104.52° fixed at their respective experimental values. A negatively charged (−2q) dummy site M at a distance 0.1546 Å from the oxygen is also present in this set of potentials, while the rest of the Coulombian partial charges are associated to the hydrogens (+q each). The oxygen atom is the Lennard-Jones interaction site.

In this thesis, the TIP4P/2005 will be employed, the force-field parameters of which are reported in Table 3.1.

Part II

SODIUM PERCHLORATE IN AQUEOUS SOLUTIONS

4

THERMODYNAMICS OF $NaClO_4$ AQUEOUS SOLUTIONS

In order to study the phase diagram of aqueous sodium perchlorate solutions from ambient to supercooled conditions, the systems were analysed through molecular dynamics (MD) simulations. This chapter will detail the thermodynamic findings for sodium perchlorate aqueous solutions at concentration ${C_1}^{NaClO_4} = 1.63\,\mathrm{wt\%}$ and ${C_2}^{NaClO_4} = 15.4\,\mathrm{wt\%}$, which were analysed during the second year of the doctoral programme. These results were also published in La Francesca and Gallo, 2023.

4.1 SIMULATION DETAILS FOR A LOW-CONCENTRATION SOLUTION

Methods

The strategy employed to achieve this involved simulating isochores over a temperature range wide enough to allow the investigation of the thermodynamics of the supercooled systems.

Once the set of densities for the isochores was chosen, the preliminary steps entailed picking the initial states of each isochore. These states were prepared using the GROMACS (Hess et al., 2008; Bekker et al., 1993; Berendsen et al., 1995) software suit, setting up a $15\,\mathrm{nm}^3$ simulation box, within which ten ${ClO_4}^-$ ions and ten Na^+ ions were inserted, then filling it with 4099 water molecules. The resulting solution had a concentration of ${C_1}^{NaClO_4} = 1.63\,\mathrm{wt\%}$ which corresponds to a number fraction of 2.43×10^{-3}. The initial condition was further refined by rescaling it to achieve the desired density and generating initial velocities, again via GROMACS, conforming to a Maxwell distribution at a temperature of $T_0 = 400\,\mathrm{K}$. Following this, with the temperature maintained at $T = 400\,\mathrm{K}$, the system underwent its first equilibration run in the canonical ensemble.

Hence, the systems across the isochores had their temperature progressively reduced down to 170 K, as intermediate state points were recorded.

To ensure accurate temporal resolution, in the simulation setup, a 1 fs time step was defined. For the thermostat, the velocity-rescale temperature coupling (Bussi et al., 2007) was used. To address the electrostatic interaction the Particle–Mesh Ewald method was employed (Essmann et al., 1995). Periodic boundary conditions were implemented. The cutoff radii were set at 0.95 nm for all considered solutions.

4.1.1 *Force Fields Descriptions*

The TIP4P/2005 potential

Water was modelled using the TIP4P/2005 (Abascal and Vega, 2005; Vega et al., 2009; Vega and Abascal, 2011) potential, known for its high accuracy in reconstructing water's phase diagram. As already discussed in previous chapters, through MD simulations in 2020, Debenedetti et al. proved that

	MASS (a.m.u.)	q_i (e)	σ_{ii}(nm)	ϵ_{ii}($kJmol^{-1}$)
Na^+	22.9898	1	0.333045	0.011598
Cl	35.4527	1.0786	0.347094	1.108760
O	15.9994	-0.51965	0.878640	0.011598

Table 4.1: Force field details for the sodium perchlorate.

this model of supercooled water exhibits a liquid-liquid transition at 172 K and 186 MPa. The finite size scaling analysis conducted in the same paper indicates that the size here chosen for the system is adequate to appropriately reproduce the thermodynamics in the vicinity of the liquid-liquid critical point (LLCP).

The Perchlorate Ion

The tetrahedral (Fig. 4.1) structure with angles of 109.5° induced by the sp^3 hybridisation of the Cl renders the $ClO_4{}^-$ ion non-polar with a formal charge of -1.

The description of the perchlorate ion provided by Nieszporek et al. and used herein is that of a rigid tetrahedron with the chlorine ion centrally located at a uniform distance of 0.144 nm from each surrounding oxygen. Considering in general a description of the potential given by

$$U(r_{ij}) = 4\epsilon_{ij}\left[\left(\frac{\sigma_{ij}}{r_{ij}}\right)^{12} - \left(\frac{\sigma_{ij}}{r_{ij}}\right)^{6}\right] + \frac{q_i q_j e^2}{r_{ij}}$$

the relevant parameters are itemised in Table 4.1.

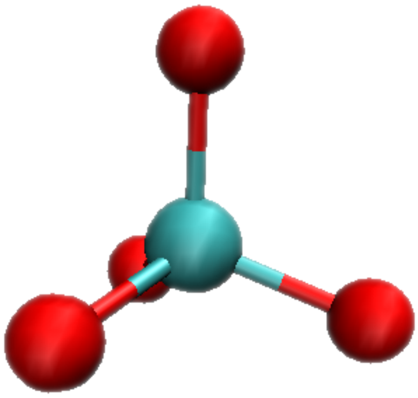

Figure 4.1: 3D visualisation of the perchlorate ion generated using the VMD software (Humphrey et al., 1996).

The Lorentz-Berthelot combination rule

$$\epsilon_{ij} = \sqrt{\epsilon_{ii}\epsilon_{jj}} \qquad \sigma_{ij} = \frac{\sigma_{ii} + \sigma_{jj}}{2} \tag{4.1}$$

completes the parameter space.

4.2 RESULTS FOR THE $C_1{}^{NaClO_4}$ = 1.63 WT% SOLUTION

For the $C_1{}^{NaClO_4}$ solution, 27 isochores were considered with densities spanning from 1140 kg/m^3 to 880 kg/m^3. For each isochore, the initial condition was obtained as described in the previous section: the details of the simulation boxes for each density are presented in Table 4.2.

Over the isochores, state points were simulated at temperatures ranging from 400 K to 170 K. At each temperature, two distinct runs were carried out: an equilibration run and a production run. The durations of these simulations, high enough to make sure the energies of the systems had reached their minima, are detailed in Table 4.3.

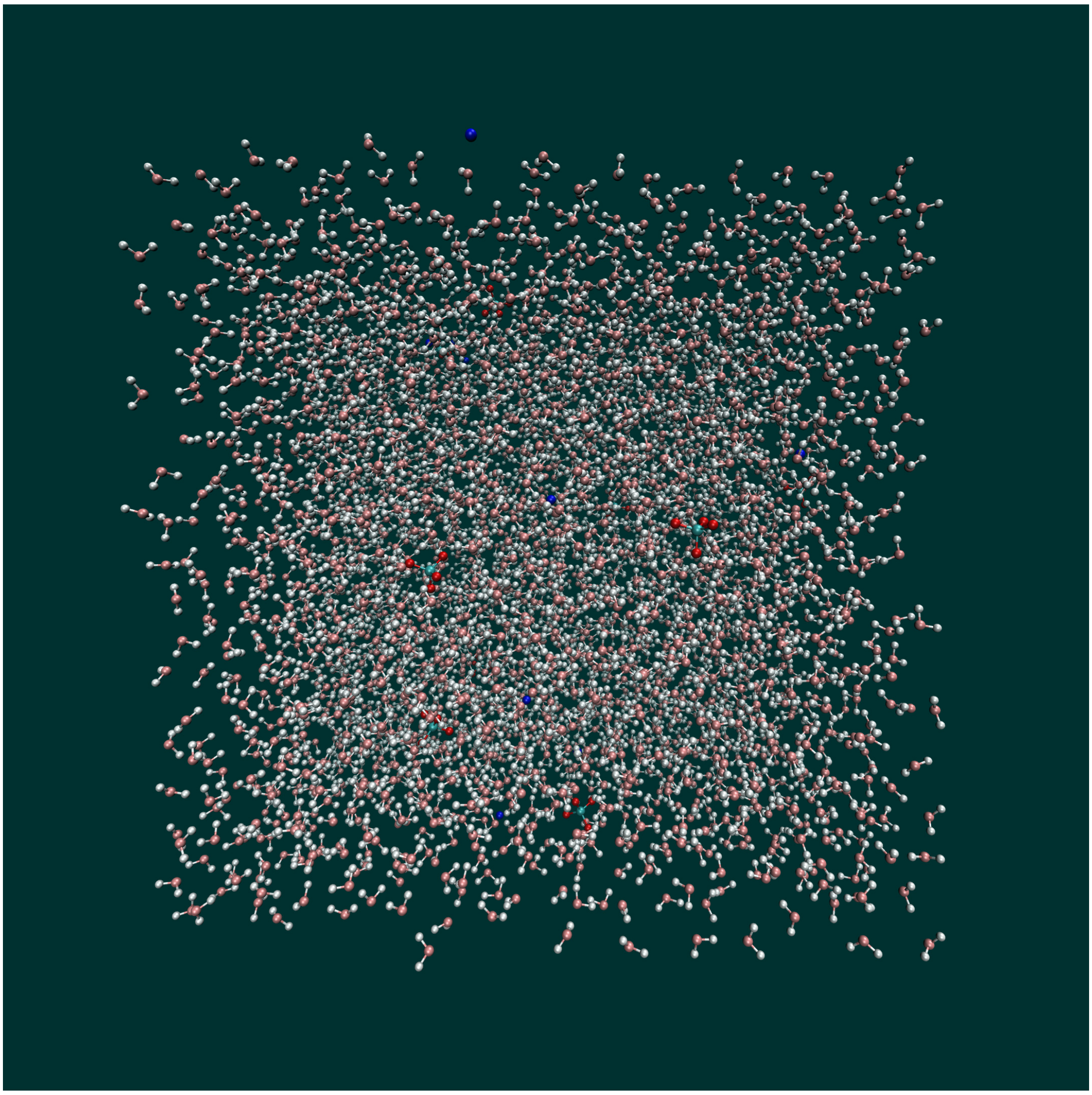

Figure 4.2: Snapshot of a $C_1{}^{NaClO_4} = 1.63$ wt% solution at density $\rho = 1100\,kg/m^3$ and temperature $T = 200\,K$. Water is shown in pink (oxygen) and grey (hydrogens), sodium in blue and perchlorates in teal (chlorine) and red (oxygens).

DENSITY	BOX LENGTH
880 kg/m^3	5.206 nm
890 kg/m^3	5.186 nm
900 kg/m^3	5.167 nm
910 kg/m^3	5.148 nm
920 kg/m^3	5.129 nm
930 kg/m^3	5.111 nm
940 kg/m^3	5.092 nm
950 kg/m^3	5.074 nm
960 kg/m^3	5.057 nm
970 kg/m^3	5.039 nm
980 kg/m^3	5.022 nm
990 kg/m^3	5.005 nm
1000 kg/m^3	4.988 nm
1010 kg/m^3	4.972 nm
1020 kg/m^3	4.956 nm
1030 kg/m^3	4.940 nm
1040 kg/m^3	4.924 nm
1050 kg/m^3	4.908 nm
1060 kg/m^3	4.892 nm
1070 kg/m^3	4.877 nm
1080 kg/m^3	4.862 nm
1090 kg/m^3	4.847 nm
1100 kg/m^3	4.832 nm
1110 kg/m^3	4.818 nm
1120 kg/m^3	4.804 nm
1130 kg/m^3	4.789 nm
1140 kg/m^3	4.775 nm

Table 4.2: Simulated densities for the $C_1^{NaClO_4}$ solution with the corresponding box lengths.

For the $C_1^{\mathrm{NaClO_4}}$ solution, the density in the simulations was gradually reduced from 1140 kg/m^3 down to the liquid-gas limit of mechanical stability (LG-LMS), which was recognised by the onset of *cavitation*: the formation of vapour bubbles in the region where the system pressure is negative (and where the stable phase is gas), a process that led to a sudden increase in the system's pressure (Lascaris, 2022).

For this solution, the LG-LMS was identified with the 880 kg/m^3 isochore.

A snapshot of the solution at density 1100 kg/m^3 and temperature 200 K is shown in Fig. 4.2.

4.2.1 *The Equation of State in the Isochore Plane*

A representation of the equation of state of the $C_1^{\mathrm{NaClO_4}}$ solution is shown in Fig. 4.3. Each point represents a simulated state point of the system and each line an isochore.

To emphasise the relatively similar (though not identical) behaviour by the solution and the bulk, the respective isochores at 960 kg/m^3 have been highlighted in black for both.

As discussed in the introductory chapter, when studying the phase diagram of water and aqueous solutions, one of the most well-known anomalies encountered is the presence of a temperature of maximum density. Local maxima of the isobars also exist and define the Temperatures of Minimum Density (TmD).

By definition, these stationary points coincide with the state points at which the coefficient of thermal expansion at constant pressure

$$\alpha_P = \frac{1}{V}\left.\frac{\partial V}{\partial T}\right|_p \tag{4.2}$$

is nullified.

By expanding

$$dp = \left.\frac{\partial p}{\partial T}\right|_V dT + \left.\frac{\partial p}{\partial V}\right|_T dV$$

at constant pressure, $dp = 0$, the following holds

$$\left.\frac{\partial p}{\partial T}\right|_V = -\left.\frac{\partial p}{\partial V}\right|_T \left.\frac{\partial V}{\partial T}\right|_p \tag{4.3}$$

and thus we can obtain

$$\alpha_p = \underbrace{-\frac{1}{V}\left.\frac{\partial V}{\partial p}\right|_T}_{\kappa_T} \left.\frac{\partial p}{\partial T}\right|_V , \tag{4.4}$$

κ_T being the isothermal compressibility, which for a mechanically stable liquid satisfies

$$\kappa_T > 0. \tag{4.5}$$

TEMPERATURE	EQUILIBRATION TIME	PRODUCTION TIME
400 K	0.1 ns	0.1 ns
380 K	0.1 ns	0.1 ns
350 K	0.1 ns	0.1 ns
330 K	0.1 ns	0.1 ns
315 K	0.1 ns	0.1 ns
305 K	0.1 ns	0.1 ns
300 K	0.1 ns	0.1 ns
295 K	0.1 ns	0.1 ns
290 K	0.1 ns	0.1 ns
285 K	0.1 ns	0.1 ns
280 K	0.5 ns	0.5 ns
275 K	0.5 ns	0.5 ns
270 K	0.5 ns	0.5 ns
265 K	0.5 ns	0.5 ns
260 K	1 ns	1 ns
255 K	1 ns	1 ns
250 K	1 ns	1 ns
245 K	1 ns	1 ns
240 K	10 ns	10 ns
230 K	10 ns	10 ns
220 K	20 ns	20 ns
210 K	20 ns	20 ns
200 K	40 ns	40 ns
190 K	40 ns	40 ns
180 K	40 ns	40 ns
175 K	40 ns	40 ns
170 K	40 ns	40 ns

Table 4.3: Simulation times for the ${C_1}^{NaClO_4}$ solution.

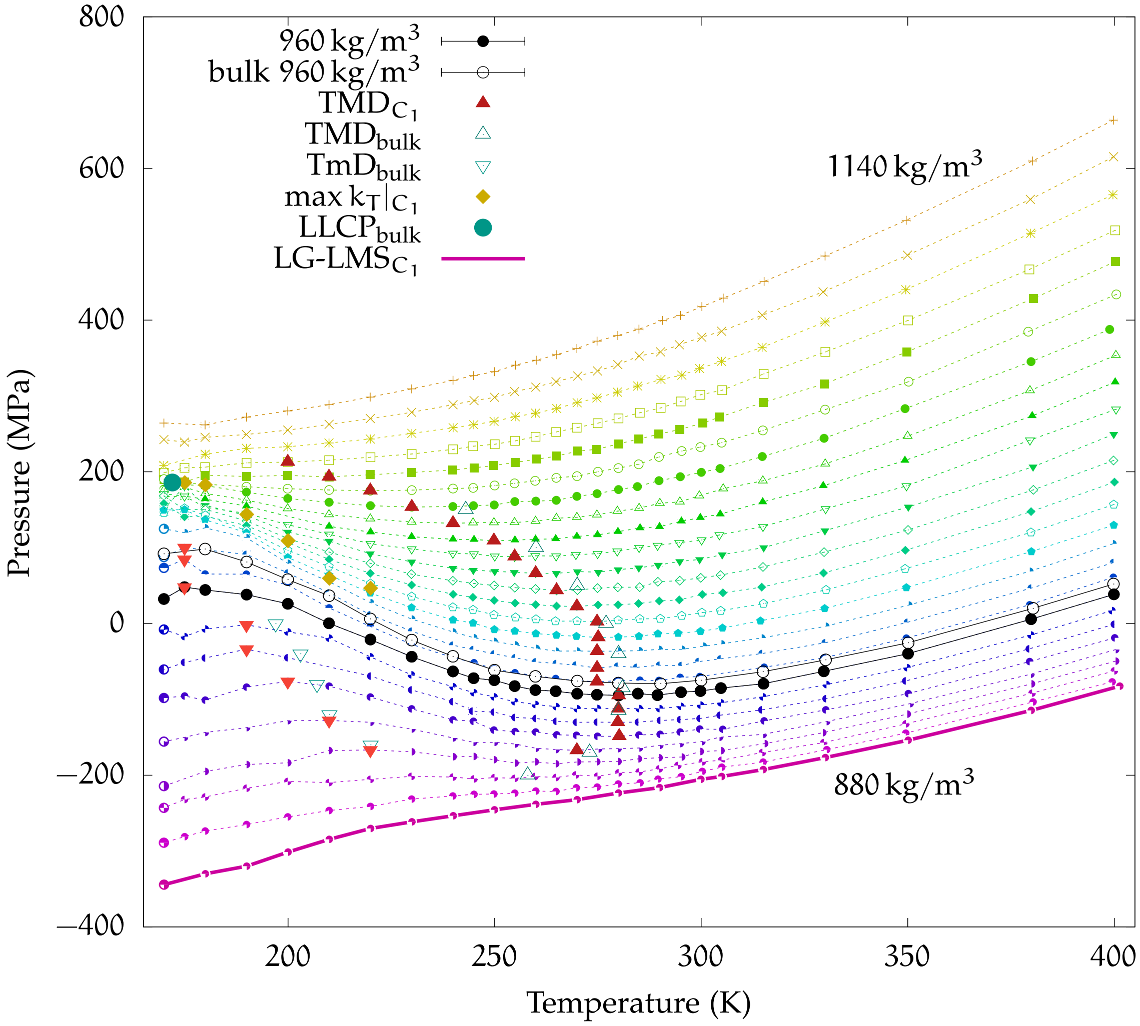

Figure 4.3: Unfitted simulated state points of the $C_1{}^{NaClO_4}$ solution in the (p, T) plane, for densities ranging from $\rho = 880\,\mathrm{kg/m^3}$ to $\rho = 1140\,\mathrm{kg/m^3}$, with increments $\Delta\rho = 10\,\mathrm{kg/m^3}$ and temperatures from $T = 400\,\mathrm{K}$ to $T = 170\,\mathrm{K}$. The symbols represent state points derived from simulations, while the lines serve as a visual guide. Error bars are plotted but not visible. Included are initial estimates of the Temperature of Maximum Density (TMD) curves for the solution, shown as red-filled upward triangles, alongside bulk data (empty teal upward triangles) from Biddle et al., 2017. Downward triangles denote the TmDs. The teal-filled circle marks the bulk Liquid-Liquid Critical Point (LLCP) as per Debenedetti et al., 2020 and filled diamonds indicate the isothermal compressibility maxima obtained from the data. The thick dash-dotted line at the bottom represents the $880\,\mathrm{kg/m^3}$ isochore, coinciding with the system's Liquid-Gas Limit of Mechanical Stability (LG-LMS). The $960\,\mathrm{kg/m^3}$ isochore data for both the C_1 solution (filled black circles) and the bulk (empty black circles) is highlighted. Further refined estimates of the TMDs, TmDs and isothermal compressibility maxima will be provided subsequently.

Hence

$$\alpha_p = 0 \mapsto \left.\frac{\partial p}{\partial T}\right|_V = 0, \tag{4.6}$$

i.e. the boundaries of the density anomaly region coincide with the stationary points of the isochores, as Eq. (4.3) suggested.

Rewriting Eq. (4.3) as

$$\left.\frac{\partial p}{\partial T}\right|_\rho = - \left.\frac{\partial p}{\partial \rho}\right|_T \left.\frac{\partial \rho}{\partial T}\right|_p \tag{4.7}$$

and differentiating it we obtain

$$\left.\frac{\partial^2 p}{\partial T^2}\right|_\rho = - \left.\frac{\partial p}{\partial \rho}\right|_T \left.\frac{\partial^2 \rho}{\partial T^2}\right|_p . \tag{4.8}$$

From Eq. (4.5) and Eq. (4.8) it follows that $p(T)|_V$ and $\rho(T)|_p$ have opposite concavities for mechanically stable liquids, hence the isochores' minima mark the TMD curve, while their maxima are localised on the TmD curve.

An initial estimate of the positions of these two curves is also portrayed in Fig. 4.3, alongside the bulk behaviour known from the literature (refer to Biddle et al., 2017). These points were determined by highlighting the isochore minima and maxima in the region of water anomalies, as directly obtained by the simulations.

Additionally, estimates have been made for the peaks of isothermal compressibility and the specific state points at which they manifest. Hereafter, we will provide a better estimate of both the TMD and TmD curves as well as the maxima of isothermal compressibility.

Fig. 4.3 also shows bulk water's LLCP obtained in Debenedetti et al., 2020.

In order to provide a more accurate localisation of the region of density anomaly (i.e. where density increases upon heating along constant pressure paths) of the solution under investigation, the isochore curves were modelled using sixth-degree polynomials.[1]

Fig. 4.4 thus shows the positions of the TMD and TmD points obtained by identifying the minima and maxima of the fitted polynomials, respectively.

A necessary condition for the LLCP

A second order critical point is characterised by the condition

$$\left.\frac{\partial p}{\partial \rho}\right|_{T_C} = 0, \tag{4.9}$$

indicating the presence of an inflexion point with a horizontal tangent in the isotherm plane, which will be investigated in the following section.

Within the (p, T) plane, instead, when considering a discrete set of isochores, Eq. (4.9) leads to

$$\frac{p(T_C, \rho)}{\Delta\rho} = \frac{p(T_C, \rho + \Delta\rho)}{\Delta\rho}, \tag{4.10}$$

---

[1] The 1130, 990, and 930 kg/m^3 isochores have been also fitted with fourth-degree polynomials (not shown), providing a trend akin to that reported here albeit with slightly diminished accuracy. Hence, higher polynomial orders were considered.

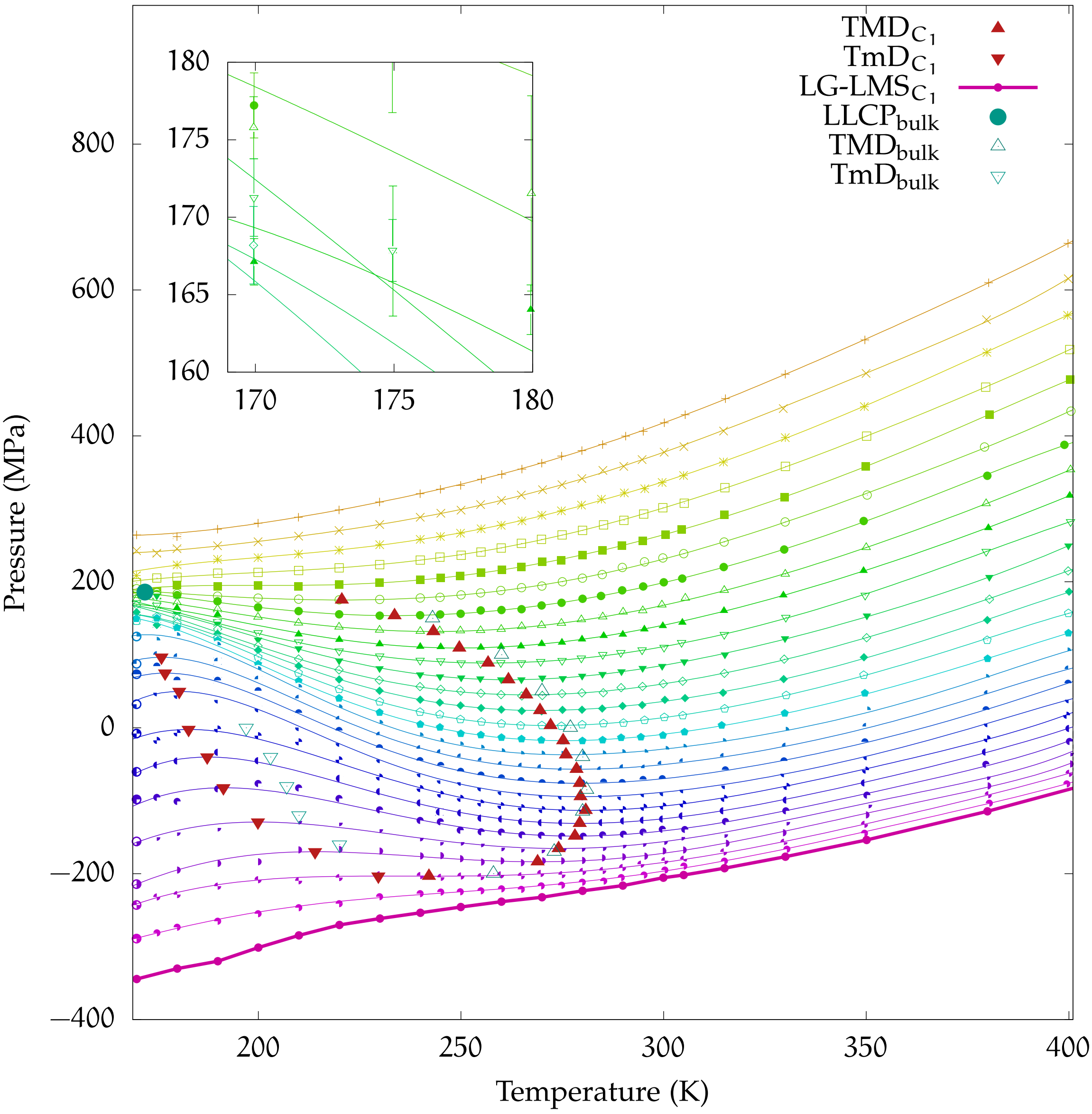

Figure 4.4: Equation of state in the isochore plane for the $C_1^{NaClO_4}$ solution obtained from MD simulations covering densities ranging from $\rho = 1140\,\mathrm{kg/m^3}$ to $880\,\mathrm{kg/m^3}$ (LG-LMS) with an incremental change of $\Delta\rho = 10\,\mathrm{kg/m^3}$. Error bars are plotted but only visible in the inset. Polynomial fittings have been applied to the simulated data points and the resulting isochores are reported with solid lines. The teal-filled circle is the TIP4P/2005 bulk LLCP as computed in Debenedetti et al., 2020. The solution's TMDs (upward triangles) and the TmDs (downward triangles) obtained from the fits are highlighted in red and compared to the values known in literature for the bulk TIP4P/2005 (see Biddle et al., 2017) and here reported with teal empty triangles. Notably, the $1050\,\mathrm{kg/m^3}$ and the $1060\,\mathrm{kg/m^3}$ isochores cross at 175 K.

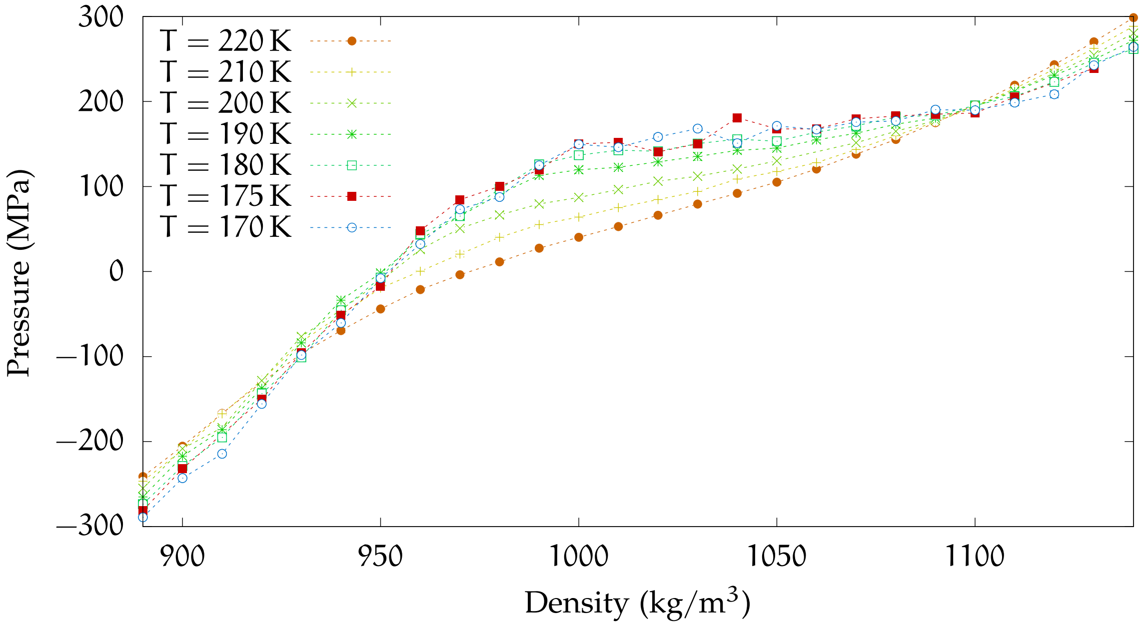

Figure 4.5: Simulated state points for the $C_1{}^{NaClO_4}$ solution plotted in the isotherm plane. The dashed lines are a guide for the eye. Highlighted by red squares are the points at 175 K, the closest temperature to where the crossing was identified in the isochore plane.

implying that the critical region is located at the crossing of the isochores that occurs at the highest temperature within the region of density anomaly. This intersection, for the set of densities considered in Fig. 4.4, occurs at $T = 173.4\,K$, between isochores at $\rho = 1050\,kg/m^3$ and $\rho = 1060\,kg/m^3$.

Therefore, we proceed to study the equation of state of the system in the isotherm plane limited to temperatures and densities close to these values.

4.2.2 *The Equation of State in the Isotherm Plane*

The outcomes of the simulations can be depicted in the isotherm plane, plotting pressure p against density ρ. By focusing on the state points within the vicinity of the critical zone, discerned through the crossing of the isochores, the plot in Fig. 4.5 is obtained. In this figure, the isotherm corresponding to the nearest simulated temperature to the said intersection is highlighted by red squares.

The simulated state points have been fitted with fifth order polynomials, to account not only for the overall concavity of the curves but also for the flattening observed in the central area as the critical temperature is approached. This flattening results in the occurrence of an inflexion point with a horizontal tangent, defining the critical point itself, as indicated by Eq. (4.9). The isotherm curves $p_T(\rho)$ are illustrated in Fig. 4.6, with the horizontal inflexion point occurring at a temperature $170\,K < T < 175\,K$.

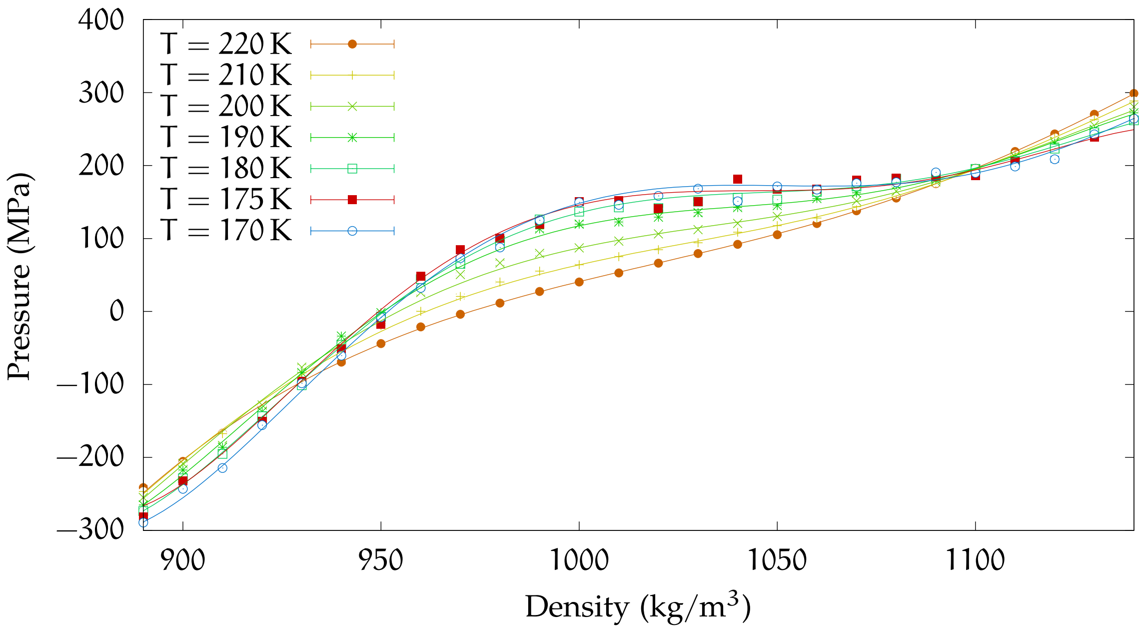

Figure 4.6: Equation of state in the isotherm plane for the $C_1^{NaClO_4}$ solution. Error bars are plotted but not visible. Lines are isotherm curves $p_T(\rho)$ obtained through polynomial fits to the simulated state points. Highlighted in red is the isotherm at 175 K, the closest temperature to where the crossing was identified in the isochore plane.

4.2.3 *On the Singularities Approaching the Transition*

With the dual aim of both calculating the critical point and completing the study of water's anomalies, we can now proceed to determine the behaviour of the isothermal compressibility, defined as

$$\kappa_T = -\frac{1}{V}\left.\frac{\partial V}{\partial p}\right|_T , \tag{4.11}$$

which, for the set of densities ρ_i considered in the isotherms $p_T(\rho)$ in Fig. 4.6, can be expressed as

$$\kappa_{T_i} = \frac{1}{\rho_i}\left.\frac{\partial \rho_i}{\partial p}\right|_T = \frac{1}{\rho_i}\frac{1}{\left.\frac{\partial p_T(\rho)}{\partial \rho}\right|_{\rho=\rho_i}} . \tag{4.12}$$

The Widom Line

In Fig. 4.7 the graph of κ_T vs p is reported.

As established in the literature (Parisi, 1998; Franzese and Stanley, 2007), second-order phase transitions, the liquid-liquid transition in TIP4P/2005 being one of which as validated in Debenedetti et al., 2020, are marked by the emergence of precursor phenomena. These phenomena are characterised by diverging response functions as they approach the second-order critical point.

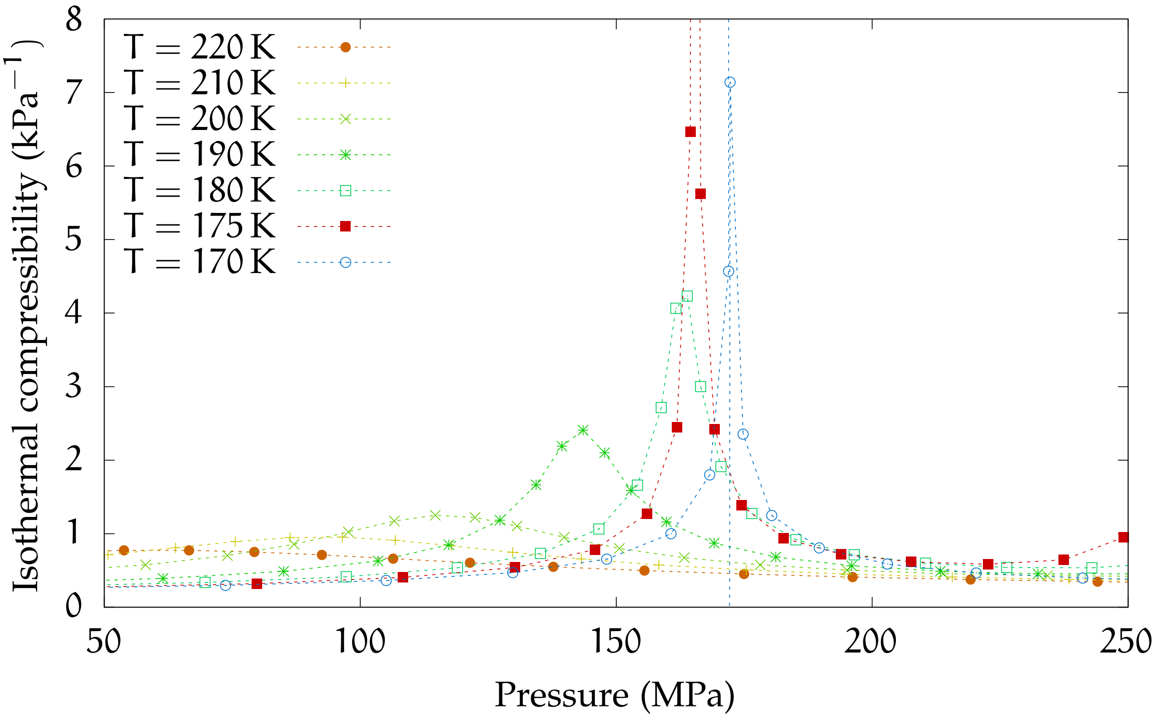

Figure 4.7: Isothermal compressibility κ_T vs pressure p for the $C_1^{NaClO_4}$ solution for temperatures ranging from 220 K to 170 K.

As an important example of this, according to the calculations led by Debenedetti et al., the bulk TIP4P/2005 exhibits near the critical point a singular behaviour

$$\kappa_T \sim (T - T_C)^{-\gamma} \quad \gamma = 1.26 \quad T \to T_C\,,$$

which places TIP4P/2005 in the Ising universality class.

The singularities in these response functions are tied to the presence of a diverging correlation length. The theory of critical phenomena further proves that within the single-phase region, a line of correlation length maxima, known as the Widom Line, emerges. This leads to the observation that the isothermal compressibility, along with other response functions, displays pronounced lines of maxima that align with and converge towards the Widom Line in proximity to the critical point (Kim et al., 2017; Xu et al., 2005; Abascal and Vega, 2010; Gallo and Rovere, 2012; De Marzio et al., 2016; Lupi et al., 2021).

The peaks of isothermal compressibility can be used as a proxy for identifying the Widom Line.

To further refine the phase diagram calculation, besides the LLCP, it is necessary to identify the pressures corresponding to the maxima of isothermal compressibility within the considered temperature range. The plot of $\kappa_T(p)$, as reported in Fig. 4.7, exhibits very sharp peaks at both 175 K and 170 K.

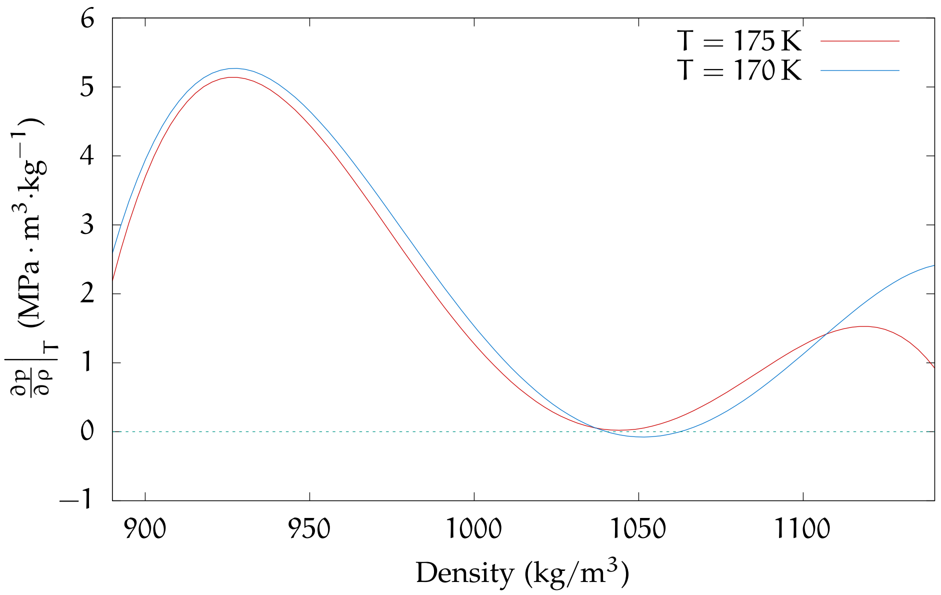

Figure 4.8: Derivative of $p_T(\rho)$ for the two simulated temperatures closest to the critical point for the $C_1^{\mathrm{NaClO_4}}$ solution.

Analysing (Fig. 4.8) the derivative of the isotherms $\frac{\partial p_T(\rho)}{\partial \rho}$ it is revealed that neither of these temperatures coincides precisely with the critical point, which is characterised by

$$\frac{\partial p}{\partial \rho}\bigg|_T = 0\,.$$

Let ρ^* be the point of minimum of the isotherm derivative.

Therefore, Fig. 4.9 displays the minima of the isotherm derivatives

$$\frac{\partial p_T(\rho^*)}{\partial \rho}$$

within the investigated temperature range. The pattern appears to be consistent with a linear trajectory and the intersection between the linear fit and the horizontal axis provides an estimated critical temperature of

$$T_C = 173.3\,\mathrm{K}\,.$$

In order to determine the critical pressure, the values of p_T derived from the isotherms at their derivatives' points of minimum ρ^* were plotted against their respective temperatures in Fig. 4.10. The values of $p_T(\rho^*)$ were then fitted with a quadratic polynomial.

This approach yielded an estimated critical pressure of

$$p_C = p(T_C) = 169.4\,\mathrm{MPa}\,.$$

A linear fit of the inflexion densities is shown in Fig. 4.11, from which a critical density of

$$\rho_c = \rho(T_C) = 1049.6\,\mathrm{kg/m^3}$$

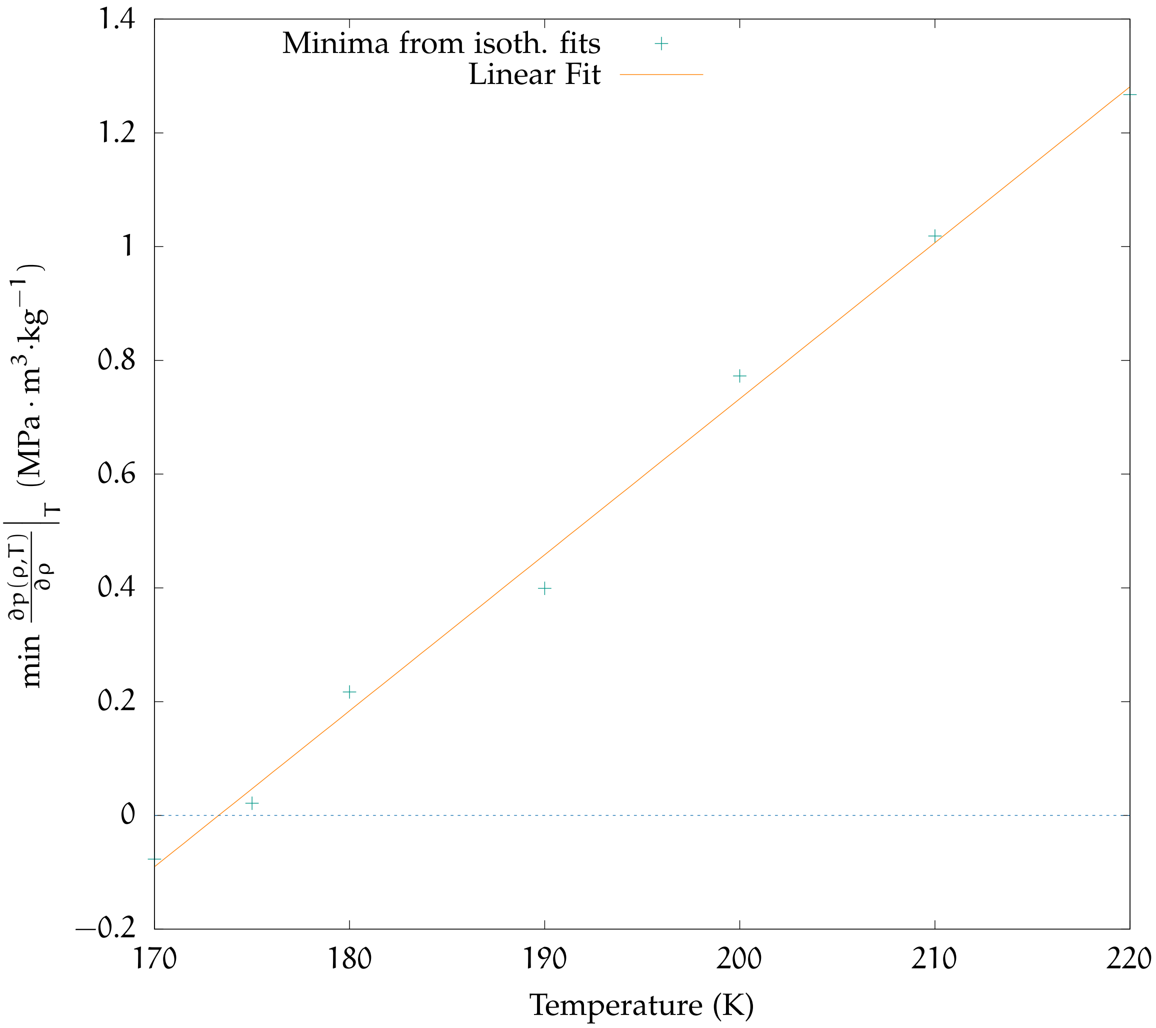

Figure 4.9: Minimum values of the derivative of the isothermal curves $p_T(\rho)$ in the region of the density anomalies fitted with a straight line for the $C_1^{NaClO_4}$ solution. As per (4.9), the intersection of the fit and the x-axis provides an estimate of the critical temperature resulting in $T_C = 173.3\,K$.

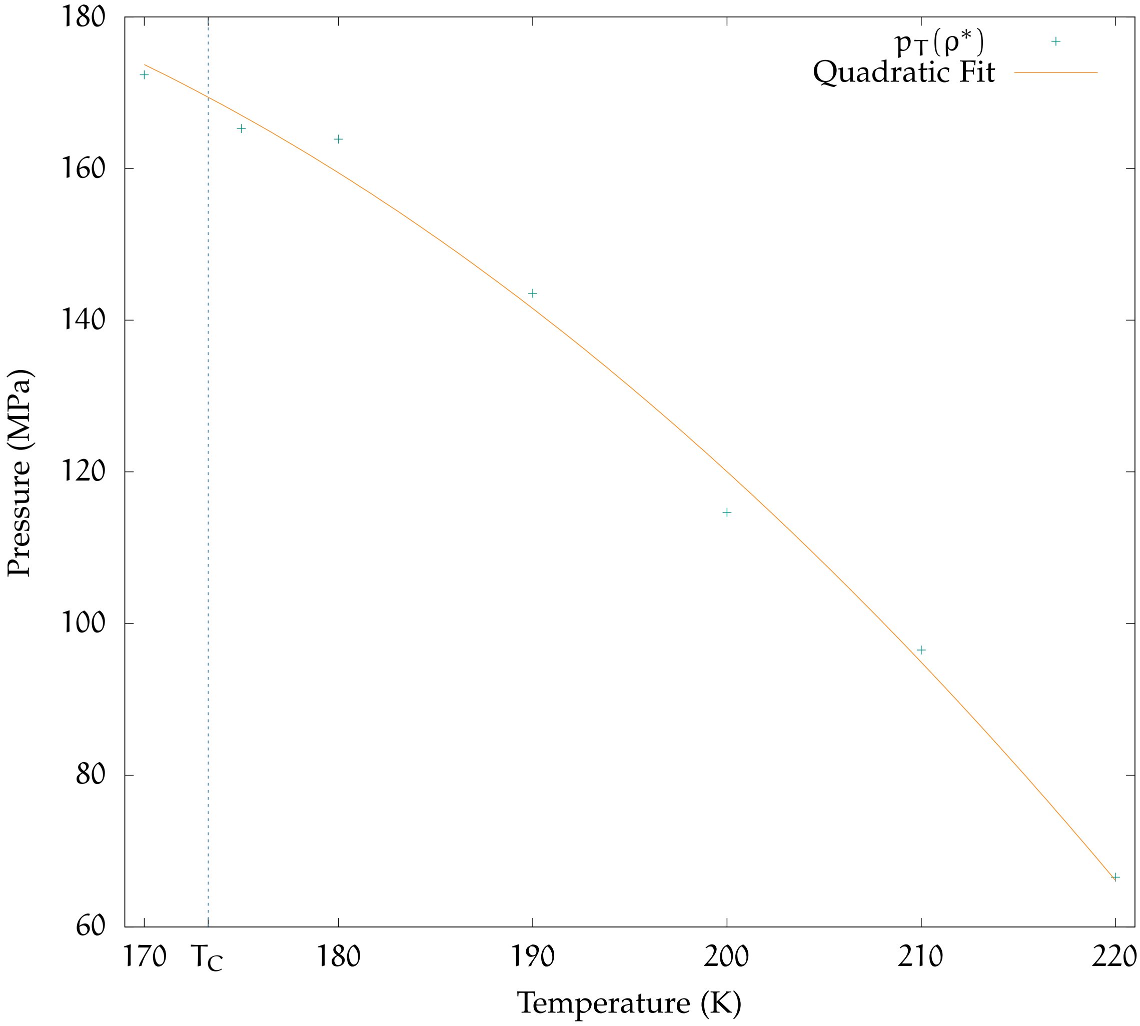

Figure 4.10: Pressure values corresponding to the temperatures at the isotherm inflexion points, fitted with a quadratic curve. At the critical temperature, the pressure is determined to be $p_C = 169.4\,\mathrm{MPa}$.

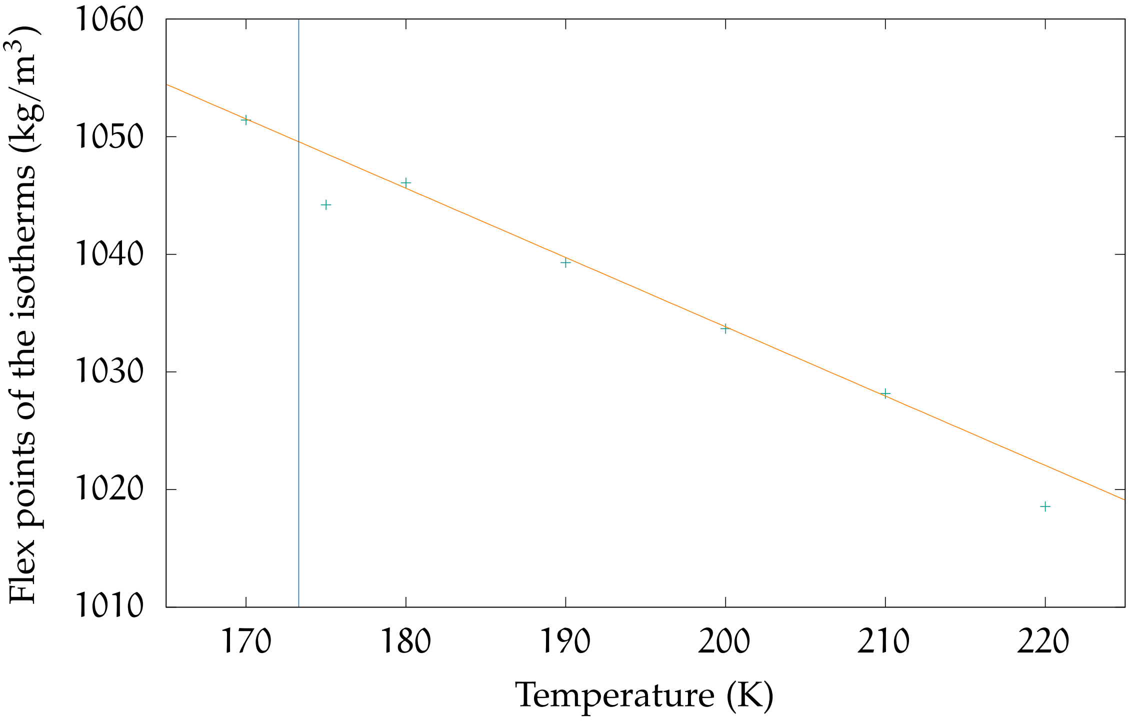

Figure 4.11: Densities at the flex points of the isotherm curves for the ${C_1}^{NaClO_4}$ solution.

is estimated.

Hence, the critical point is:

$$\begin{cases} T_C = 173.3\,\text{K} \\ p_C = 169.4\,\text{MPa} \\ \rho_C = 1049.6\,\text{kg/m}^3. \end{cases}$$

The complete phase diagram of the supercooled ${C_1}^{NaClO_4}$ aqueous solution obtained by this study is reported in Fig. 4.12. In the same figure the phase diagram of the corresponding bulk phase is also reported. The comparison will be discussed in Sec. 4.4.

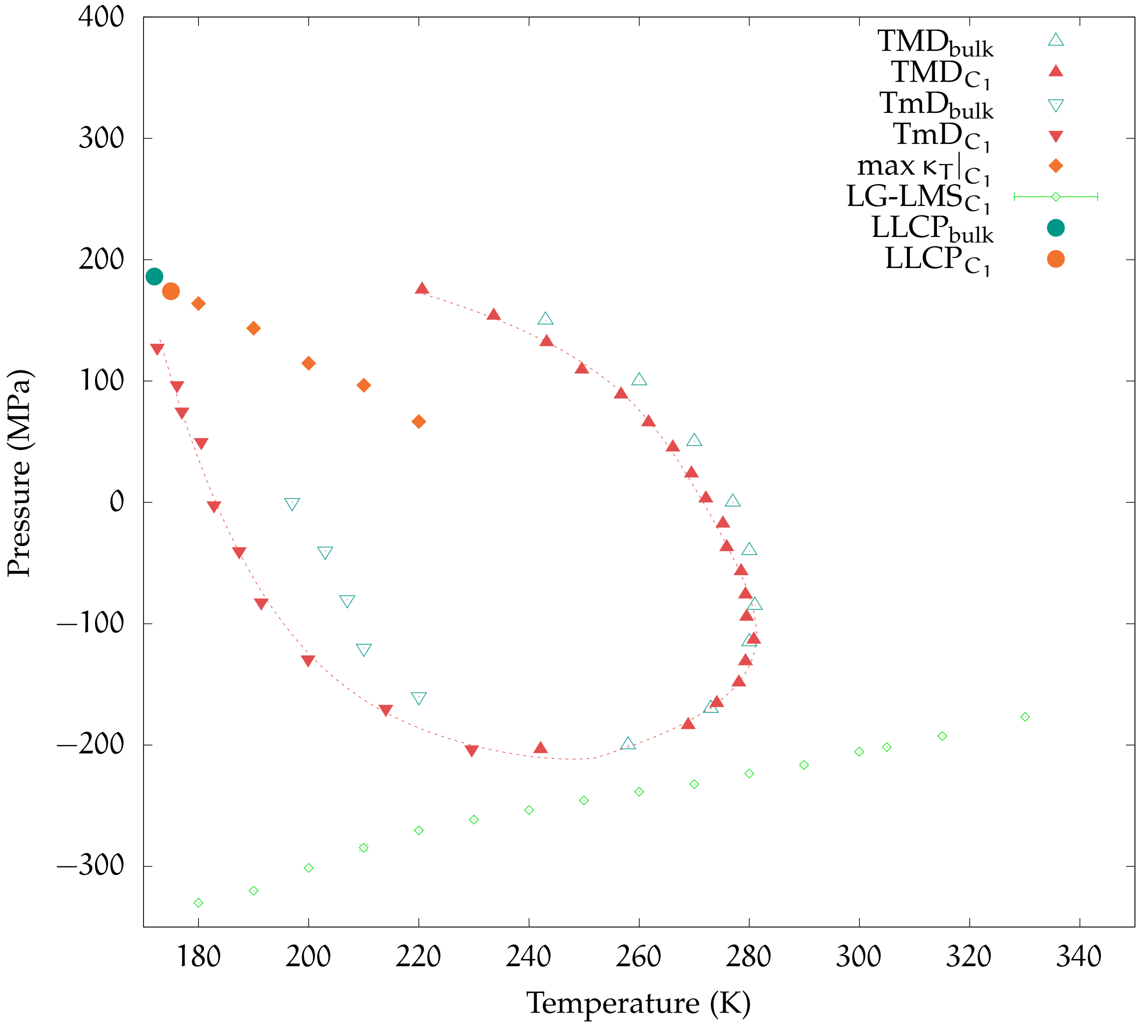

Figure 4.12: Phase diagram of the $C_1^{NaClO_4}$ solution without the isochores. The figure shows the LLCP, the TMD and the TmD curves for the solution compared to the values known in literature for the bulk (Debenedetti et al., 2020; Biddle et al., 2017). The figure also shows the LG-LMS and the state points corresponding to the peaks of the isothermal compressibility.

4.3 RESULTS FOR THE ${C_2}^{NaClO_4} = 15.4$ WT% SOLUTION

The second system investigated was the ${C_2}^{NaClO_4} = 15.4\,\mathrm{wt\%}$ solution which was built similarly to the ${C_1}^{NaClO_4}$ solution in Sec. 4.1.

A direct comparison between the two concentrations is reported in Table 4.4.

In order to obtain the ${C_2}^{NaClO_4}$ solution, the number of ions was increased to 100 Na^+ ions and 100 ${ClO_4}^-$ ions, while keeping a comparable number of TIP4P/2005 water molecules as in the ${C_1}^{NaClO_4}$ solution.[2]

In Table 4.5 the selected densities for the system isochores and the linear dimensions of the simulation boxes necessary to achieve them are reported. Also in this case, isochoric simulations were carried out in the canonical ensemble over the temperature range specified in Table 4.6, which further includes the respective equilibration and production times.

To facilitate more effective equilibration of the system at lower temperatures, the system was allowed to equilibrate at the intermediate temperatures of $195\,\mathrm{K}$ and $185\,\mathrm{K}$, where no production runs were performed. The asymptotic thermodynamic values of these points were also used to increase the degrees of freedom for fitting the isochores in the density range $[1100\,\mathrm{kg/m^3}, 1115\,\mathrm{kg/m^3}]$ with eighth-degree polynomials instead of sixth-degree.

The liquid-gas mechanical stability limit was determined, as before, by the occurrence of cavitation, this time observed at $950\,\mathrm{kg/m^3}$. A snapshot of the solution at $1200\,\mathrm{kg/m^3}$ and $200\,\mathrm{K}$ is shown in Fig. 4.13.

The simulated state points for the ${C_2}^{NaClO_4}$ solutions are shown in Fig. 4.14 in the isochore plane.

The C_2 concentration has a clear influence on the thermodynamic properties of the solution, altering them from those observed in bulk water much more than the C_1 concentration did. To quantify this change, Fig. 4.14 displays, similarly to what was done for the ${C_1}^{NaClO_4}$ solution, the isochores at $960\,\mathrm{kg/m^3}$ for both the ${C_2}^{NaClO_4}$ solution and bulk water: in this case, the difference (both in the curvature and in the displacement) between them is evident.

---

[2] In this thesis, the focus is on studying the variation of thermodynamic and structural properties as the concentration increases, which is why a very low initial concentration was chosen and then the number of ions was increased.

	N_{ions}	$N_{water\ molecules}$	CONC. (wt%)	CONC. (NUMB. FRAC.$\times 10^{-3}$)
${C_1}^{NaClO_4}$	20	4099	1.63	2.43
${C_2}^{NaClO_4}$	200	3737	15.4	26.1

Table 4.4: Concentrations of the two $NaClO_4$ solutions investigated expressed both in weight percentage and in number fraction.

DENSITY	BOX LENGTH
950 kg/m^3	5.112 nm
960 kg/m^3	5.094 nm
970 kg/m^3	5.077 nm
980 kg/m^3	5.059 nm
990 kg/m^3	5.042 nm
1000 kg/m^3	5.025 nm
1010 kg/m^3	5.009 nm
1020 kg/m^3	4.992 nm
1030 kg/m^3	4.976 nm
1040 kg/m^3	4.960 nm
1050 kg/m^3	4.944 nm
1060 kg/m^3	4.929 nm
1070 kg/m^3	4.913 nm
1080 kg/m^3	4.898 nm
1090 kg/m^3	4.883 nm
1100 kg/m^3	4.868 nm
1105 kg/m^3	4.861 nm
1110 kg/m^3	4.854 nm
1115 kg/m^3	4.846 nm
1120 kg/m^3	4.839 nm
1130 kg/m^3	4.825 nm
1140 kg/m^3	4.811 nm
1150 kg/m^3	4.797 nm
1160 kg/m^3	4.783 nm
1170 kg/m^3	4.769 nm
1180 kg/m^3	4.756 nm
1190 kg/m^3	4.742 nm
1200 kg/m^3	4.729 nm

Table 4.5: Simulated densities for the $C_2^{NaClO_4}$ solution with the corresponding box lengths.

TEMPERATURE	EQUILIBRATION TIME	PRODUCTION TIME
400 K	0.1 ns	0.1 ns
380 K	0.1 ns	0.1 ns
350 K	0.1 ns	0.1 ns
330 K	0.1 ns	0.1 ns
315 K	0.1 ns	0.1 ns
305 K	0.1 ns	0.1 ns
300 K	0.1 ns	0.1 ns
295 K	0.1 ns	0.1 ns
290 K	0.1 ns	0.1 ns
285 K	0.1 ns	0.1 ns
280 K	0.5 ns	0.5 ns
275 K	0.5 ns	0.5 ns
270 K	0.5 ns	0.5 ns
265 K	0.5 ns	0.5 ns
260 K	1 ns	1 ns
255 K	1 ns	1 ns
250 K	1 ns	1 ns
245 K	1 ns	1 ns
240 K	10 ns	10 ns
230 K	10 ns	10 ns
220 K	20 ns	20 ns
210 K	20 ns	20 ns
200 K	40 ns	40 ns
195 K	40 ns	
190 K	40 ns	40 ns
185 K	40 ns	
180 K	40 ns	40 ns
175 K	40 ns	40 ns
170 K	40 ns	40 ns

Table 4.6: Simulation times for the $C_2^{NaClO_4}$ solution.

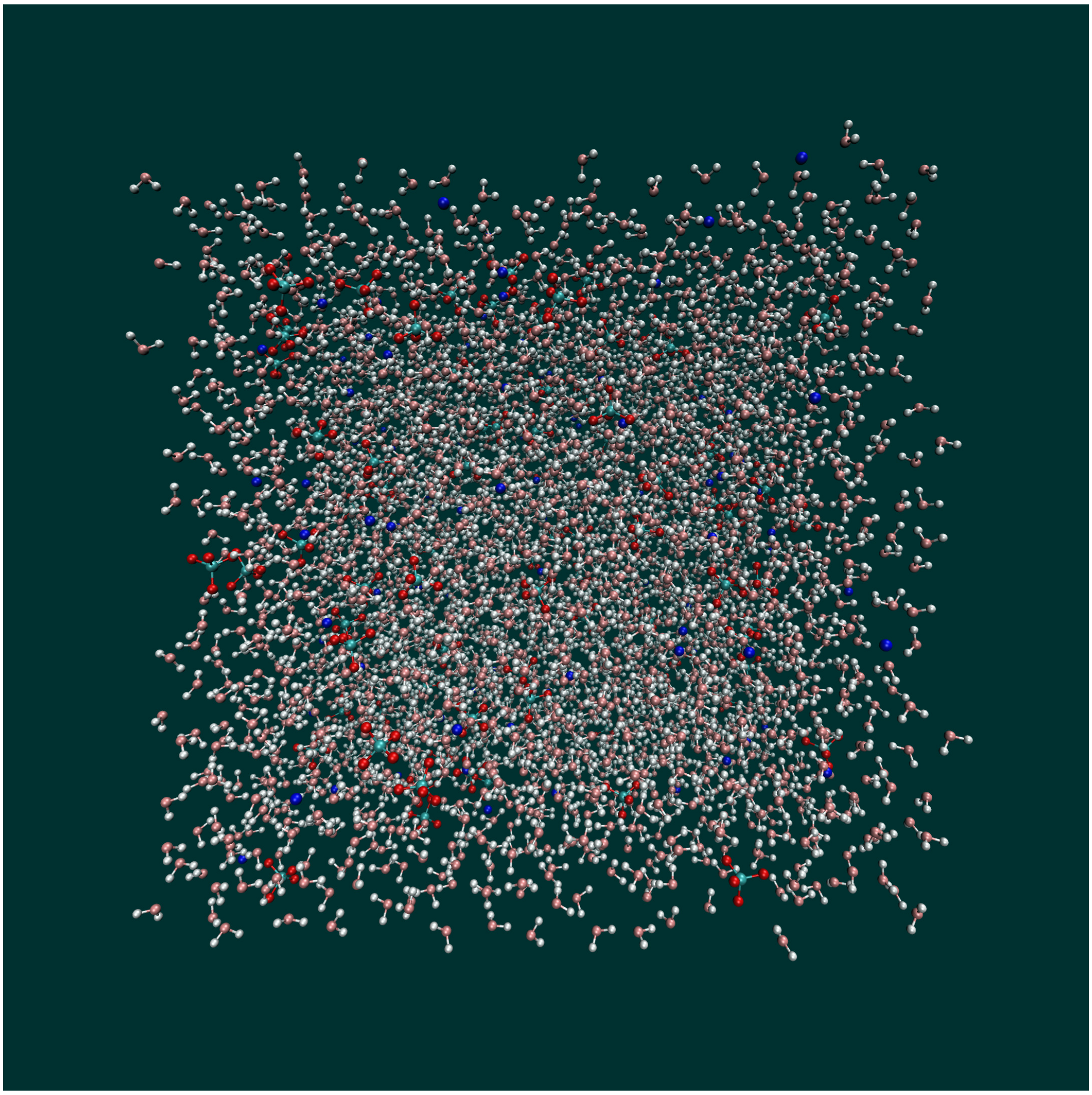

Figure 4.13: Snapshot of a $C_2^{NaClO_4} = 15.4\,\text{wt\%}$ solution at density $\rho = 1200\,\text{kg/m}^3$ and temperature $T = 200\,\text{K}$. Water is shown in pink (oxygen) and grey (hydrogens), sodium in blue and perchlorates in teal (chlorine) and red (oxygens).

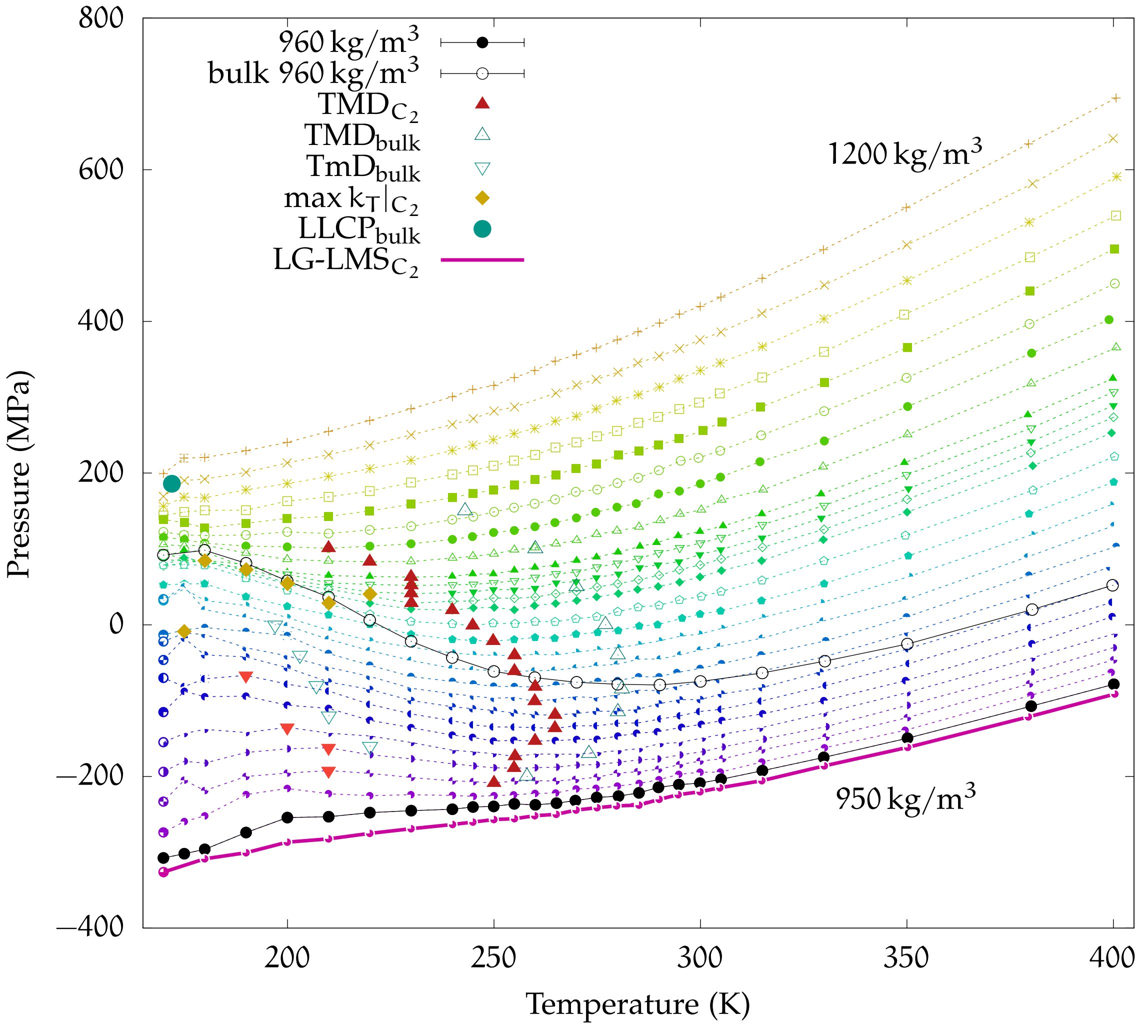

Figure 4.14: Unfitted simulated state points of the $C_2^{NaClO_4}$ solution in the (p, T) plane, for and temperatures ranging from $T = 400\,K$ to $T = 170\,K$ and densities from $\rho = 950\,kg/m^3$ to $\rho = 1200\,kg/m^3$, with increments $\Delta\rho = 10\,kg/m^3$ except in the region $[1100\,kg/m^3, 1120\,kg/m^3]$ where it is $\Delta\rho = 5\,kg/m^3$. The symbols represent state points derived from simulations, while the lines serve as a visual guide. Error bars are plotted but not visible. Included are initial estimates of the Temperature of Maximum Density (TMD) curves for the solution, shown as red-filled upward triangles, alongside bulk data (empty teal upward triangles) from Biddle et al., 2017. Downward triangles denote the TmDs. The teal-filled circle marks the bulk Liquid-Liquid Critical Point (LLCP) as per Debenedetti et al., 2020 and filled diamonds indicate the isothermal compressibility maxima obtained from the data. The thick dash-dotted line at the bottom represents the $950\,kg/m^3$ isochore, coinciding with the system's Liquid-Gas Limit of Mechanical Stability (LG-LMS). The $960\,kg/m^3$ isochore data for both the $C_2^{NaClO_4}$ solution (filled black circles) and the bulk (empty black circles) is highlighted. Further refined estimates of the thermodynamic anomalies will be provided subsequently.

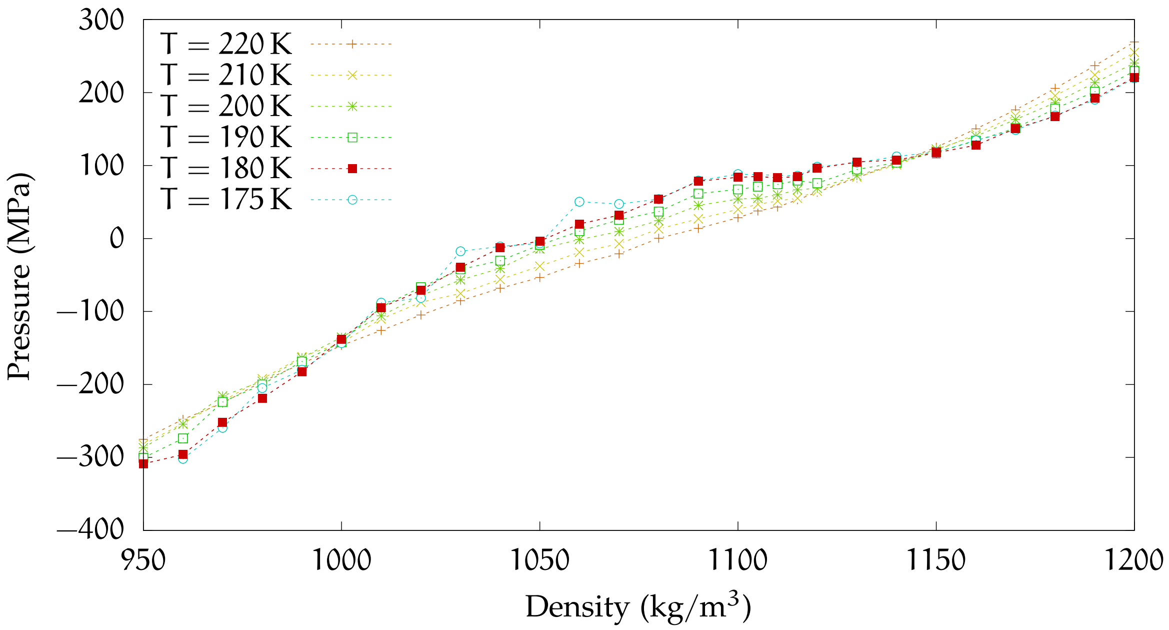

Figure 4.15: Simulated state points for the $C_2^{\mathrm{NaClO_4}}$ solution plotted in the isotherm plane. The dashed lines are a guide for the eye.

The same figure also presents a first estimate of the TMD and the TmD curves for the $C_2^{\mathrm{NaClO_4}}$ solution compared to the bulk phase. For this particular concentration, these two lines look to be shifting towards lower temperatures and pressures.

Simulated state points for selected temperatures and densities are shown in Fig. 4.15 in the isotherm plane in which is evident that the curves flatten out at a temperature of 180 K and a pressure of about 85 MPa, in a density range around 1110 kg/m^3.

A full representation of the system's equation of state, comprehensive of the fitted isochores, is shown in Fig. 4.16.

The TMD and the TmD points obtained from the fits in Fig. 4.16 follow the trend already highlighted in Fig. 4.14, shifting towards lower temperatures and pressures.

The 1110 kg/m^3 and the 1115 kg/m^3 isochores cross approximately at 180 K.

We can now proceed to study the equation of state of the system in the isotherm plane limited to temperatures and densities close to these values. The fitted isotherms are plotted in Fig. 4.17. A flattening of the $p_{180\,\mathrm{K}}$ curve at the flex point is evident, which marks our estimate of the critical temperature

$$T_C = 180\,\mathrm{K}.$$

Fig. 4.18 shows the derivative of the isotherm curve at 180 K compared with that at 175 K, the immediately lower investigated temperature. From the minimum of the 180 K curve, very close to zero, it is possible to estimate the critical density

$$\rho_C = 1110\,\mathrm{kg/m^3}.$$

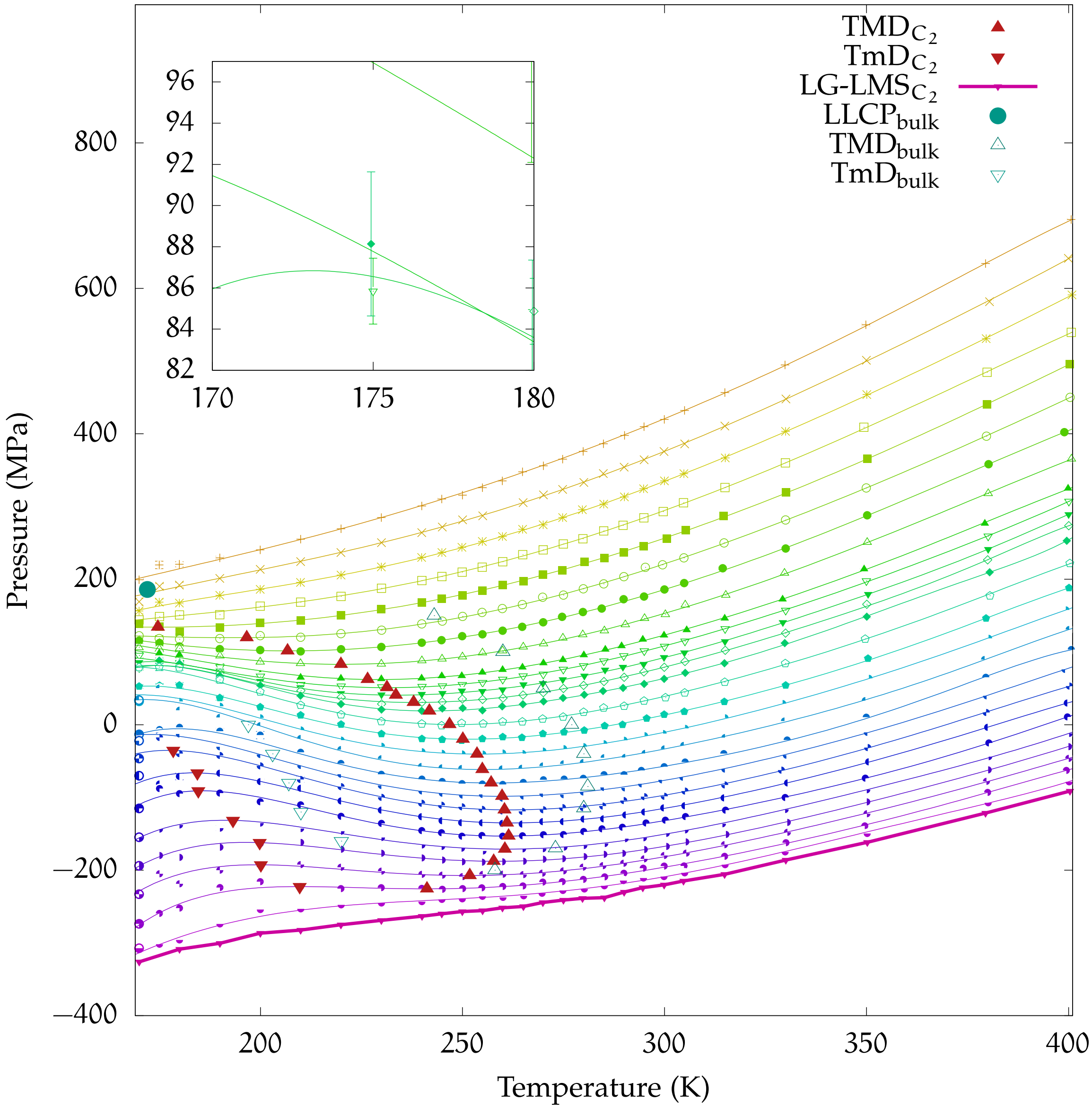

Figure 4.16: Equation of state in the isochore plane for the $C_2^{NaClO_4}$ solution obtained from MD simulations covering densities ranging from $\rho = 1200\,kg/m^3$ to $950\,kg/m^3$ (LG-LMS) with with increments $\Delta\rho = 10\,kg/m^3$ except in the region $[1100\,kg/m^3, 1120\,kg/m^3]$ where it is $\Delta\rho = 5\,kg/m^3$. Error bars are plotted but only visible in the inset. Polynomial fittings have been applied to the simulated data points and the resulting isochores are reported with solid lines. The teal-filled circle is the TIP4P/2005 bulk LLCP as computed in Debenedetti et al., 2020. The solution's TMDs (upward triangles) and the TmDs (downward triangles) obtained from the fits are highlighted in red and compared to the values known in literature for the bulk TIP4P/2005 (see Biddle et al., 2017) and here reported with teal empty triangles. Notably, the $1110\,kg/m^3$ and the $1115\,kg/m^3$ isochores cross approximately at 180 K.

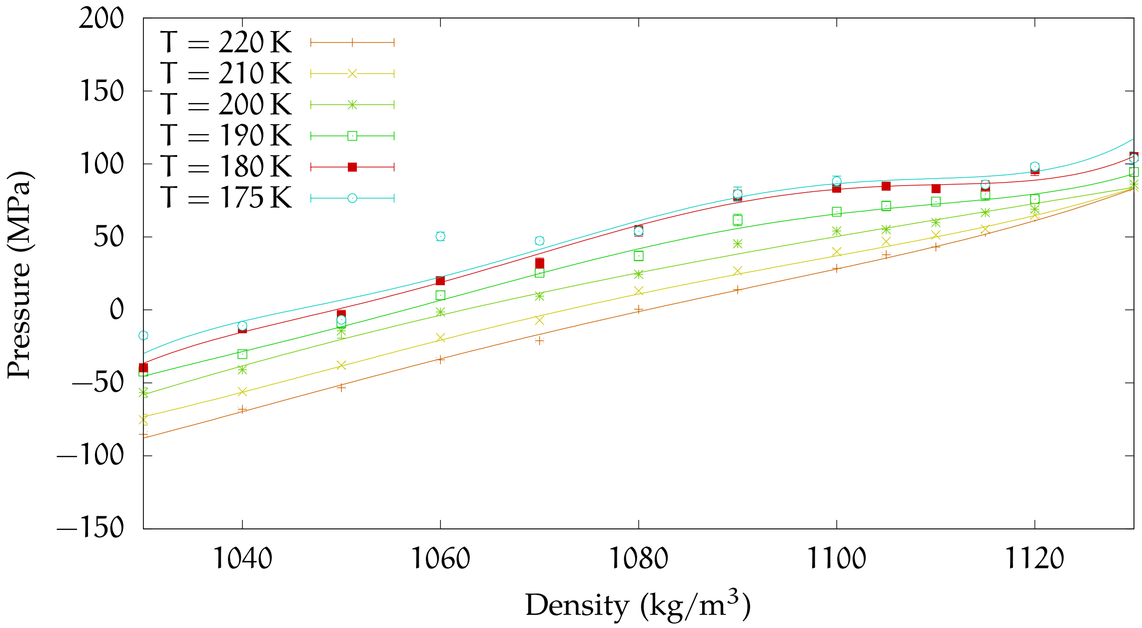

Figure 4.17: Equation of state in the isotherm plane for the $C_2^{NaClO_4}$ solution. Error bars are plotted but not visible. Lines are isotherm curves $p_T(\rho)$ obtained through polynomial fits to the simulated state points. Highlighted in red is the isotherm at 180 K, the closest temperature to where the isochores resulted to be crossing.

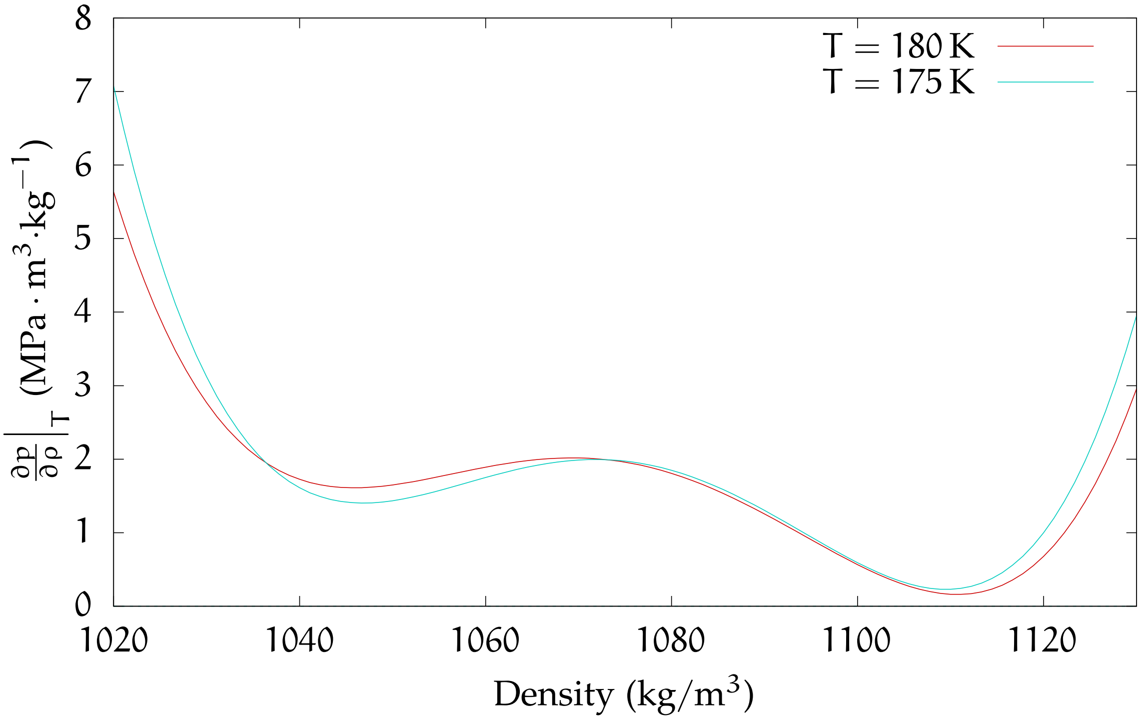

Figure 4.18: Derivative of $p_T(\rho)$ for the $C_2^{NaClO_4}$ solution at the simulated temperatures closest to the critical region.

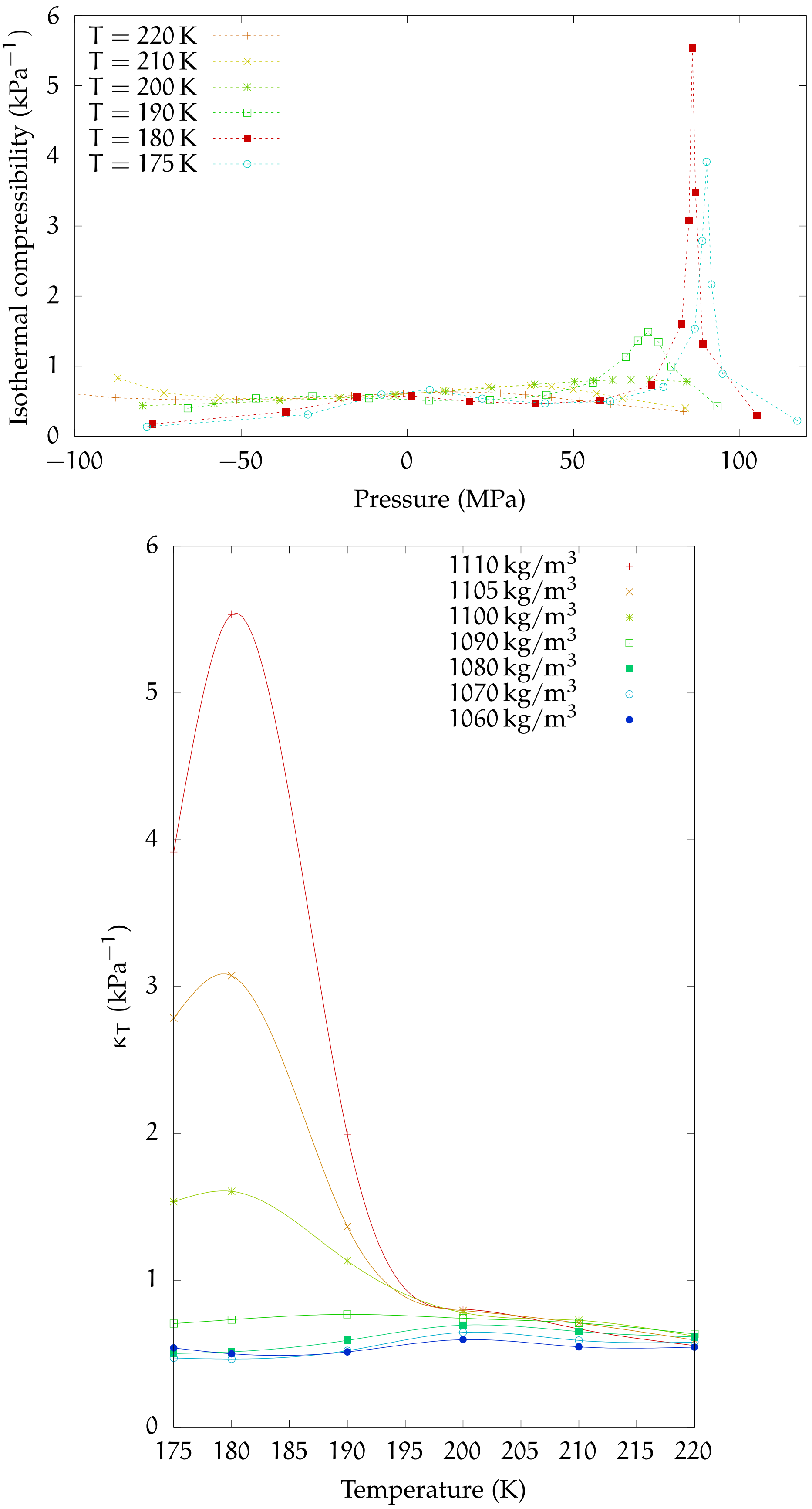

Figure 4.19: Isothermal compressibility for the $C_2^{NaClO_4}$ solution. Lines in the second figure are a fit of the results using natural smoothing splines.

Fig. 4.19 shows the isothermal compressibility across the isotherms and across the isochores, highlighting a peak in the same state point at

$$p_c = 85.7\,\text{MPa}.$$

From these results the estimated position of the LLCP was

$$\begin{cases} T_C = 180\,\text{K} \\ p_C = 85.7\,\text{MPa} \\ \rho_c = 1110\,\text{kg/m}^3 \end{cases}.$$

4.4 COMPARISON

To summarise the thermodynamic findings obtained in this chapter, Table 4.7 provides the critical points identified in both the C_1 and C_2 $NaClO_4$ solutions, compared with the bulk phase data.

A slight increase in the Liquid-Liquid Critical Point (LLCP) temperature is observed relative to the bulk for the $C_2^{NaClO_4}$ solution, while the critical pressure decreases slightly for the $C_1^{NaClO_4}$ solution and of circa 85 MPa at concentration $C_2^{NaClO_4}$.

For an immediate comparison of these thermodynamic findings, Fig. 4.20 displays the phase diagram for both solutions in the (p, T) plane. This includes the maxima of the isothermal compressibility (serving as an indicator of the Widom line), the liquid-gas Limit of Mechanical Stability (LG-LMS) curves, as well as the Temperature of Maximum Density (TMD) and Temperature of Minimum Density (TmD) curves. Fig. 4.20 also shows the LLCP as reported in Table 4.7

The TMD exhibits a significant displacement in both temperature and pressure compared to the bulk at the highest concentration examined. This shift appears less pronounced in the TmD. The LG-LMS lines, however, remain largely unchanged in position.

Results can then be schematised by considering the phase diagram cartoons presented in Fig. 4.21, in which hypothesised positions of the HDL-LDL

---

[3] Debenedetti et al., 2020.

SYSTEM	T_C	p_C	ρ_C
bulk[3]	172 K	186 MPa	1030 kg/m^3
$C_1^{NaClO_4}$	173 K	169 MPa	1050 kg/m^3
$C_2^{NaClO_4}$	180 K	85.7 MPa	1110 kg/m^3

Table 4.7: Overview of the critical points of the $C_1^{NaClO_4}$ and the $C_2^{NaClO_4}$: T_C shifts to slightly higher temperatures, p_C to lower pressures, ρ_C to higher densities.

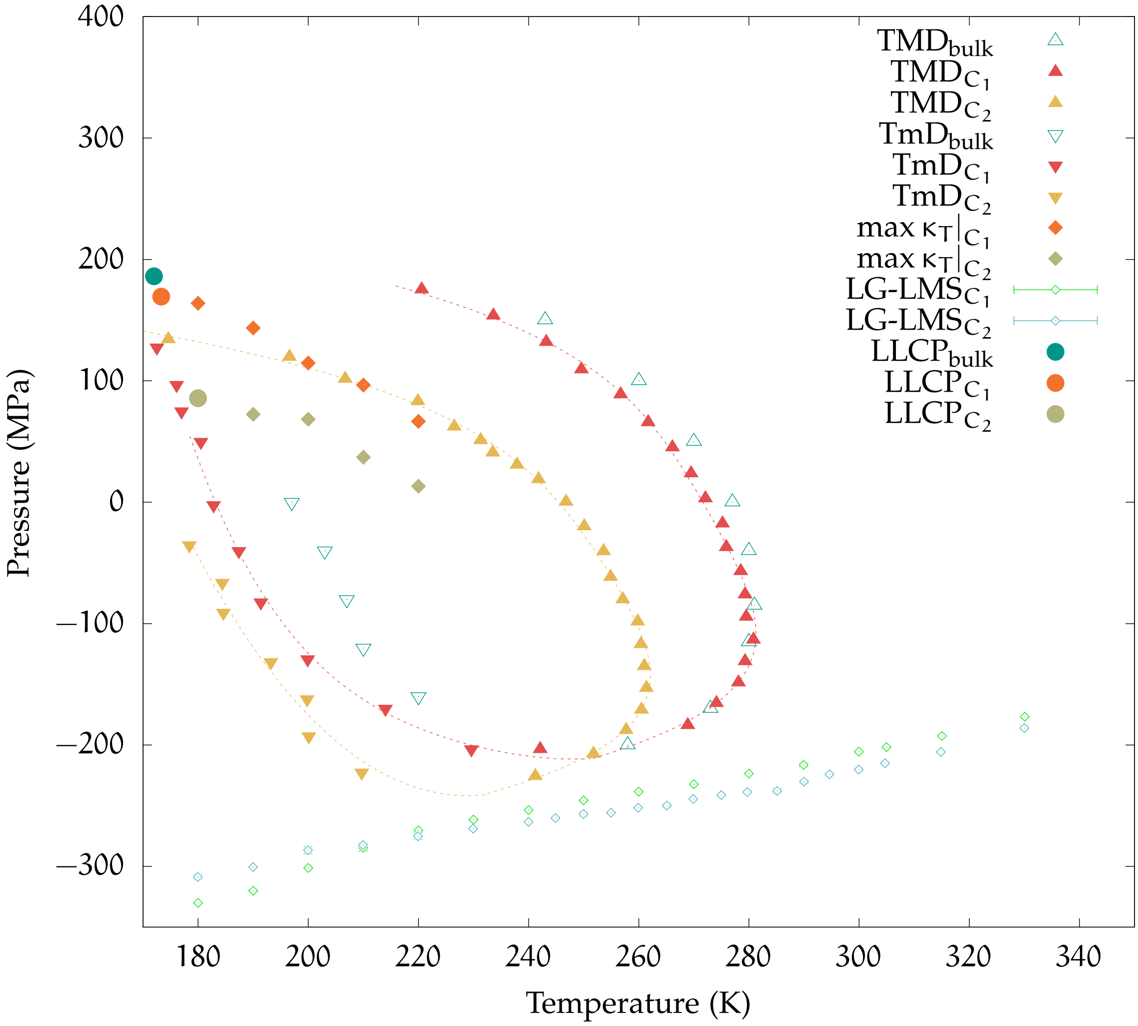

Figure 4.20: Thermodynamic features of the C_1 and C_2 aqueous $NaClO_4$ solutions. The LLCPs, the TMD and TmD curves are plotted and compared to the bulk. The figure also shows the Widom Line and the LG-LMS for the two solutions considered.

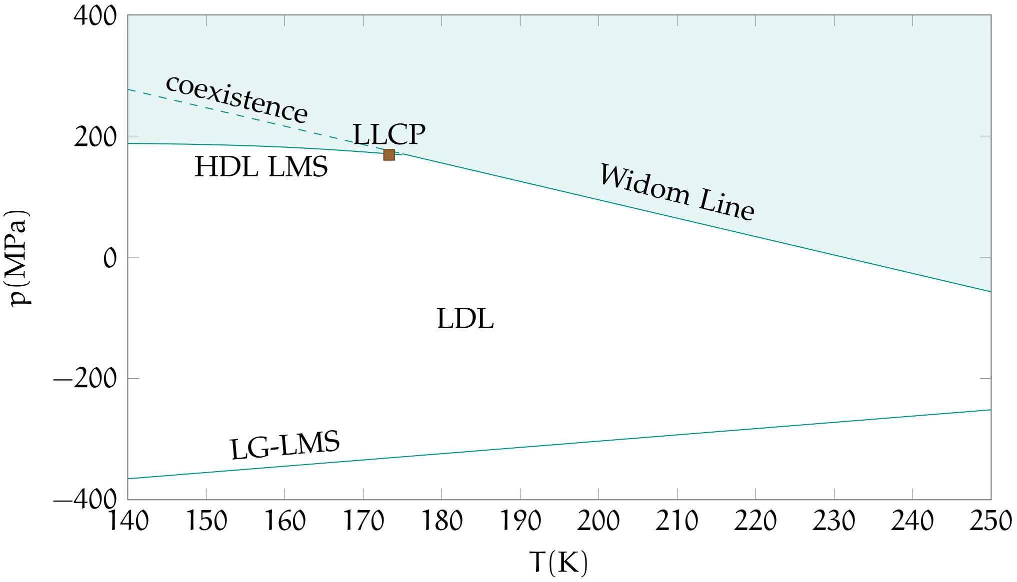

(a) $C_1 = 1.63\,\mathrm{wt\%}$

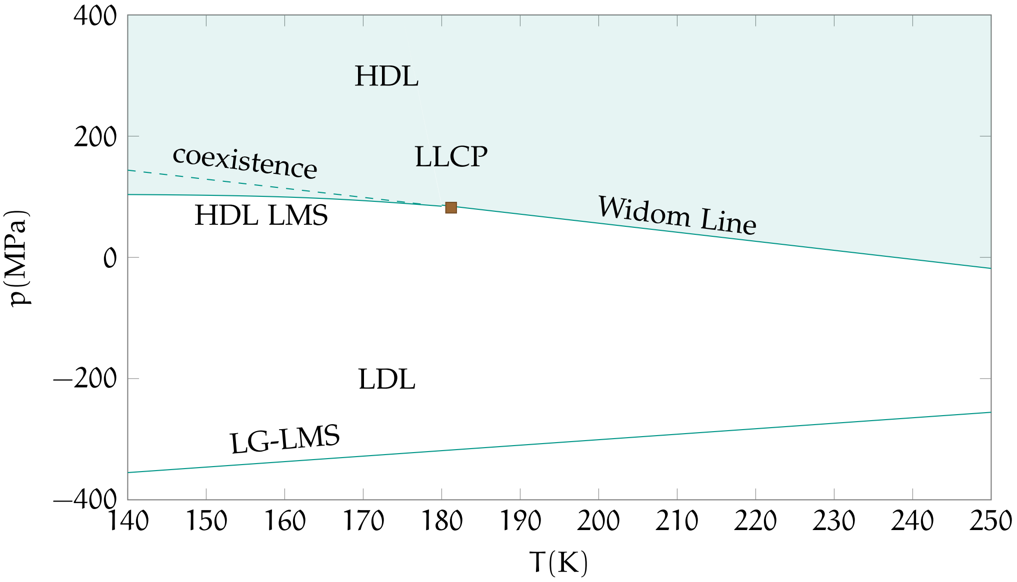

(b) $C_2 = 15.4\,\mathrm{wt\%}$

Figure 4.21: Schematic phase diagrams of the ${C_1}^{\mathrm{NaClO_4}}$ and the ${C_2}^{\mathrm{NaClO_4}}$ solutions, clearly showing the LDL region shrinking upon increasing the sodium perchlorate concentration. The positions of the HDL-LDL coexistence line and the HDL LMS here shown are hypothesised, as equilibration to eccessively low temperature is not possible in MD simulations (see Sec. 3.3.3).

coexistence line and the HDL LMS are also shown, as their exact location is not easy to calculate in MD due to difficulties in equilibrating too low supercooled temperatures.

It is worth mentioning that for $T > T_C$, the Widom line separates the phase diagram into regions resembling more HDL-like or LDL-like characteristics. At $T < T_C$, the coexistence line delineates the separation between the LDL and HDL phases. The observed shrinkage of the LDL region upon increasing the solute concentration implies that ions are more likely to be solvated in denser water, thereby tending to stabilise the HDL region over the LDL region.

The HDL region appears to expand at the expense of the LDL region

FINAL REMARKS By examining the trends of the Widom Line, of the TMD and the TmD curves and by noting the almost constant position of the LG-LMS, a contraction in the LDL region is evident.
This contraction might explain why water is found in a liquid form on Mars (Orosei et al., 2018; Lauro et al., 2021), nucleation being favoured in the LDL region. Indeed, local structural ordering not only controls water anomalies but also ice nucleation (Gallo et al., 2016).

5

STRUCTURAL RESULTS: $NaClO_4$ SOLUTIONS

5.1 THE RADIAL DISTRIBUTION FUNCTION

THE STRUCTURAL properties of an isotropic fluid can be analysed by means of the pair correlation function $g(r)$ (Gallo and Rovere, 2021; Allen and Tildesley, 2017) which, between particles of type A and B, can be operatively defined as (Abraham et al., 2023)

$$g_{AB}(r) = \frac{V}{N^2}\left\langle \sum_{i=0}^{N_A}\sum_{j=0}^{N_B} \delta(r - r_{ij}) \right\rangle \tag{5.1}$$

which only depends on r and quantifies the likelihood of finding a pair of atoms or molecules at a distance r.

For this reason, $g(r)$ is known as *radial distribution function*.

In computer simulations $\delta(r - r_{ij})$ in eq. (5.1) is replaced by a function of compact support that holds non-zero values within a narrow interval. The `gmx rdf` tool allows to perform this calculation in GROMACS and was used to provide the results which are going to be discussed in this chapter and that are also published in La Francesca and Gallo, 2023.

5.2 WATER-WATER RADIAL DISTRIBUTION FUNCTIONS

In this section the differences in the structural behaviour of water as it transitions from the HDL to the LDL phase will be investigated by means of the $O_W - O_W$ RDF, whose behaviour between bulk water, the C_1 and C_2 aqueous $NaClO_4$ solutions will be compared in detail.

Picking a reference convention for comparison at different concentrations was not straightforward, as the $NaClO_4$ isochores at the two concentrations have very different curvatures and are shifted in pressure. It was therefore chosen to compare the two systems at densities such that the thermodynamic behaviour of their respective isochores was similar at low temperatures.

This led to the choice of three sets of densities for the two $NaClO_4$ solutions and bulk:[1]

HIGH-DENSITY TRIPLET lying well above the LLCP;

$$\begin{cases} \rho_0 = 1110\,\mathrm{kg/m^3} \\ \rho_{C_1} = 1110\,\mathrm{kg/m^3} \\ \rho_{C_2} = 1200\,\mathrm{kg/m^3} \end{cases}$$

---

[1] The density of the solution with concentration C_x is denoted by ρ_{C_x}, while ρ_0 is used for the bulk.

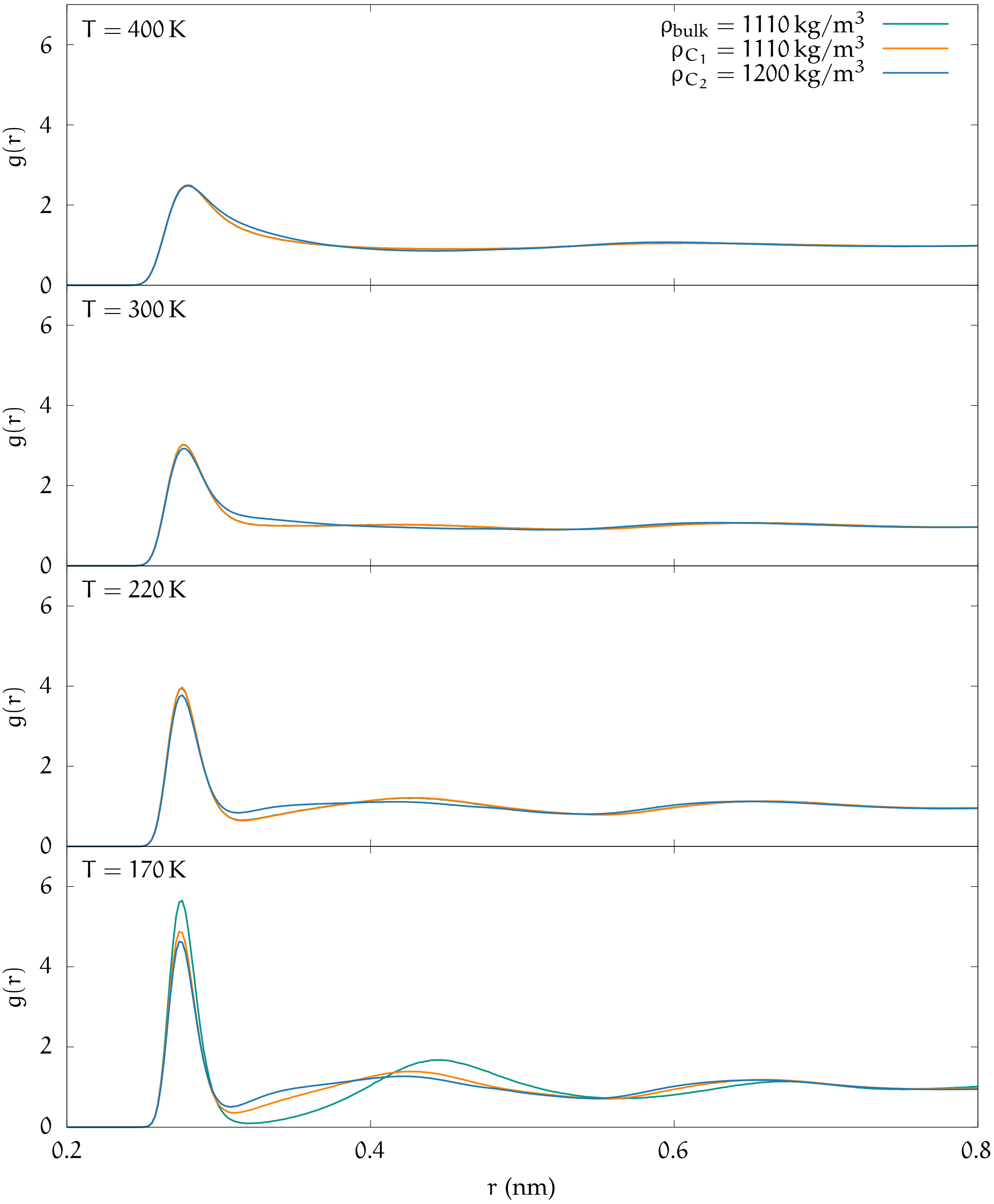

Figure 5.1: Water-Water RDF for the high-density set for the bulk and the $NaClO_4$ solutions. At the lowest temperature investigated the bulk is clearly in the LDL phase.

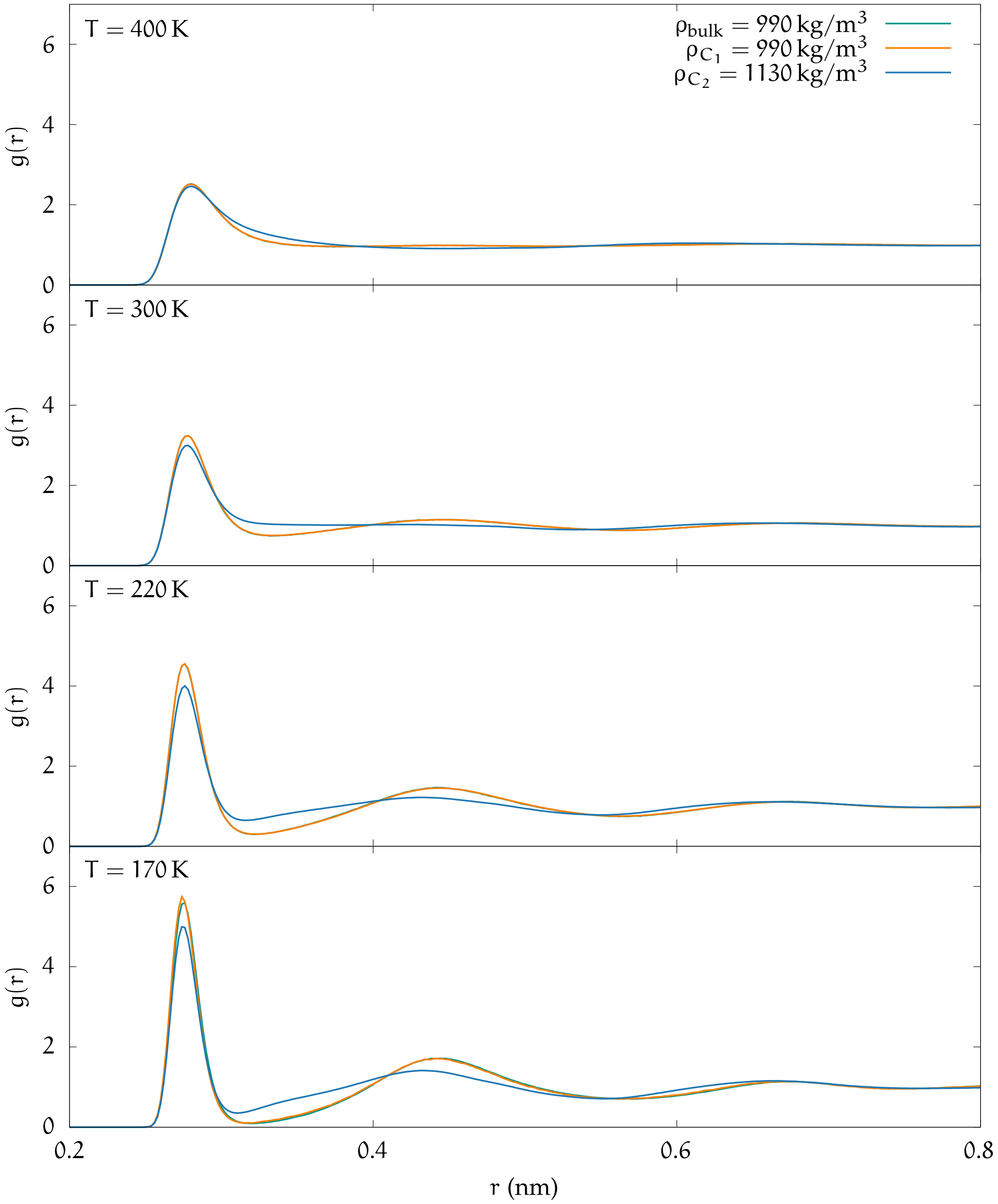

Figure 5.2: Water-Water RDF for the medium-density set for the bulk and the $NaClO_4$ solutions. The bulk and the $C_1^{NaClO_4}$ solution are practically indistinguishable and they appear to be in the LDL phase at low temperatures. Even though the thermodynamic behaviours of the three systems are similar, structurally the $C_2^{NaClO_4}$ solution appears to behave like the higher densities in Fig. 5.1 due to its state points being above the Widom Line.

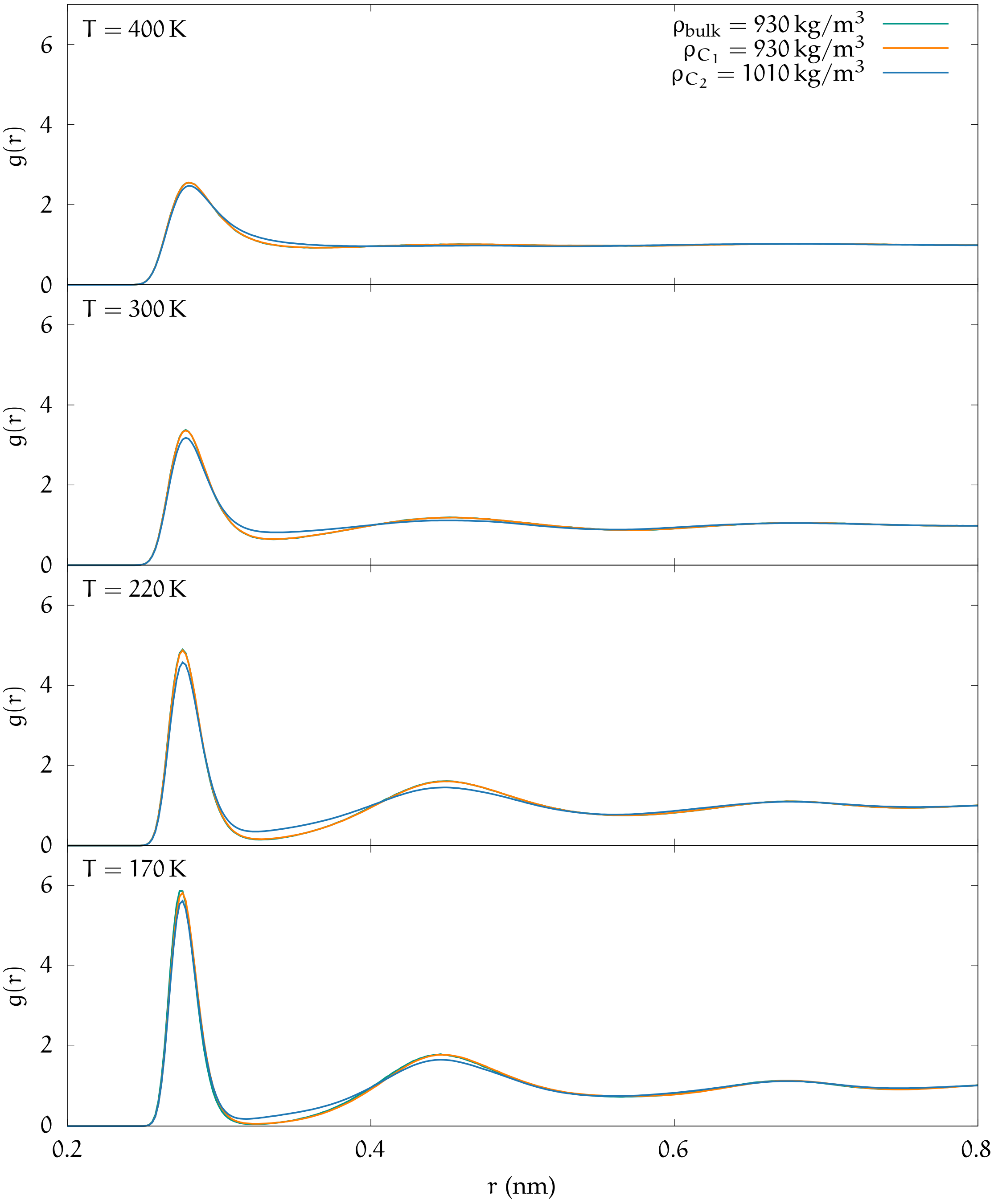

Figure 5.3: Water-Water RDF for the low-density set for the bulk and the $NaClO_4$ solutions. All the systems considered appear to be in the LDL phase at low temperature. The $C_1^{NaClO_4}$ solution closely matches the bulk, as in Fig. 5.2.

MEDIUM-DENSITY TRIPLET lying in an intermediate region between the HDL and the LDL phase;

$$\begin{cases} \rho_0 = 990\,\mathrm{kg/m^3} \\ \rho_{C_1} = 990\,\mathrm{kg/m^3} \\ \rho_{C_2} = 1130\,\mathrm{kg/m^3} \end{cases}$$

LOW-DENSITY TRIPLET lying in the LDL region.

$$\begin{cases} \rho_0 = 930\,\mathrm{kg/m^3} \\ \rho_{C_1} = 930\,\mathrm{kg/m^3} \\ \rho_{C_2} = 1010\,\mathrm{kg/m^3} \end{cases}$$

As discussed in Sec. 2.7.2, upon shifting from an LDL-like to an HDL-like phase, a collapse of the second shell of the $g_{O-O}(r)$ RDF occurs, indicating a disruption of the hydrogen bonds between the first and second shells of water molecules.

Hence, to distinguish between the HDL and LDL phases of water, the first minimum and the second maximum can be considered: a pronounced first minimum followed by a sharp local maximum indicates the LDL phase, while a gentler first minimum and a less pronounced second maximum are indicative of the HDL phase (Corradini et al., 2011; Gallo et al., 2011; Soper, 2017).

Figure 5.1 displays an analysis and comparison of the three systems at the directly comparable high densities:

$$\rho_0 = 1110\,\mathrm{kg/m^3}, \rho_{C_1} = 1110\,\mathrm{kg/m^3}, \rho_{C_2} = 1200\,\mathrm{kg/m^3}\,.$$

As expected from Fig. 4.21, at high temperatures, all the solutions considered display HDL behaviour, with the ${C_2}^{NaClO_4}$ system differing from the others at $T = 300\,\mathrm{K}$, indicating a more pronounced HDL nature.

The dissimilarity between the ${C_2}^{NaClO_4}$ solution and bulk water becomes increasingly pronounced with decreasing temperature. In contrast, the ${C_1}^{NaClO_4}$ solution exhibits significant deviations from the bulk only at the lowest examined temperature, $T = 170\,\mathrm{K}$. At this temperature, the water in the ${C_1}^{NaClO_4}$ solution presents a higher HDL character than bulk water. This deviation is much more pronounced in the ${C_2}^{NaClO_4}$ solution. As we will observe, aligning with the thermodynamic findings presented in the previous chapter, this represents the most notable distinction between the structure of the ${C_1}^{NaClO_4}$ solution and that of bulk water.

In Fig. 5.2, the intermediate density set

$$\rho_0 = 990\,\mathrm{kg/m^3}, \rho_{C_1} = 990\,\mathrm{kg/m^3}, \rho_{C_2} = 1130\,\mathrm{kg/m^3}$$

is examined. Here, the ${C_1}^{NaClO_4}$ solution closely matches the bulk also at the lowest temperature while the behaviour of the ${C_2}^{NaClO_4}$ solution resembles that at higher densities, aligning with the observed reduction in the LDL region upon increasing the concentration of the solutes.

Lastly (Fig. 5.3), the lowest densities comparable

$$\rho_0 = 930\,\mathrm{kg/m^3}, \rho_{C_1} = 930\,\mathrm{kg/m^3}, \rho_{C_2} = 1010\,\mathrm{kg/m^3}$$

are considered. At low temperatures, all systems are in the LDL phase, although the ${C_2}^{NaClO_4}$ solution shows distinct differences compared to the other two systems, being less LDL.

The structural observations, therefore, perfectly match what was observed from thermodynamics: firstly, while increasing the ion concentration, water retains its anomalous character, evidenced by its dichotomous structural behaviour; secondly, there is a shrinkage of the LDL region.

5.2.1 *Coordination Number*

To conclude the structural analysis of the water-water RDF, the behaviour of the oxygen-oxygen first shell coordination numbers for water is analysed:

$$N_{\mathrm{coord}} = 4\pi\,\rho_{O_W} \int_0^{r_0} dr\, g_{O_W - O_W}(r)\, r^2\,, \tag{5.2}$$

where

- ρ_{O_W} is the density of water oxygens;
- $g_{O_W - O_W}(r)$ is the water-water RDF;
- the cutoff distance r_0 is the first point of minimum of $g_{O_w - O_W}(r)$.

In the current context, the (5.2) can be rewritten as a function of ρ

$$N_{\mathrm{coord}} = 4\pi\,\frac{N_{O_W}}{m_{TOT}}\,\rho \int_0^{r_0} dr\, g_{O_w - O_W}(r)\, r^2\,. \tag{5.3}$$

Figure 5.4 depicts the $O_W - O_W$ first-shell coordination numbers evaluated at selected temperatures as a function of varying densities. Since, for each concentration, the cutoff distance r_0 (corresponding to the first RDF minimum) remained almost unchanged at low temperatures, it was opted to adopt the same value for all densities: $r_0 = 0.335\,\mathrm{nm}$ for the ${C_1}^{NaClO_4}$ solution and $r_0 = 0.328\,\mathrm{nm}$ for the ${C_2}^{NaClO_4}$ solution.

Upon increasing the densities, the coordination numbers for both concentration show an increasing trend with similar slopes. As the concentration increases, the curves shift downwards since water molecules also need to solvate the ions of the solutions.

At lower temperatures, the coordination number approaches 4, thus confirming the presence of LDL water in both solutions.

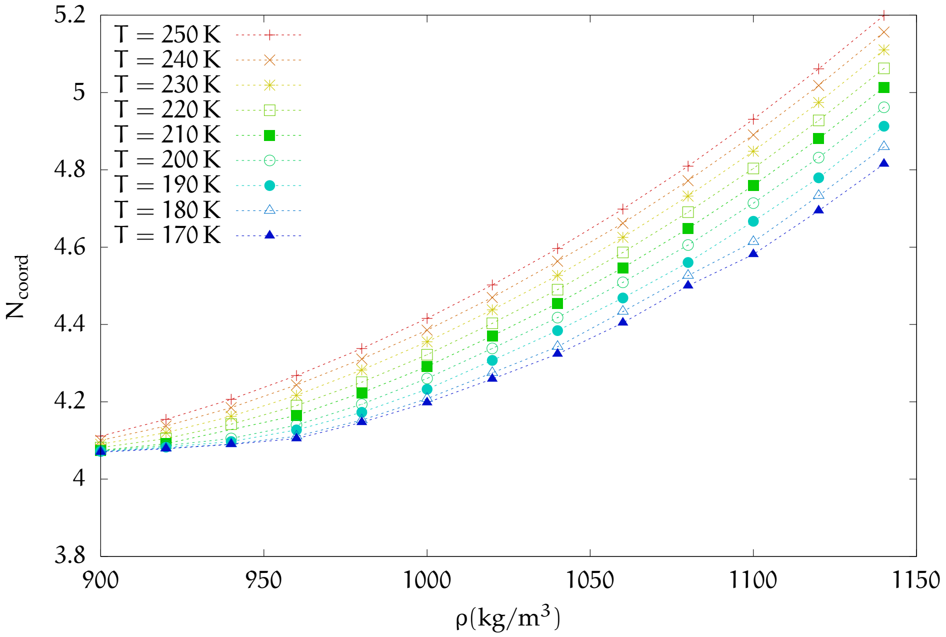

(a) $C_1^{NaClO_4} = 1.63$ wt%

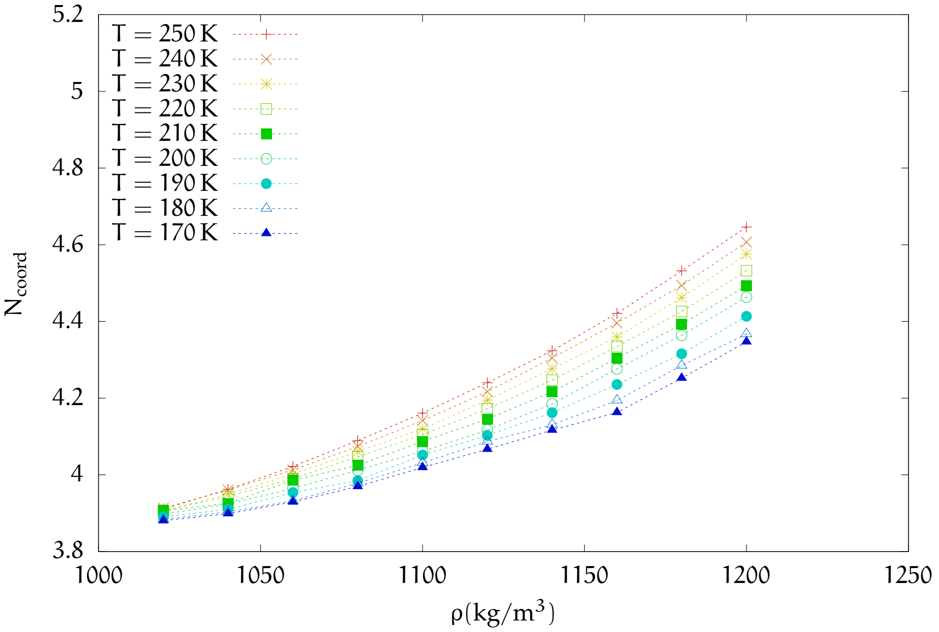

(b) $C_2^{NaClO_4} = 15.4$ wt%

Figure 5.4: $O_W - O_W$ first shell coordination numbers for selected temperatures as a function of density for the C_1 and the C_2 $NaClO_4$ solutions.

5.3 ION-WATER AND ION-ION RADIAL DISTRIBUTION FUNCTIONS

Figure 5.5 and Fig. 5.6 depict the alternating arrangement of ions within the $C_2^{NaClO_4}$ solution by means of the $Cl-H$, $Cl-Na$, $Cl-O_W$ and $Cl-Cl$ RDFs at densities $\rho_{C_2^{NaClO_4}} = 1200\,kg/m^3$ (Fig. 5.5) and $\rho_{C_2^{NaClO_4}} = 1010\,kg/m^3$ (Fig. 5.6). The results were comparable across the two concentrations but only the highest concentration, being more representative, will be considered.

The observations indicate that the chlorine ion is consistently surrounded by a cage of water molecules. This is apparent from the fact that the first peak, which remains largely consistent across all temperatures, occurring in the RDF corresponds to the hydrogen. Sodium, oxygen and chlorine follow in sequence.

At high temperatures, the RDF behaves nearly identically for the two densities.

The behaviour of the peak associated with the sodium ion suggests that the ion pairing (Cl-Na) is more prominent at lower densities. This trend can be attributed to the exclusion of ions by water in the LDL phase, leading to a higher likelihood of ion proximity, similarly to what can be seen for example in Corradini et al., 2011 for NaCl. This phenomenon becomes more pronounced at lower temperatures, as water increasingly assumes LDL-like behaviour.

Focusing on the Cl-Cl interaction, it is found that for $\rho = 1200\,kg/m^3$ (figure 5.5), the first coordination shell is located further away compared to other ions and shifts slightly closer as temperature decreases, albeit with only a mild increase in peak intensity. For the lower density $\rho = 1010\,kg/m^3$ (figure 5.6), at higher temperatures, the first coordination shell behaves similarly to the higher density case. However, as the temperature lowers and the proportion of LDL water rises, the Cl first coordination shell not only gets closer, as in the higher density case, but also exhibits a significantly enhanced peak intensity. At the lowest temperature studied, oscillations in the peaks are noted, indicating the onset of ordering among the Cl ions. It is emphasised that the two lowest temperatures on this isochore are the only state points below the Widom line among these eight graphs, indicating that as water in the solution becomes more LDL-like (below the Widom line), chlorine ions find it easier to order. This confirms that LDL water does not favour ion solvation, which appears to be preferred in the HDL phase (see also Corradini et al., 2010, 2012).

These findings align with the observed reduction of the LDL thermodynamic region, as discussed in the previous chapter (see Fig. 4.21).

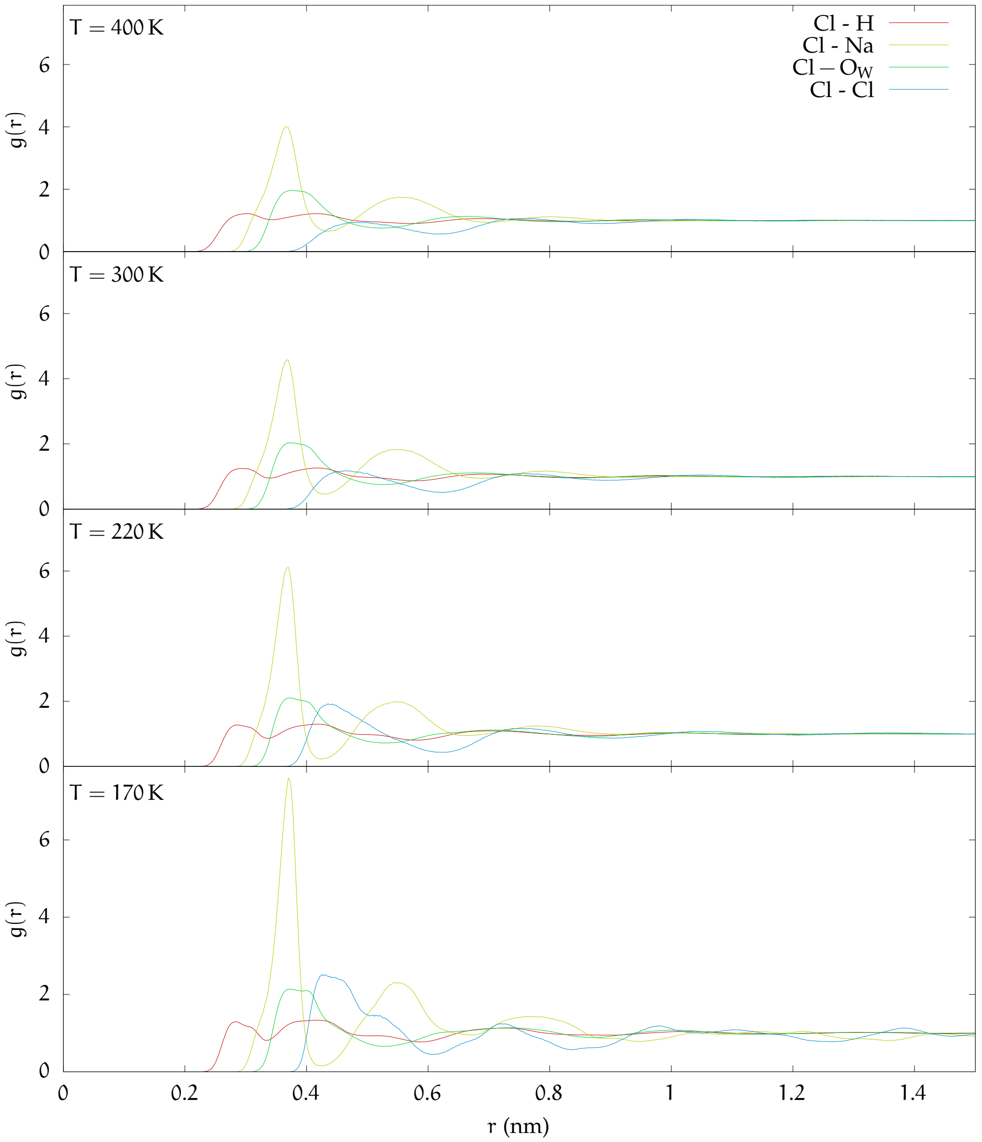

Figure 5.5: Radial distribution functions for $Cl-H$, $Cl-Na$, $Cl-O_W$ and $Cl-Cl$ in the $C_2{}^{NaClO_4}$ solution at $\rho = 1200\,kg/m^3$.

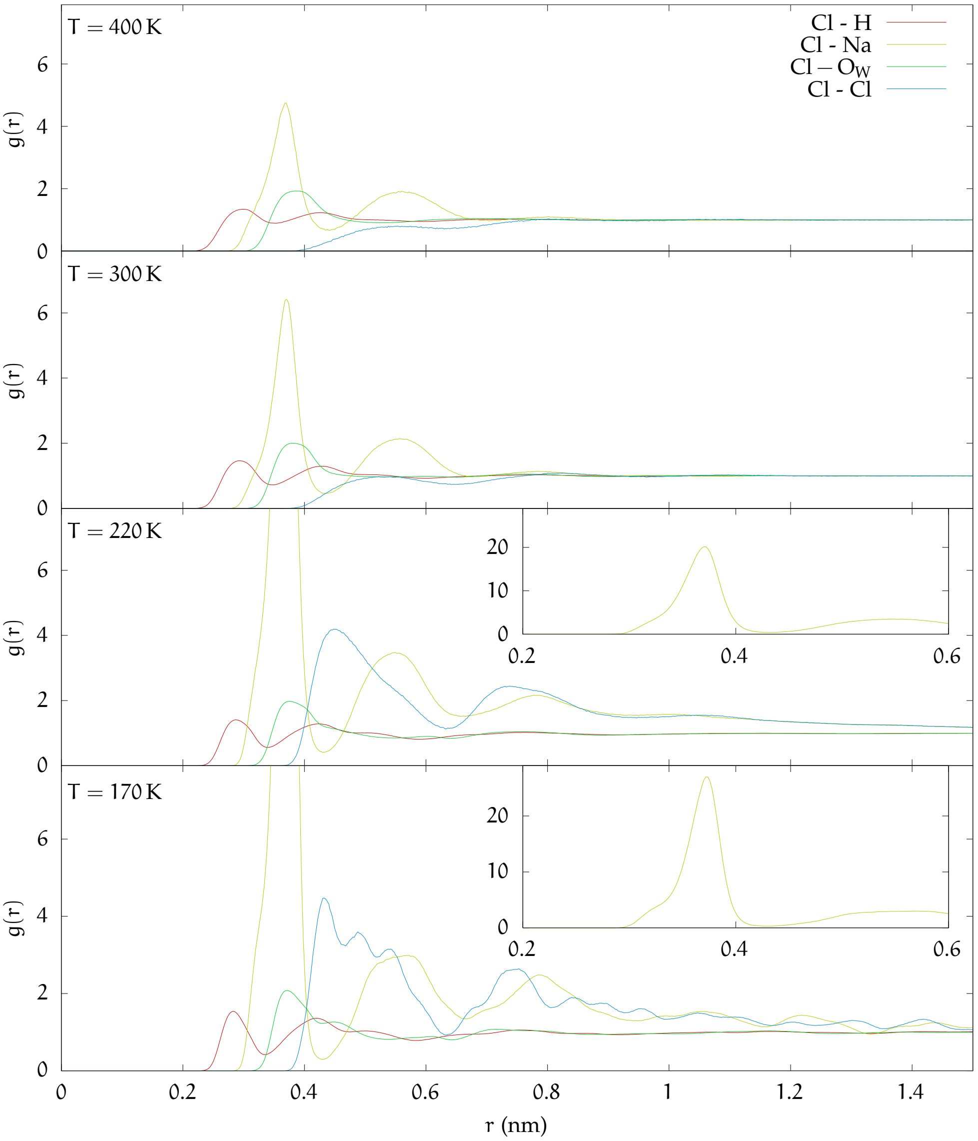

Figure 5.6: Radial distribution functions for $Cl-H$, $Cl-Na$, $Cl-O_W$ and $Cl-Cl$ in the $C_2^{NaClO_4}$ solution at density $\rho = 1010\,kg/m^3$. The lower right panels display the Cl–Na RDF separately, using different scales to emphasise the height of the first peak.

Part III

MAGNESIUM PERCHLORATE IN AQUEOUS SOLUTIONS

6

THERMODYNAMICS OF $Mg(ClO_4)_2$ AQUEOUS SOLUTIONS

During the third year of the doctoral programme, MD simulations were conducted on aqueous solutions of magnesium perchlorate. Magnesium, sodium, calcium and potassium perchlorates are abundantly present on Mars and, as described in Chapter 2, are believed to be the key to the detection of liquid water underneath the Martian soil (Orosei et al., 2018; Lauro et al., 2021).

Experiments (Toner et al., 2014) have shown that whilst sodium perchlorate solutions can be supercooled down to approximately 220 K, solutes such as magnesium or calcium perchlorate can reduce this temperature to at least 150 K. This is significant for two primary reasons: firstly, magnesium and calcium perchlorates are believed to be more prevalent than sodium perchlorate on Mars; secondly, the temperature of Martian liquid solutions on the site of observation was estimated to be approximately 180 K.

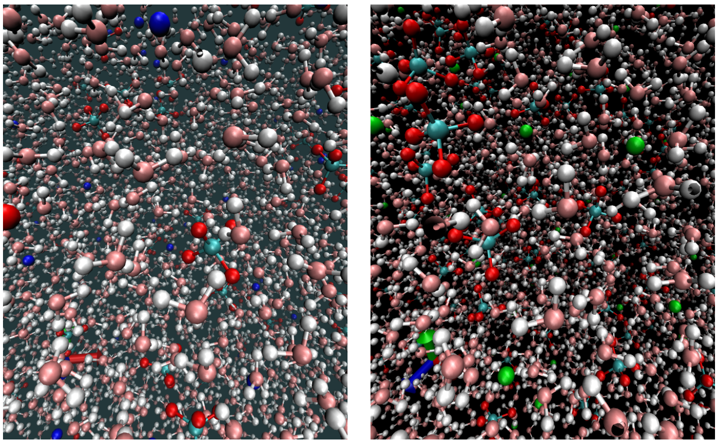

Figure 6.1: Partial snapshots of a 15.4 wt% $NaClO_4$ and of a 24.4 wt% $Mg(ClO_4)_2$ aqueous solutions at $\rho = 1200\,kg/m^3$ and $T = 200\,K$.

Consequently, it was decided to calculate the phase diagram and analyse the structure of aqueous solutions of magnesium perchlorate.

To understand the effects of the ions on the thermodynamics and the structure of the system, as already done and discussed in Chapters 4 and 5 for sodium perchlorate, phase diagrams and radial distribution functions of aqueous solutions of magnesium perchlorate were examined at two different concentrations:

$$C_1^{Mg(ClO_4)_2} = 2.95\,wt\% \qquad C_2^{Mg(ClO_4)_2} = 24.4\,wt\%.$$

The concentration details for all the systems studied during the PhD programme are presented in Table 6.1. The number of ions and water molecules were selected to achieve comparable number fractions between the sodium and the magnesium perchlorate aqueous solutions.

Partial snapshots of the $C_2^{NaClO_4}$ and of the $C_2^{Mg(ClO_4)_2}$ aqueous solutions at $\rho = 1200\,kg/m^3$ and $T = 200\,K$ are reported in Fig. 6.1.

Water was modelled using the TIP4P/2005 potential, due to its capability to yield reliable results in phase diagram analysis.

SOLUTE	CONCENTRATION				
		N_{ions}	$N_{\text{water molecules}}$	wt%	numb. frac.$\times 10^{-3}$
$NaClO_4$	$C_1^{NaClO_4}$	20	4099	1.63	2.43
	$C_2^{NaClO_4}$	200	3737	15.4	26.1

SOLUTE	CONCENTRATION				
		N_{ions}	$N_{\text{water molecules}}$	wt%	numb. frac.$\times 10^{-3}$
$Mg(ClO_4)_2$	$C_1^{Mg(ClO_4)_2}$	30	4072	2.95	2.45
	$C_2^{Mg(ClO_4)_2}$	300	3838	24.4	25.4

Table 6.1: Concentrations of the four systems investigated expressed both in weight percentage and in number fraction.

		MASS (a.m.u.)	q_i (e)	σ_{ii}(nm)	ϵ_{ii}(kJmol^{-1})
Mg^{2+}		24.3051	2	0.16	3.661
Na^+		22.9898	1	0.333045	0.011598
Cl	$Mg(ClO_4)_2$	35.4527	1.309	0.49	0.168
	$NaClO_4$		1.0786	0.347094	1.108760
O	$Mg(ClO_4)_2$	15.9994	-0.577	0.31	0.317
	$NaClO_4$		-0.51965	0.878640	0.011598

Table 6.2: Force field details for the solutions (Nieszporek et al., 2016; Agieienko et al., 2014).

Magnesium perchlorate was modelled using the potential defined in Agieienko et al., 2014. This potential retains the rigid tetrahedral configuration of the perchlorate ion induced by the sp^3 hybridisation and a formal charge of -1. The details of the parameters are described in Table 6.2. The Lorentz-Berthelot combination (4.1) rule completes the parameter space.

For the chosen potential parameters and the concentrations involved, the methodology applied to carry out the simulations uses GROMACS (Hess et al., 2008; Bekker et al., 1993; Berendsen et al., 1995) and it is identical to that reported in chapters 4 and 5 for sodium perchlorate.

The overall single-CPU simulation time for the two $NaClO_4$-TIP4P/2005 solutions and the two $Mg(ClO_4)_2$-TIP4P/2005 solutions was approximately 100 years. The equations of state were built out of a total number of 2937 state points.

The results that follow are planned to be submitted for publication in a paper currently under preparation (La Francesca and Gallo, 2024).

6.1 RESULTS FOR THE $C_1^{Mg(ClO_4)_2}$ = 2.95 wt% SOLUTION

In order to obtain the phase diagram of the $C_1^{Mg(ClO_4)_2}$ solution from ambient to supercooled conditions, isochores were simulated at the same densities as the $C_1^{NaClO_4}$ solution.

The 27 densities, along with the corresponding box lengths are reported in Table 6.3. By gradually lowering the density of the system, the LG-LMS, acknowledged by the emergence of cavitation, was reached over the 880 kg/m^3 isochore, exactly as previously occurred in the $C_1^{NaClO_4}$ solution.

Over the isochores, state points at temperatures ranging from 400 K to 170 K were simulated. The equilibration and production times needed to calculate them are reported in Table 6.4.

A snapshot of the solution at density 1100 kg/m^3 and temperature 200 K is shown in Fig. 6.2.

The simulated state points of the $C_1^{Mg(ClO_4)_2}$ solution are reported in the isochore (p, T) plane in Fig. 6.3. State points belonging to the same isochore are depicted in identical colours, while dashed curves serve as visual guides. Isochores corresponding to the bulk TIP4P/2005 and the $C_1^{Mg(ClO_4)_2}$ solution at a density of 980 kg/m^3 are highlighted in black. A preliminary estimate of the region of density anomaly's location is provided by the curves of TMD and TmD, here recognised from the isochore minimum and maximum points as directly obtained from the simulations. These curve estimates are themselves depicted in Fig. 6.3 and compared with the bulk (Biddle et al., 2017). Also highlighted in the figure are the preliminary estimates of the points corresponding to the peaks of the isothermal compressibility for the solution here simulated, and the bulk LLCP as calculated in Debenedetti et al., 2020.

Following the approach used for the previous two solutions, more accurate estimates of the thermodynamic anomalies are immediately provided. This is done by fitting the isochores using sixth-degree polynomials and determining

DENSITY	BOX LENGTH
880 kg/m³	5.211 nm
890 kg/m³	5.192 nm
900 kg/m³	5.172 nm
910 kg/m³	5.153 nm
920 kg/m³	5.135 nm
930 kg/m³	5.116 nm
940 kg/m³	5.098 nm
950 kg/m³	5.080 nm
960 kg/m³	5.062 nm
970 kg/m³	5.045 nm
980 kg/m³	5.028 nm
990 kg/m³	5.011 nm
1000 kg/m³	4.994 nm
1010 kg/m³	4.977 nm
1020 kg/m³	4.961 nm
1030 kg/m³	4.945 nm
1040 kg/m³	4.929 nm
1050 kg/m³	4.913 nm
1060 kg/m³	4.898 nm
1070 kg/m³	4.882 nm
1080 kg/m³	4.867 nm
1090 kg/m³	4.852 nm
1100 kg/m³	4.838 nm
1110 kg/m³	4.823 nm
1120 kg/m³	4.809 nm
1130 kg/m³	4.794 nm
1140 kg/m³	4.780 nm

Table 6.3: Simulated densities for the $C_1^{Mg(ClO_4)_2}$ solution with the corresponding box lengths.

TEMPERATURE	EQUILIBRATION TIME	PRODUCTION TIME
400 K	0.1 ns	0.1 ns
380 K	0.1 ns	0.1 ns
350 K	0.1 ns	0.1 ns
330 K	0.1 ns	0.1 ns
315 K	0.1 ns	0.1 ns
305 K	0.1 ns	0.1 ns
300 K	0.1 ns	0.1 ns
295 K	0.1 ns	0.1 ns
290 K	0.1 ns	0.1 ns
285 K	0.1 ns	0.1 ns
280 K	0.5 ns	0.5 ns
275 K	0.5 ns	0.5 ns
270 K	0.5 ns	0.5 ns
265 K	0.5 ns	0.5 ns
260 K	1 ns	1 ns
255 K	1 ns	1 ns
250 K	1 ns	1 ns
245 K	1 ns	1 ns
240 K	10 ns	10 ns
230 K	10 ns	10 ns
220 K	20 ns	20 ns
210 K	20 ns	20 ns
200 K	40 ns	40 ns
190 K	40 ns	40 ns
180 K	40 ns	40 ns
175 K	40 ns	40 ns
170 K	40 ns	40 ns

Table 6.4: Simulation times for the $C_1^{Mg(ClO_4)_2}$ solution.

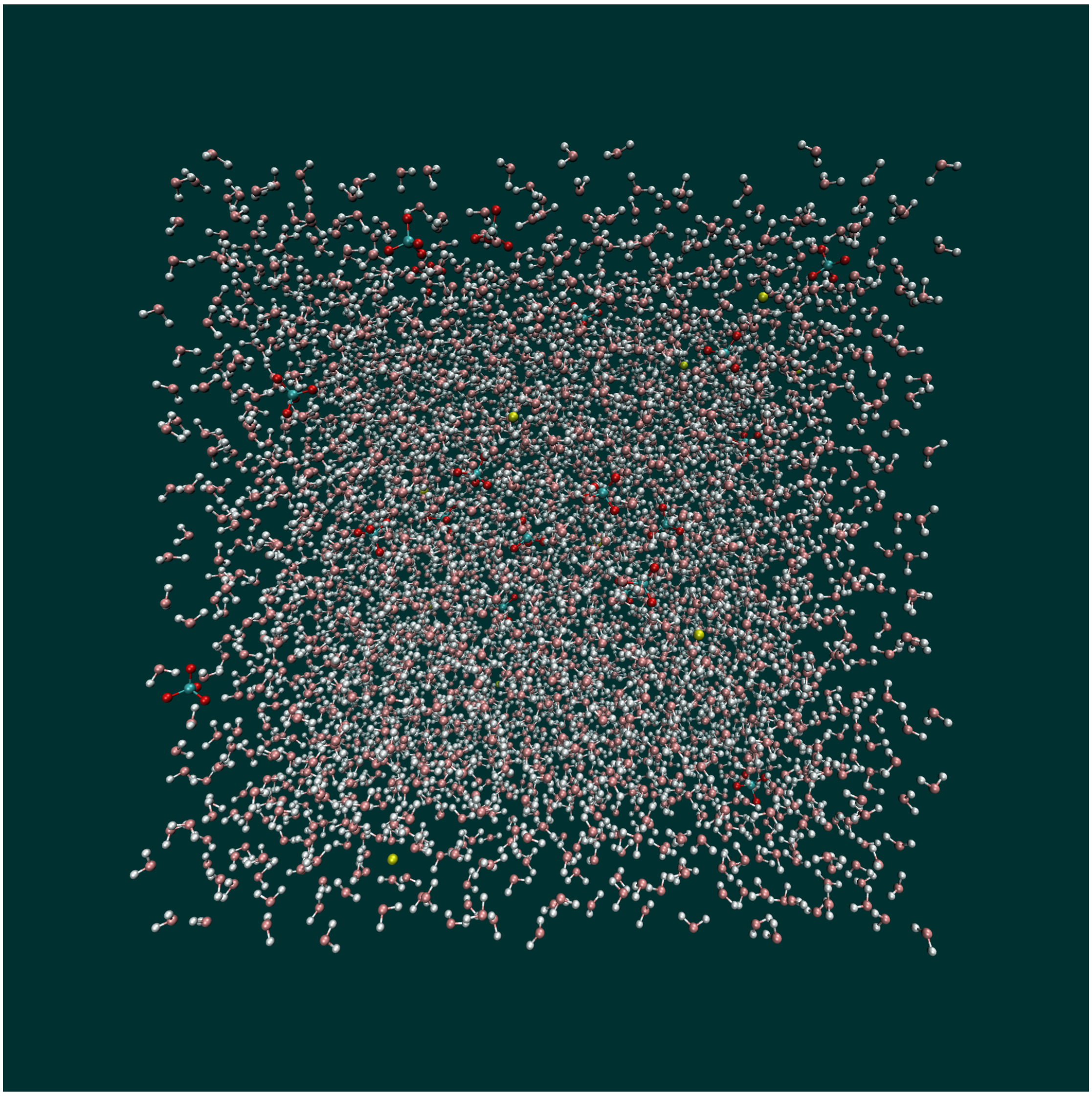

Figure 6.2: Snapshot of a $C_1^{Mg(ClO_4)_2} = 2.95\,\text{wt}\%$ solution at density $\rho = 1100\,\text{kg/m}^3$ and temperature $T = 200\,\text{K}$. Water is shown in pink (oxygen) and grey (hydrogens), magnesium in yellow and perchlorates in teal (chlorine) and red (oxygens).

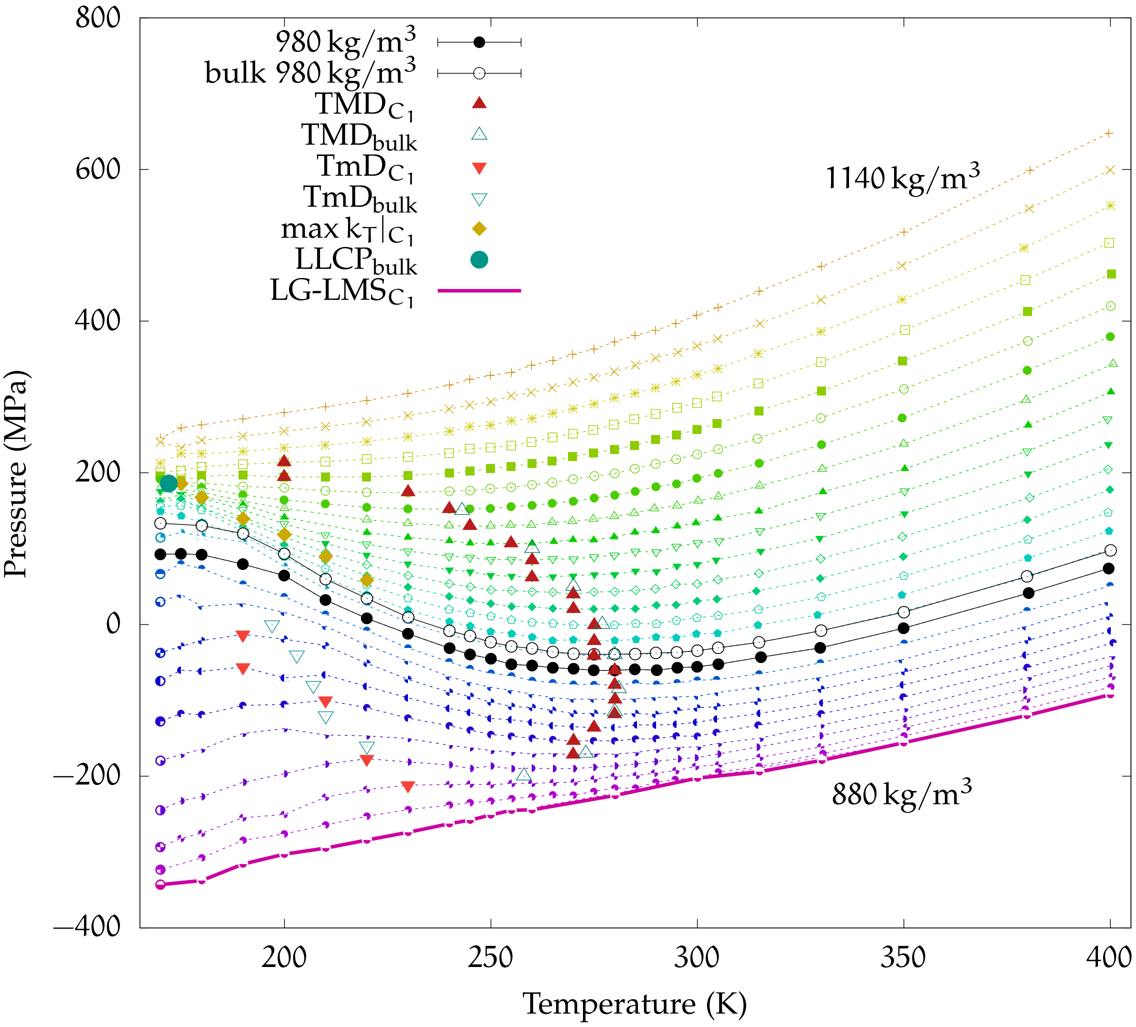

Figure 6.3: Unfitted simulated state points of the $C_1^{\mathrm{Mg(ClO_4)_2}}$ solution in the (p, T) plane, for densities ranging from $\rho = 880\,\mathrm{kg/m^3}$ to $\rho = 1140\,\mathrm{kg/m^3}$, with increments $\Delta\rho = 10\,\mathrm{kg/m^3}$ and temperatures from $T = 400\,\mathrm{K}$ to $T = 170\,\mathrm{K}$. The symbols represent state points derived from simulations, while the lines serve as a visual guide. Error bars are plotted but not visible. Included are initial estimates of the Temperature of Maximum Density (TMD) curves for the solution, shown as red-filled upward triangles, alongside bulk data (empty teal upward triangles) from Biddle et al., 2017. Downward triangles denote the TmDs. The teal-filled circle marks the bulk Liquid-Liquid Critical Point (LLCP) as per Debenedetti et al., 2020 and filled diamonds indicate the isothermal compressibility maxima obtained from the data. The thick dash-dotted line at the bottom represents the 880 kg/m^3 isochore, coinciding with the system's Liquid-Gas Limit of Mechanical Stability (LG-LMS). The 980 kg/m^3 isochore data for both the $C_1^{\mathrm{Mg(ClO_4)_2}}$ solution (filled black circles) and the bulk (empty black circles) is highlighted. Further refined estimates of the TMDs, TmDs and isothermal compressibility maxima will be provided subsequently.

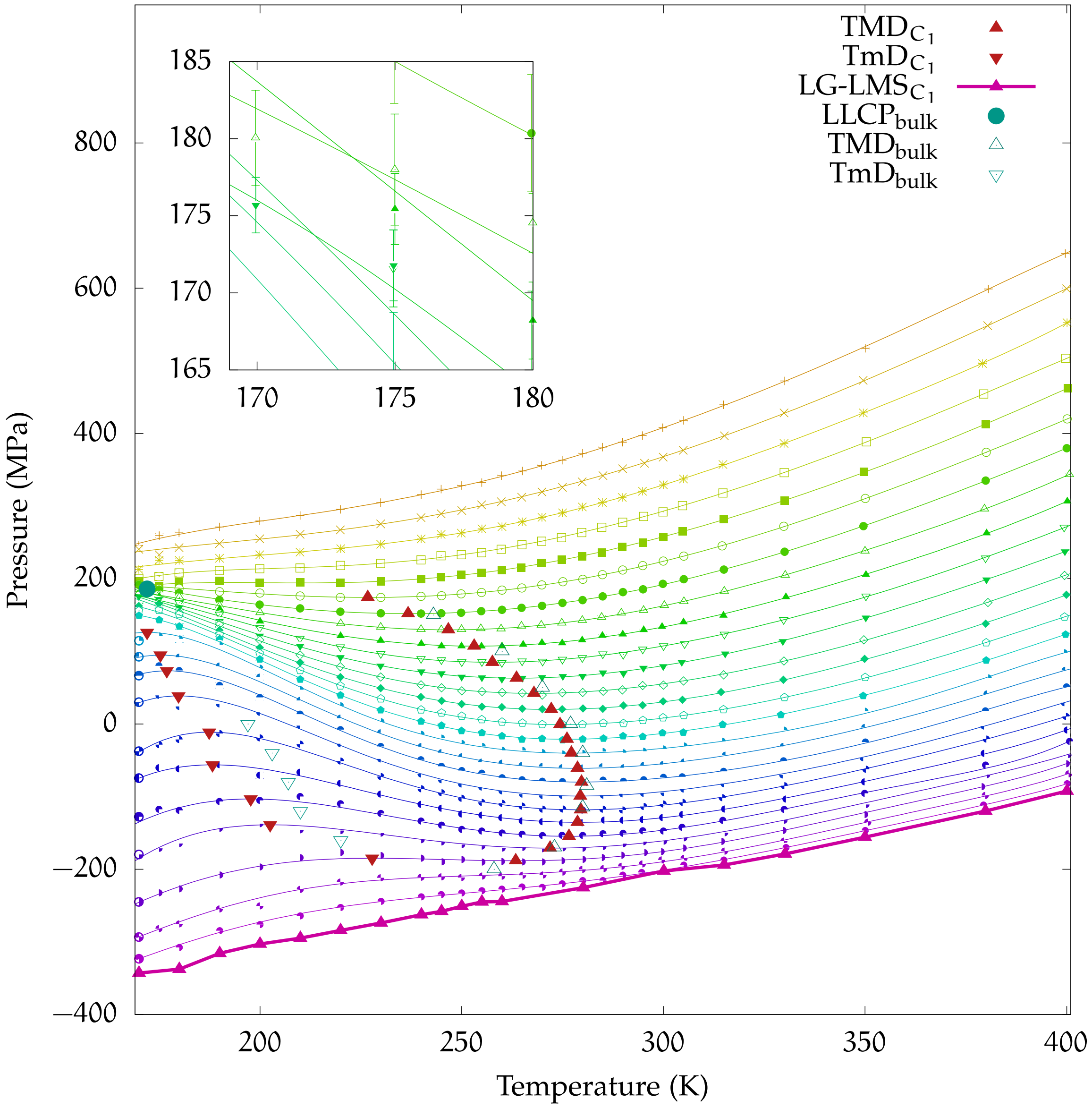

Figure 6.4: Equation of state in the isochore plane for the $C_1^{Mg(ClO_4)_2}$ solution obtained from MD simulations covering densities ranging from $\rho = 1140\,kg/m^3$ to $880\,kg/m^3$ (LG-LMS) with an incremental change of $\Delta\rho = 10\,kg/m^3$. Error bars are plotted but only visible in the inset. Polynomial fittings have been applied to the simulated data points and the resulting isochores are reported with solid lines. The teal-filled circle is the TIP4P/2005 bulk LLCP as computed in Debenedetti et al., 2020. The solution's TMDs (upward triangles) and the TmDs (downward triangles) obtained from the fits are highlighted in red and compared to the values known in literature for the bulk TIP4P/2005 (see Biddle et al., 2017) and here reported with teal empty triangles. Notably, the $1050\,kg/m^3$ and the $1060\,kg/m^3$, as well as the $1070\,kg/m^3$ and the $1080\,kg/m^3$ isochores cross approximately at 175 K.

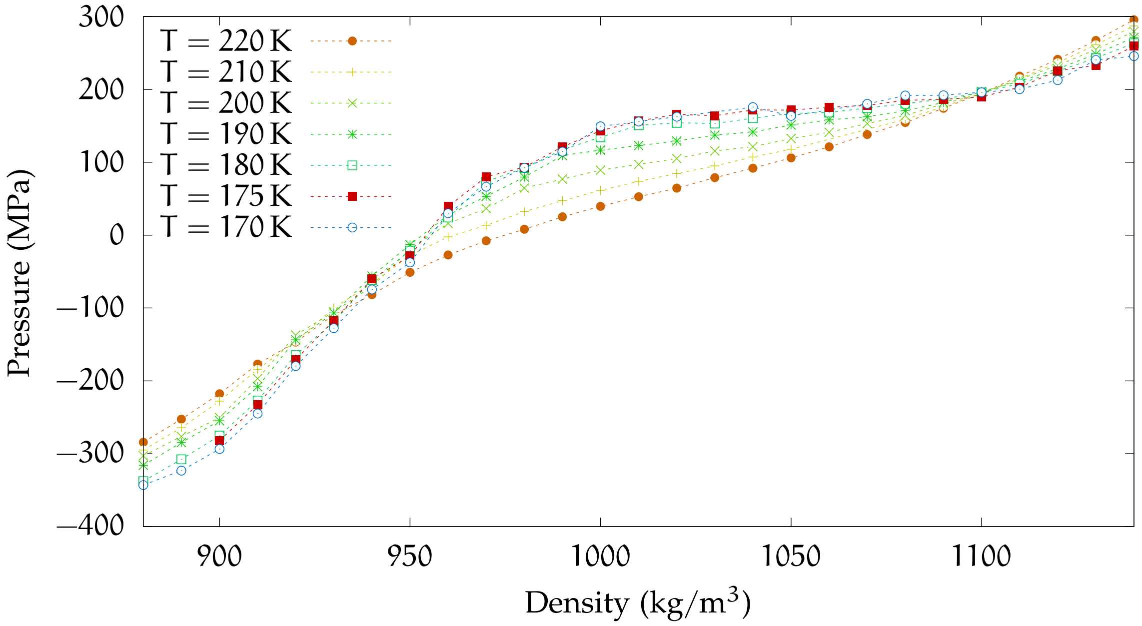

Figure 6.5: Simulated state points for the $C_1{}^{Mg(ClO_4)_2}$ solution plotted in the isotherm plane. The dashed lines are a guide for the eye. Highlighted in red are the points at 175 K, the closest temperature to where the crossings were identified in the isochore plane.

the resulting minima and maxima to respectively highlight the TMD and TmD curves: see Fig. 6.4. As for the $C_1{}^{NaClO_4}$ solution, a slight shift of the TMD curve towards lower temperatures is evident.

It is important to note that the isochores at densities 1050 kg/m^3 and 1060 kg/m^3, as well as those at densities 1070 kg/m^3 and 1080 kg/m^3 cross around 175 K. As per Eq. (4.10), an intersection in the isochore plane locates the critical region, which therefore will be also analysed in the isotherm plane.

Since the universality of critical phenomena is limited to the region close to the critical point, the analysis in the isotherm plane will be carried out for densities and temperatures close to where the isochores intersect.

The simulated state points in the isotherm planes are reported in Fig. 6.5 which also highlights by red squares the 175 K isotherm, since 175 K is the temperature around which the isochores cross.

Following the approach employed for the previous solutions, we proceed to fit the isotherms to fifth-degree polynomials in search of a horizontal point of inflexion to locate the critical point.

The equation of state of the system in the isotherm plane for the solution under consideration, complete with the $p_T(\rho)$ fits, is shown in Fig. 6.6. As expected, the curves flatten around 175 K. Interestingly, the pressure at the inflexion point for the last two isotherms is very similar.

Likewise, the derivative of the fits at those densities is located near the x-axis (Fig. 6.7), although actually slightly closer to zero at 175 K compared to 170 K.

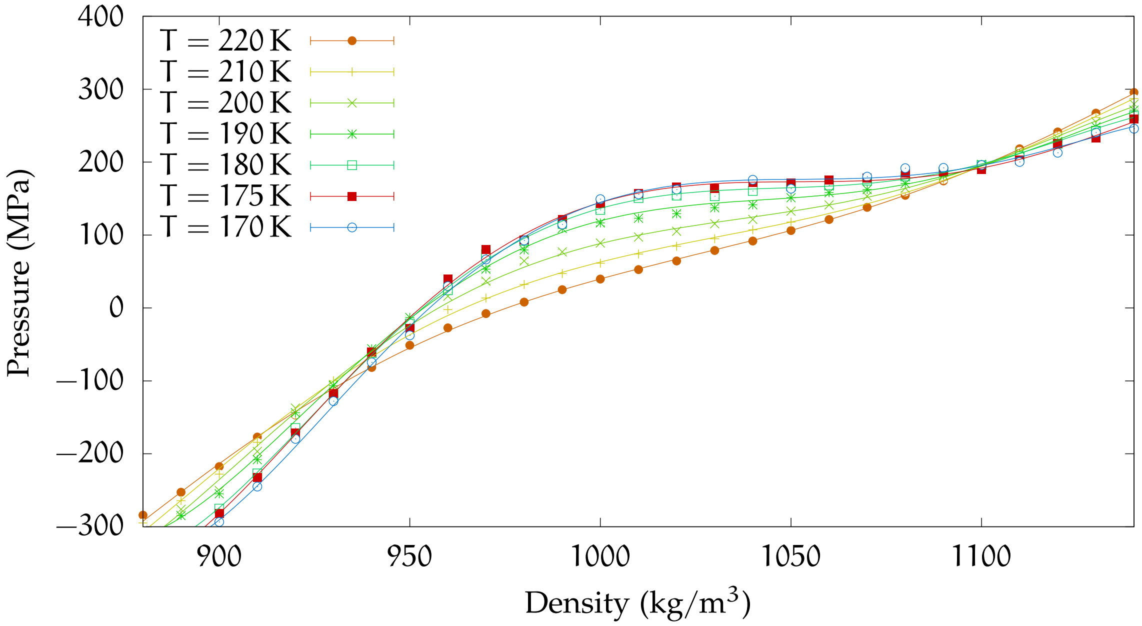

Figure 6.6: Equation of state in the isotherm plane for the $C_1{}^{Mg(ClO_4)_2}$ solution. Error bars are plotted but not visible. Lines are isotherm curves $p_T(\rho)$ obtained through polynomial fits to the simulated state points. Highlighted in red is the isotherm at 175 K, the closest temperature to where the crossing was identified in the isochore plane.

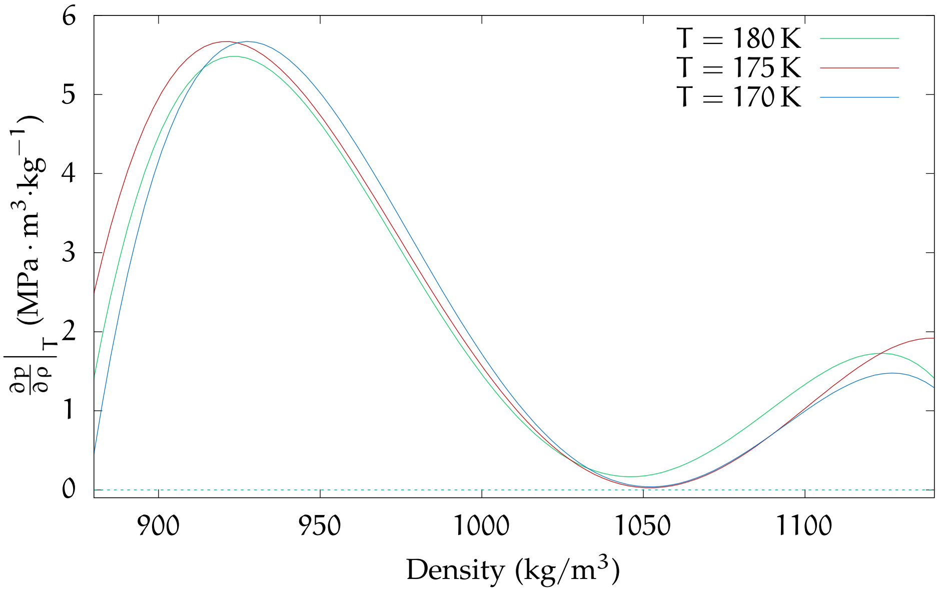

Figure 6.7: Derivative of $p_T(\rho)$ for the simulated temperatures closest to the critical point for the $C_1{}^{Mg(ClO_4)_2}$ solution.

To further understand the critical behaviour of the system, it is hence required to look at the peaks of the isothermal compressibility, which are shown in Fig. 6.8.

Despite both compressibility curves being very sharp at their peaks, it is clear that, being much higher, the one occurring over the 175 K curve offers the best estimate of the liquid-liquid critical temperature

$$T_C = 175\,\mathrm{K}\,.$$

Therefore, from the minimum of the critical isotherm's derivative (Fig. 6.7, in red), the critical density

$$\rho_C = 1052\,\mathrm{kg/m^3}$$

is estimated, and from the inflexion point of the critical isotherm (Fig. 6.6),

$$p_C = 173.1\,\mathrm{MPa}$$

the critical pressure.

As a result, the liquid-liquid critical point of the $C_1{}^{Mg(ClO_4)_2}$ solution

$$\begin{cases} T_C = 175\,\mathrm{K} \\ p_C = 173.1\,\mathrm{MPa} \\ \rho_C = 1052\,\mathrm{kg/m^3} \end{cases}$$

is obtained.

The resulting phase diagram, inclusive of the TMD and TmD curves (compared with the bulk), the peaks of isothermal compressibility, the LLCP (compared with the bulk), and the LG-LMS, is presented in Fig. 6.9. A slight shift of the critical point to a higher temperature and lower pressure is evident from the simulation, while the TMD and the TmD curves have shifted slightly downwards in temperature.

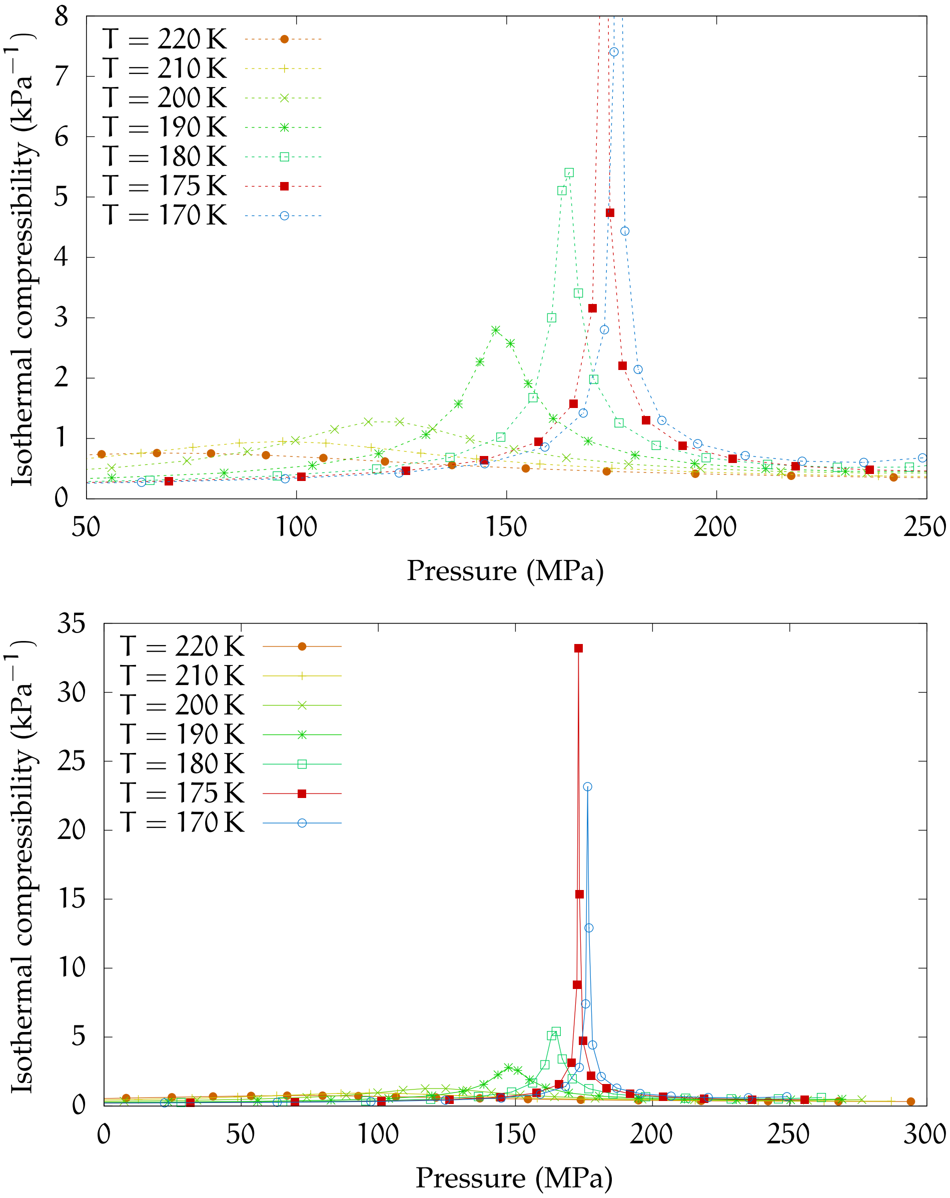

Figure 6.8: Isothermal compressibility κ_T vs pressure p for the $C_1^{Mg(ClO_4)_2}$ solution for temperatures ranging from 220 K to 170 K.

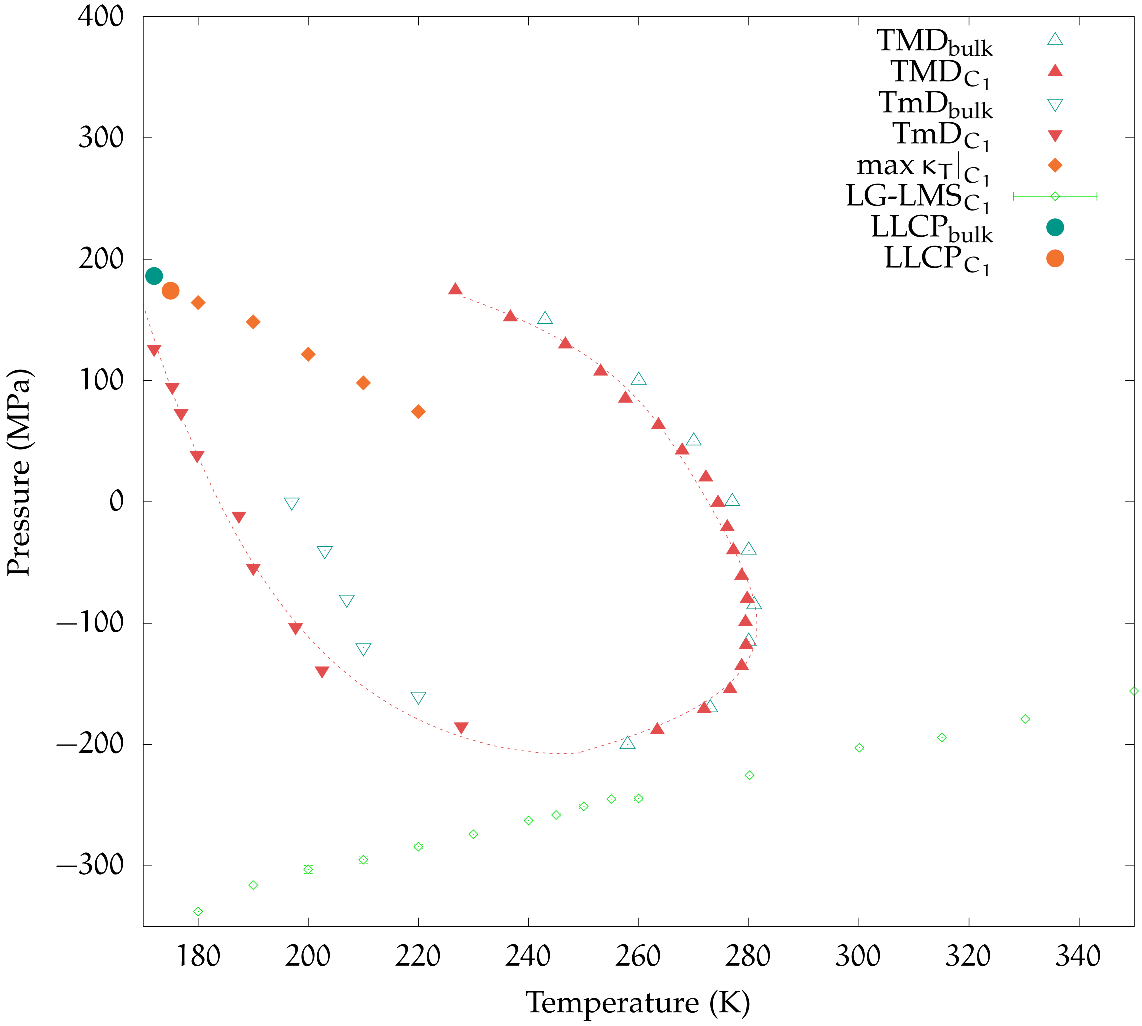

Figure 6.9: Phase diagram of the $C_1^{Mg(ClO_4)_2}$ solution without the isochores. The figure shows the LLCP, the TMD and the TmD curves for the solution compared to the values known in literature for the bulk (Debenedetti et al., 2020; Biddle et al., 2017). The figure also shows the LG-LMS and the state points corresponding to the peaks of the isothermal compressibility.

6.2 RESULTS FOR THE $C_2^{Mg(ClO_4)_2} = 24.4$ WT% SOLUTION

The details of the final solution examined, with concentration $C_2^{Mg(ClO_4)_2} = 24.4$ wt%, are provided in Table 6.1 along with those of the other systems discussed in this thesis.

In this section the phase diagram of the $C_2^{Mg(ClO_4)_2}$ solution is calculated by considering MD simulations of the state points of the system over isochores: the simulated densities, as well as the linear lengths of the boxes, are reported in Table 6.5.

The simulations were performed in the canonical ensemble, gradually lowering the temperature from 400 K to 170 K along the isochores.

In the range of densities [1120 kg/m^3, 1160 kg/m^3], intermediate equilibration states at temperatures 195 K, 185 K and 175 K were considered, where no production runs were performed.

The LG-LMS was identified with the isochore at density 970 kg/m^3, at which cavitation occurred.

A snapshot of the system at density $\rho = 1200$ kg/m^3 and temperature $T = 200$ K is reported in Fig. 6.10.

The simulated state points of the $C_2^{Mg(ClO_4)_2}$ solution are plotted in the isochore plane in Fig. 6.11.

To show the extent of the change in thermodynamic behaviour induced by the ions inserted into the system, the isochore at 980 kg/m^3 was highlighted and compared to that of the bulk. As with sodium perchlorate, a shift in pressure and a change in the curvature upon increasing the concentration are observed.

In Fig. 6.11, the estimates of the positions of the TMD and TmD curves (compared with the bulk Biddle et al., 2017), as well as those of the state points corresponding to the estimated peaks of isothermal compressibility, are presented, as obtained directly from the simulation. The figure also includes the position of the LLCP calculated in Debenedetti et al., 2020.

To further refine the calculations, the isochores were fitted via sixth-degree polynomials. A representation of the equation of state of the system complete with the fitted isochores is thus provided in Fig. 6.12.

Figure 6.12 also displays the TMD and TmD curves compared with the bulk (Biddle et al., 2017). For these curves, a downward shift in temperature compared to the bulk is evident. Unlike the $C_2^{NaClO_4}$ solution, no significative shift in pressure is apparent.

Within the temperature range explored in the PhD programme, no crossing was detected, although the fitted isochores at 1145 kg/m^3 and 1140 kg/m^3 are very close at the lowest considered temperature of 170 K.

That at low temperatures the system is not in a critical regime is evident by analysing its equation of state in the isotherm plane near this region of state points. As it is evident from both the representation of the state points in Fig. 6.13 and the fits with fifth-degree polynomials in Fig. 6.14, although there are inflexion points, none of them has a horizontal tangent or a nearly flat curvature.

DENSITY	BOX LENGTH
970 kg/m^3	5.271 nm
980 kg/m^3	5.253 nm
990 kg/m^3	5.235 nm
1000 kg/m^3	5.218 nm
1010 kg/m^3	5.200 nm
1020 kg/m^3	5.183 nm
1030 kg/m^3	5.167 nm
1040 kg/m^3	5.150 nm
1050 kg/m^3	5.134 nm
1060 kg/m^3	5.117 nm
1070 kg/m^3	5.101 nm
1080 kg/m^3	5.086 nm
1090 kg/m^3	5.070 nm
1100 kg/m^3	5.055 nm
1110 kg/m^3	5.039 nm
1120 kg/m^3	5.024 nm
1125 kg/m^3	5.017 nm
1130 kg/m^3	5.009 nm
1135 kg/m^3	5.002 nm
1140 kg/m^3	4.995 nm
1145 kg/m^3	4.987 nm
1150 kg/m^3	4.980 nm
1155 kg/m^3	5.180 nm
1160 kg/m^3	4.966 nm
1170 kg/m^3	4.952 nm
1180 kg/m^3	4.938 nm
1190 kg/m^3	4.924 nm
1200 kg/m^3	4.910 nm

Table 6.5: Simulated densities for the $C_2^{Mg(ClO_4)_2}$ solution with the corresponding box lengths.

TEMPERATURE	EQUILIBRATION TIME	PRODUCTION TIME
400 K	0.1 ns	0.1 ns
380 K	0.1 ns	0.1 ns
350 K	0.1 ns	0.1 ns
330 K	0.1 ns	0.1 ns
315 K	0.1 ns	0.1 ns
305 K	0.1 ns	0.1 ns
300 K	0.1 ns	0.1 ns
295 K	0.1 ns	0.1 ns
290 K	0.1 ns	0.1 ns
285 K	0.1 ns	0.1 ns
280 K	0.5 ns	0.5 ns
275 K	0.5 ns	0.5 ns
270 K	0.5 ns	0.5 ns
265 K	0.5 ns	0.5 ns
260 K	1 ns	1 ns
255 K	1 ns	1 ns
250 K	1 ns	1 ns
245 K	1 ns	1 ns
240 K	10 ns	10 ns
230 K	10 ns	10 ns
220 K	20 ns	20 ns
210 K	20 ns	20 ns
200 K	40 ns	40 ns
195 K*	40 ns	
190 K	40 ns	40 ns
185 K*	40 ns	
180 K	40 ns	40 ns
175 K*	40 ns	
170 K	40 ns	40 ns

*Only for isochores at densities $\rho \in [1120\,\mathrm{kg/m^3}, 1155\,\mathrm{kg/m^3}]$.

Table 6.6: Simulation times for the $C_2^{Mg(ClO_4)_2}$ solution.

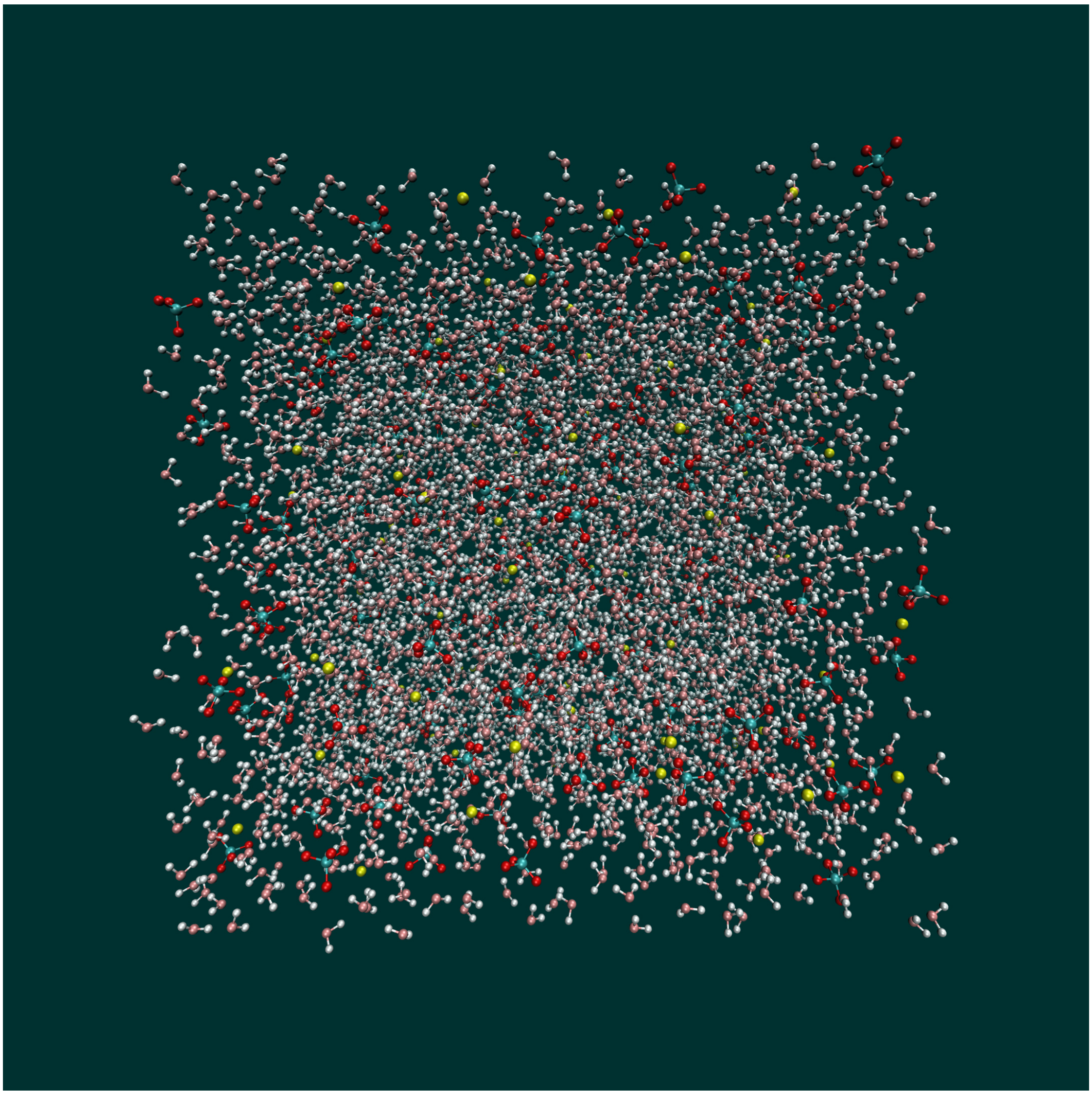

Figure 6.10: Snapshot of a $C_2^{Mg(ClO_4)_2} = 24.4$ wt% solution at density $\rho = 1100\,\mathrm{kg/m^3}$ and temperature $T = 200\,\mathrm{K}$. Water is shown in pink (oxygen) and grey (hydrogens), magnesium in yellow and perchlorates in teal (chlorine) and red (oxygens).

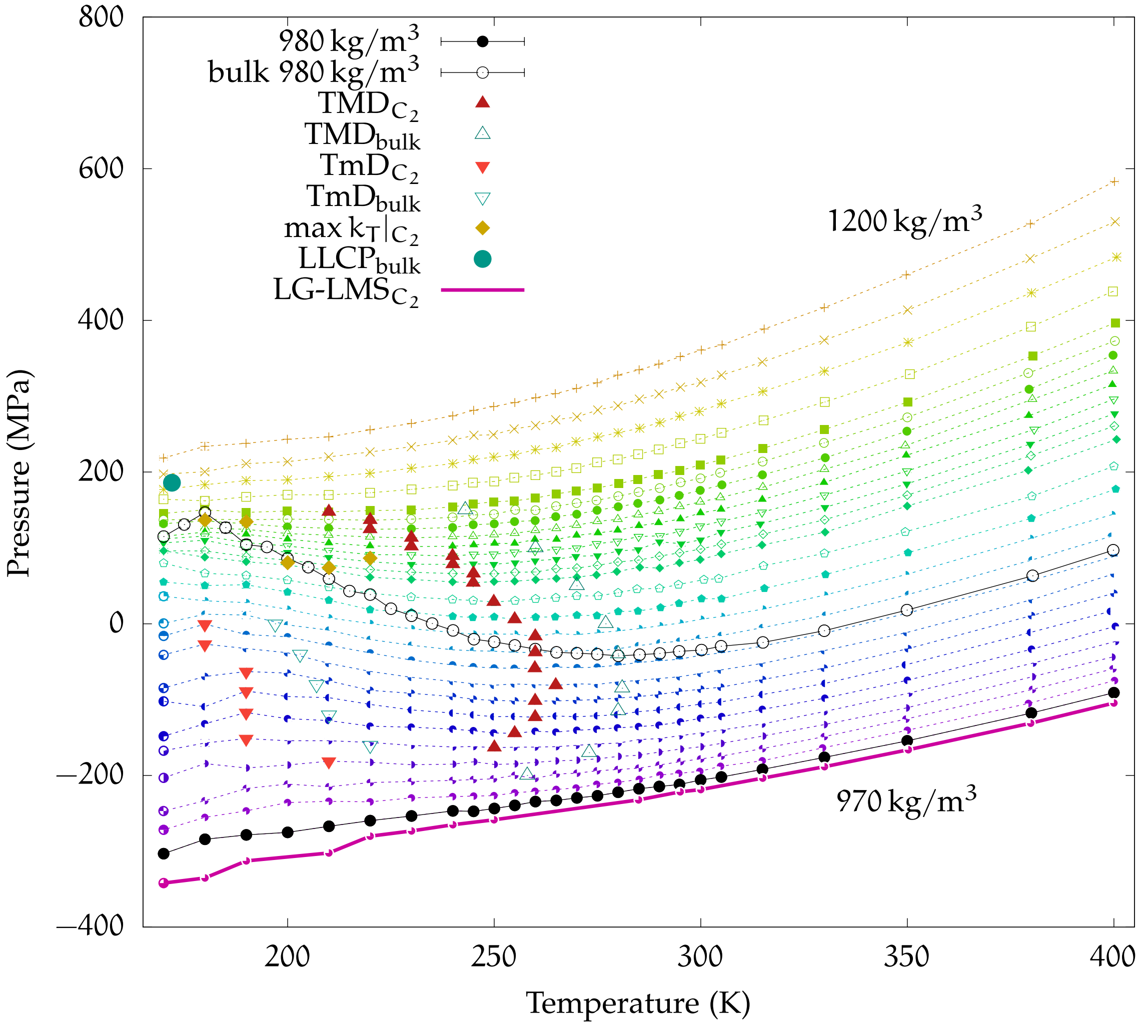

Figure 6.11: Unfitted simulated state points of the $C_2^{Mg(ClO_4)_2}$ solution in the (p, T) plane, for densities ranging from $\rho = 970\,kg/m^3$ to $\rho = 1200\,kg/m^3$, with increments $\Delta\rho = 10\,kg/m^3$ except in the region $[1120\,kg/m^3, 1160\,kg/m^3]$ where it is $\Delta\rho = 5\,kg/m^3$. Simulated temperatures range from $T = 400\,K$ to $T = 170\,K$. The symbols represent state points derived from simulations, while the lines serve as a visual guide. Error bars are plotted but not visible. Included are initial estimates of the Temperature of Maximum Density (TMD) curves for the solution, shown as red-filled upward triangles, alongside bulk data (empty teal upward triangles) from Biddle et al., 2017. Downward triangles denote the TmDs. The teal-filled circle marks the bulk Liquid-Liquid Critical Point (LLCP) as per Debenedetti et al., 2020 and filled diamonds indicate the isothermal compressibility maxima obtained from the data. The thick dash-dotted line at the bottom represents the $880\,kg/m^3$ isochore, coinciding with the system's Liquid-Gas Limit of Mechanical Stability (LG-LMS). The $980\,kg/m^3$ isochore data for both the $C_2^{Mg(ClO_4)_2}$ solution (filled black circles) and the bulk (empty black circles) is highlighted. Further refined estimates of the TMDs, TmDs and isothermal compressibility maxima will be provided subsequently.

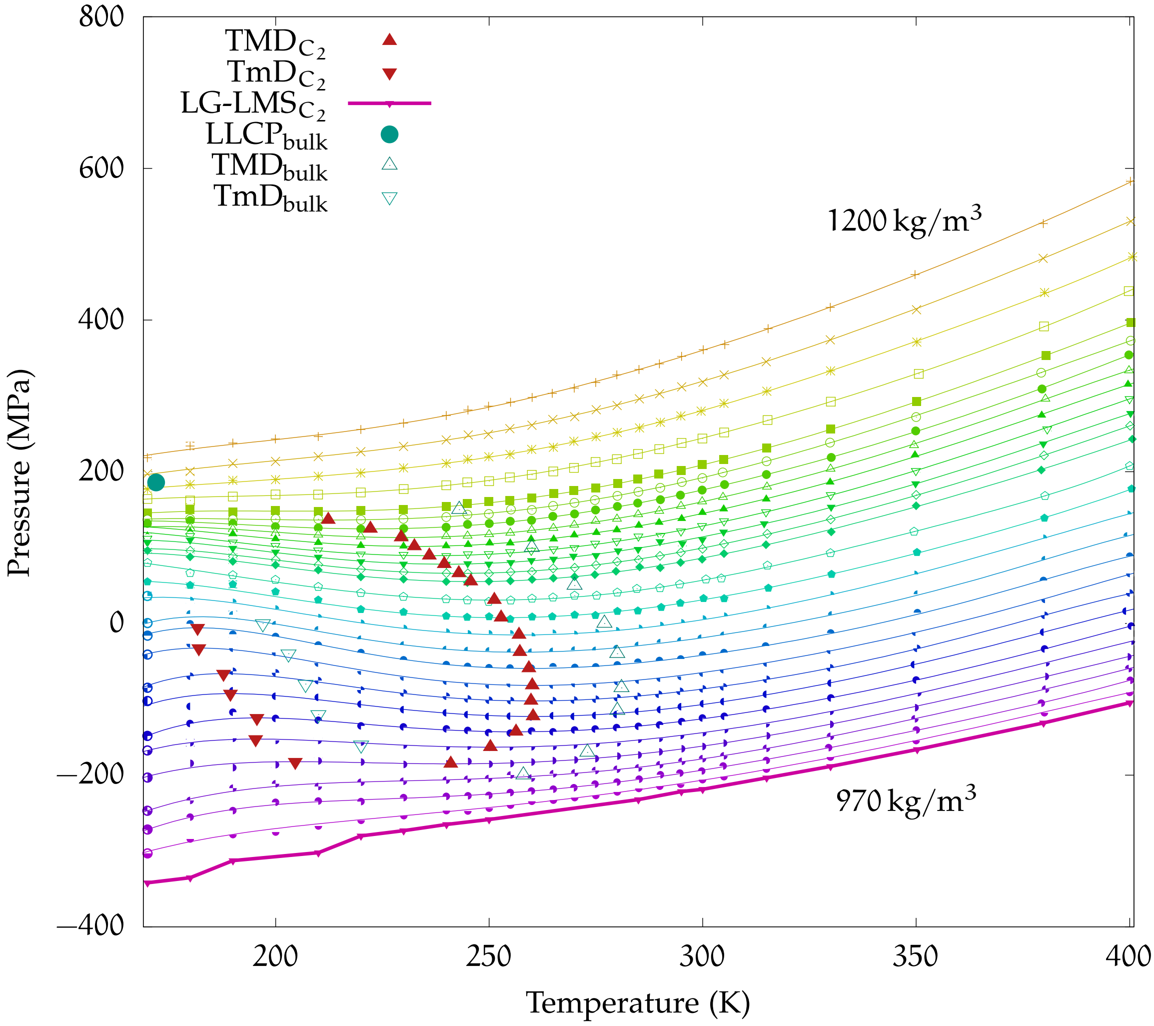

Figure 6.12: Equation of state in the isochore plane for the $C_2^{Mg(ClO_4)_2}$ solution obtained from MD simulations covering densities ranging from $\rho = 1140\,kg/m^3$ to $880\,kg/m^3$ (LG-LMS) with an incremental change of $\Delta\rho = 10\,kg/m^3$ except in the region $[1120\,kg/m^3, 1160\,kg/m^3]$ where it is $\Delta\rho = 5\,kg/m^3$. Error bars are plotted but not visible. Polynomial fittings have been applied to the simulated data points and the resulting isochores are reported with solid lines. The teal-filled circle is the TIP4P/2005 bulk LLCP as computed in Debenedetti et al., 2020. The solution's TMDs (upward triangles) and the TmDs (downward triangles) obtained from the fits are highlighted in red and compared to the values known in literature for the bulk TIP4P/2005 (see Biddle et al., 2017) and here reported with teal empty triangles.

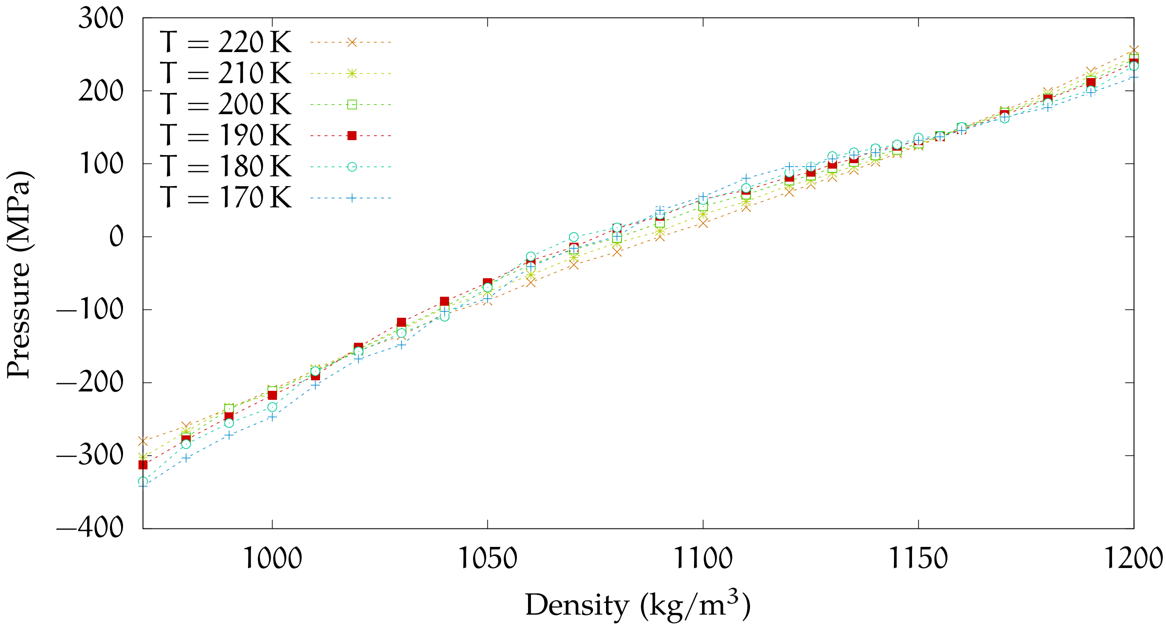

Figure 6.13: Simulated state points for the $C_2^{Mg(ClO_4)_2}$ solution plotted in the isotherm plane. The dashed lines are a guide for the eye.

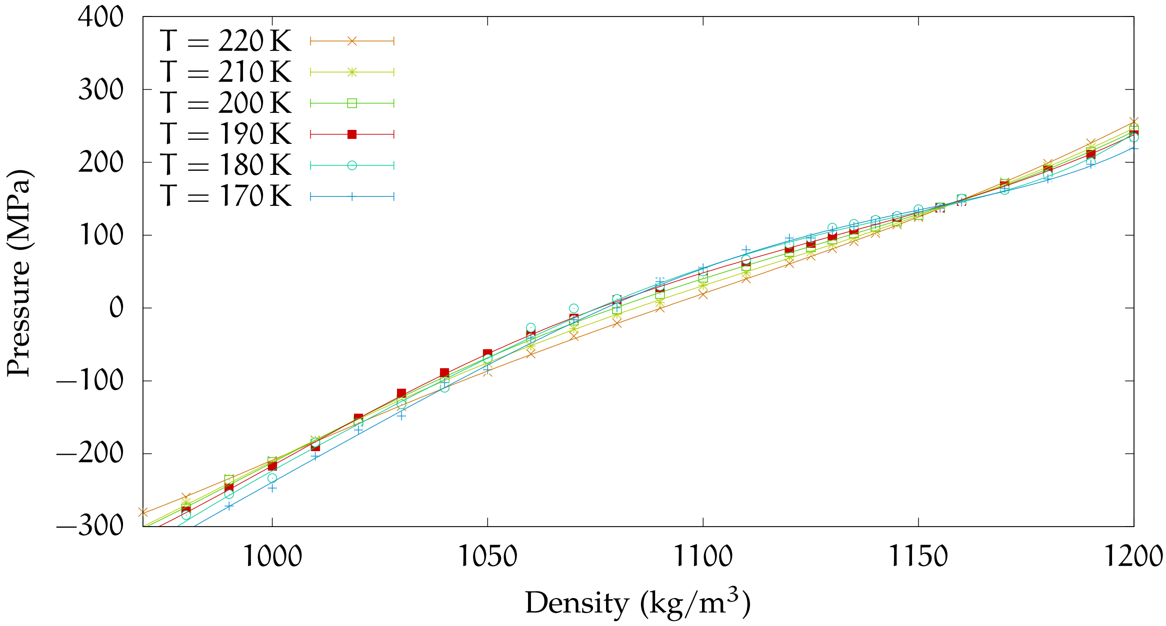

Figure 6.14: Equation of state in the isotherm plane for the $C_2^{Mg(ClO_4)_2}$ solution. Error bars are plotted but not visible. Lines are isotherm curves $p_T(\rho)$ obtained through polynomial fits to the simulated state points.

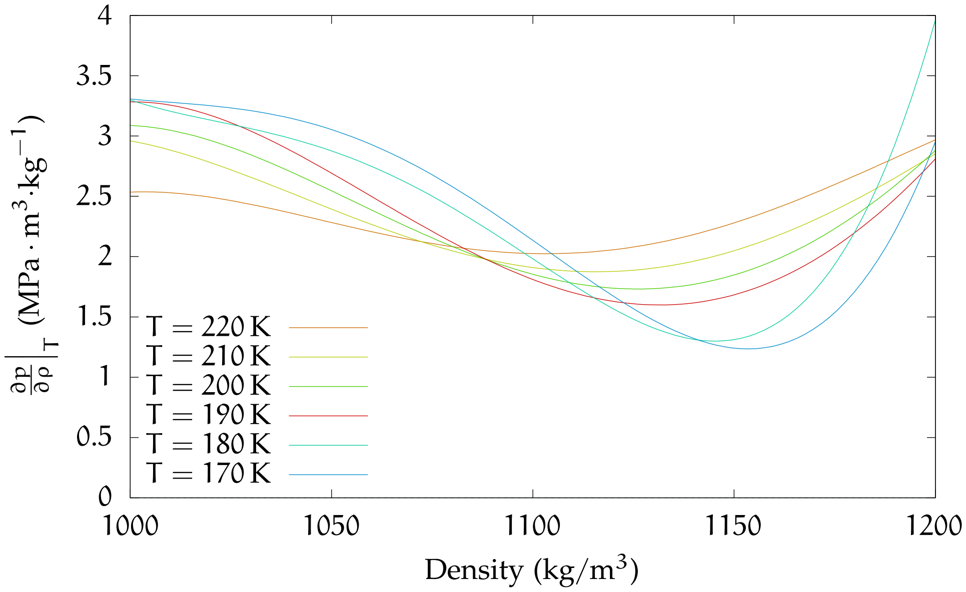

Figure 6.15: Derivative of $p_T(\rho)$ for selected temperatures for the $C_2^{Mg(ClO_4)_2}$ solution. No sign of a flex point in the isotherm plane is evident.

This observation becomes even more evident when looking at the derivatives of the isotherms, as reported in Fig. 6.15. None of the considered curves approaches zero.

Therefore, no critical points are observed for the $C_2^{Mg(ClO_4)_2}$ solution in this range of temperatures.

Nevertheless, observing the behaviour of isothermal compressibility in Fig. 6.16, it is clear that a line of maxima exists. Thus, it is not ruled out that these maxima might be anticipating the onset of a critical region at lower temperatures.

Furthermore, a shift of the critical point to lower temperatures could imply a lower glass transition temperature and thus a higher stabilisation of the supercooled phase, therefore providing a further explanation for why water on Mars would be liquid at temperatures that low, magnesium perchlorate being a much more abundant salt there than sodium perchlorate.

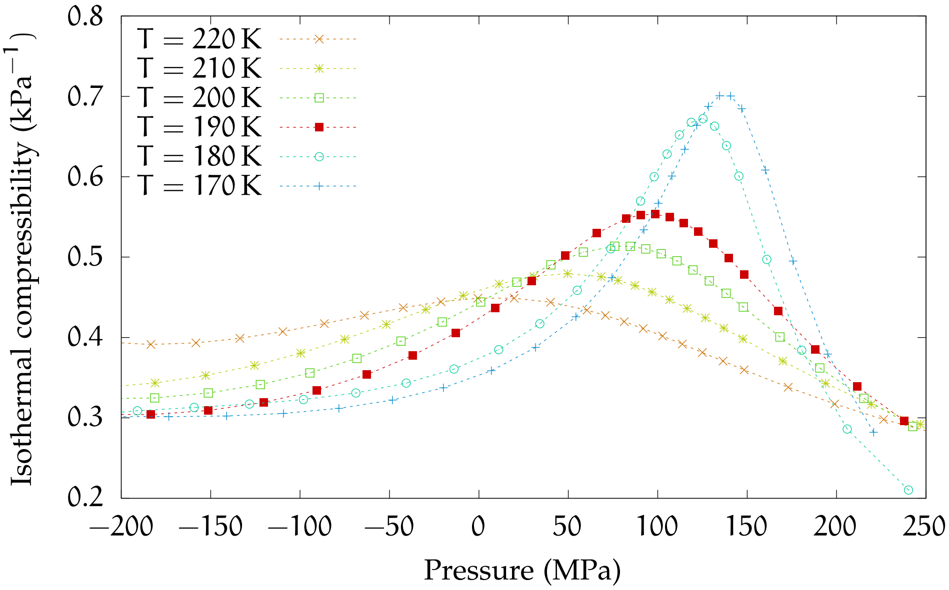

Figure 6.16: Isothermal compressibility κ_T vs pressure p for the $C_2^{Mg(ClO_4)_2}$ solution for temperatures ranging from 220 K to 170 K.

6.3 COMPARISON

Figure 6.17 shows the phase diagrams of the four solutions investigated. To facilitate an immediate comparison between the four systems, a symmetric colour coding has been chosen for sodium perchlorate and magnesium perchlorate. In red and orange, the thermodynamic quantities for the C_1 solutions are displayed, while light and dark yellow indicate those for the C_2 solutions. Teal was chosen for the bulk. Simulated state points reported in green and blue mark the limits of mechanical stability.

LIQUID-LIQUID CRITICAL POINT When considering the LLCP across the solutions, with respect to the bulk:

$C_1^{NaClO_4}$: the LLCP has a slight shift downwards in pressure but T_C is barely affected by the presence of ions;

$C_2^{NaClO_4}$: T_C shifts to a higher temperature and p_C to a significantly lower pressure;

$C_1^{Mg(ClO_4)_2}$: T_C shifts slightly upwards in temperature, p_C slightly downwards in pressure;

$C_2^{Mg(ClO_4)_2}$: no critical points were found in the considered ranges of temperature and densities, although it is possible that an LLCP exists at lower temperatures, possibly shifting the glass transition at a lower temperature and hence better stabilising the supercooled phase.

Across all the systems considered, when a ρ_C was found, it always shifted upwards in densities upon increasing the concentration of the solutes.

(a) Sodium Perchlorate

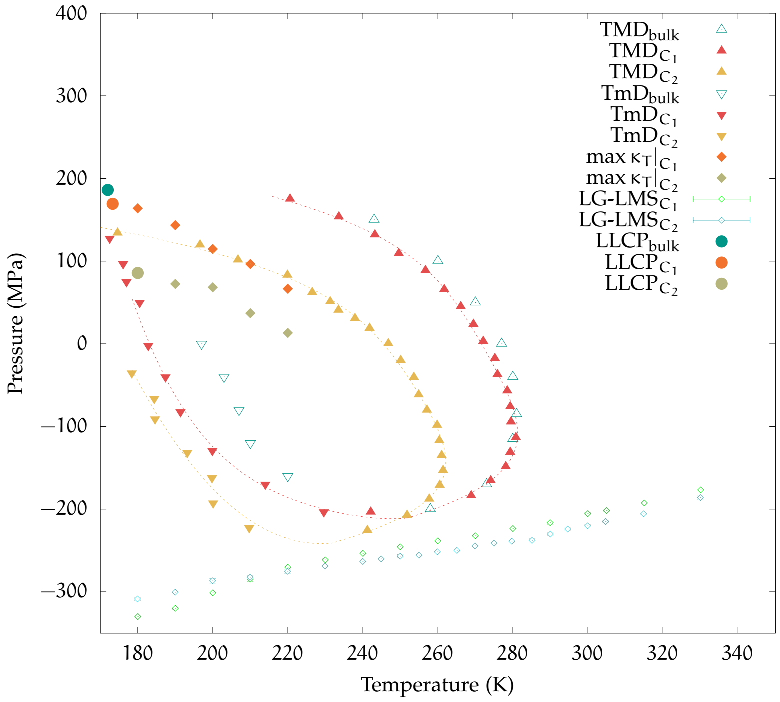

(b) Magnesium Perchlorate

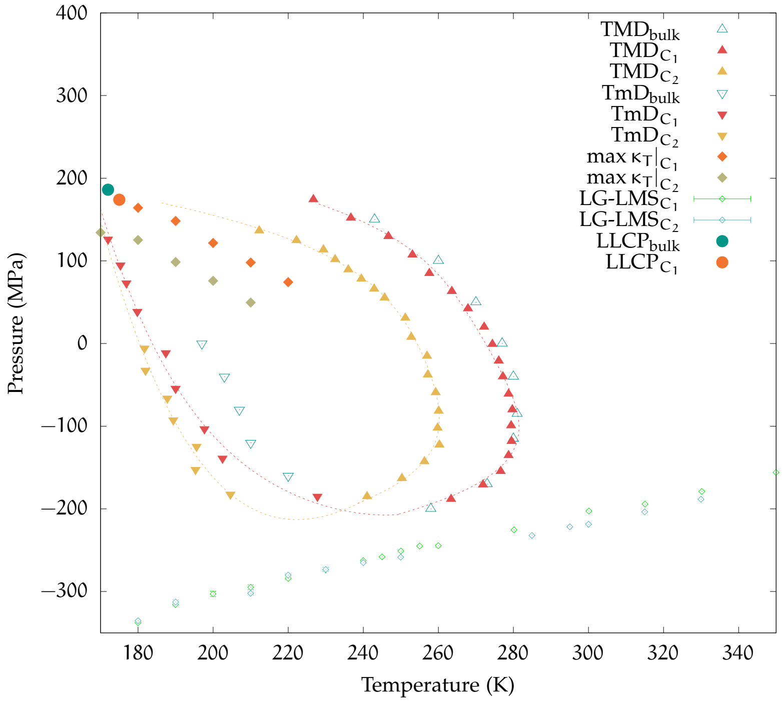

Figure 6.17: Thermodynamic features of the systems investigated in the PhD programme. The the TMD and TmD curves are plotted and compared to the bulk (as per Biddle et al., 2017). The calculated LLCPs are also shown, as well as the bulk one (Debenedetti et al., 2020). The figures also show the points of maximum of the isothermal compressibility and the LG-LMS for the four solutions considered. The positions of the HDL-LDL coexistence line and the HDL LMS here shown are hypothesised, as equilibration to eccessively low temperature is not possible in MD simulations (see Sec. 3.3.3). No state points were simulated below $T = 170\,\mathrm{K}$.

ISOTHERMAL COMPRESSIBILITY The line of state points corresponding to the peaks of isothermal compressibility shifts towards lower pressures in both pairs of solutions.

TEMPERATURES OF MAXIMUM AND MINIMUM DENSITIES The TMD and the TmD curves show a similar pattern in T, shifting towards lower temperatures upon increasing the concentrations. The shift is higher for the TMD curve compared to the TmD one. Therefore, upon increasing the concentration of the solutes, a shrinkage in the region of density anomaly is observed. In p, a shifting trend towards lower pressures is noted within the $C_2^{NaClO_4}$ solution but not within the $C_2^{Mg(ClO_4)_2}$ one.

LIQUID-GAS LIMIT OF MECHANICAL STABILITY The location of the LG-LMS does not change much in the (p, T) plane, but shifts upwards in densities.

As described in Section 4.3, the downward shift in the $\{p(\max k_T)\}$ points, together with the essentially constant LG-LMS, leads to a narrower LDL phase, where nucleation is favoured (Gallo et al., 2016), with respect to the bulk. This can explain why perchlorate solutions on Mars would remain liquid at temperatures much lower than their melting point. Schemes of the phase diagrams of the considered solutions showing this behaviour are pictured in Fig. 6.18. The interplay between the HDL and the LDL phase for the aqueous $Mg(ClO_4)_2$ solutions will be shown in the next chapter by means of the RDFs.

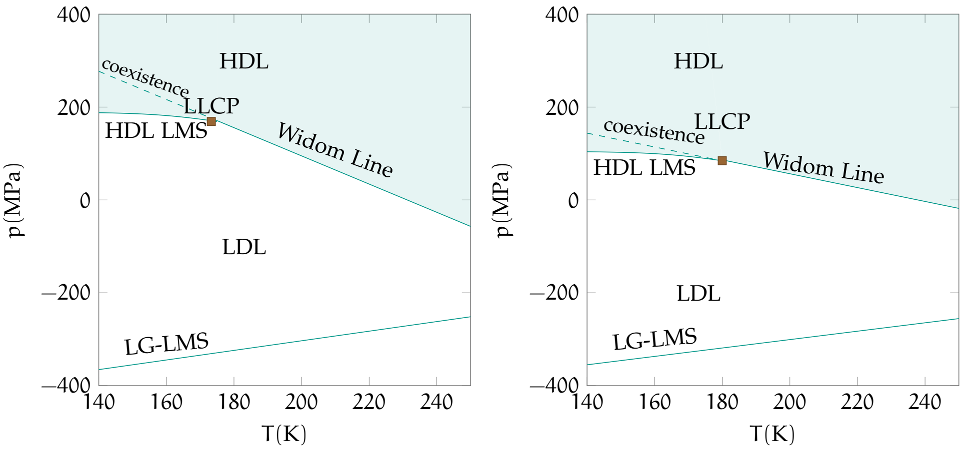

(a) $C_1{}^{NaClO_4} = 1.63\,\mathrm{wt\%}$

(b) $C_2{}^{NaClO_4} = 15.4\,\mathrm{wt\%}$

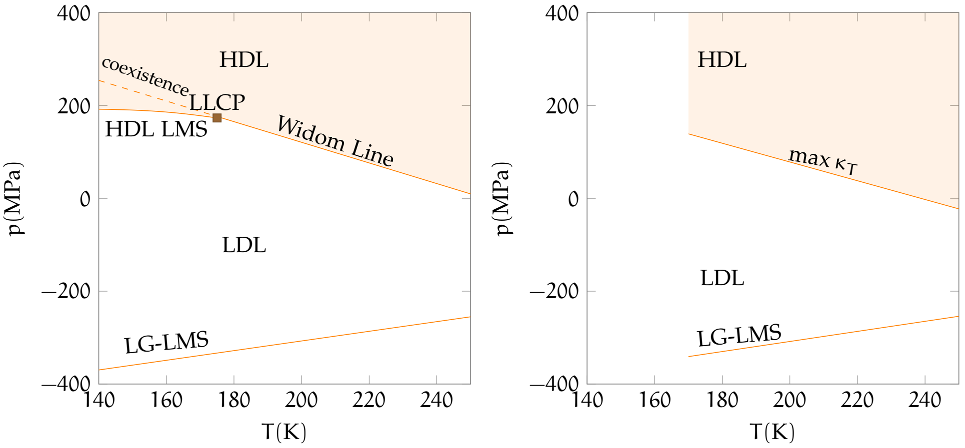

(c) $C_1{}^{Mg(ClO_4)_2} = 2.95\,\mathrm{wt\%}$

(d) $C_2{}^{Mg(ClO_4)_2} = 24.4\,\mathrm{wt\%}$

Figure 6.18: Schematic phase diagrams of the considered solutions, clearly showing the LDL region shrinking upon increasing the ionic concentrations.

7

STRUCTURAL RESULTS: $Mg(ClO_4)_2$ SOLUTIONS

In this chapter, the structural analysis of the two aqueous magnesium perchlorate solutions previously introduced will be performed. The analyses carried out in the case of sodium perchlorate had shown that the main effect of adding ions to the solution was a contraction of the LDL region, resulting in a persistence of the dichotomous behaviour of water and featuring an interplay between the HDL and the LDL phases. This result was consistent with the thermodynamic investigations, which showed that the LLCP shifted to higher temperatures and lower pressures, the Widom Line was lowered in pressure, the TMD curve shifted to lower temperatures and pressures but the LG-LMS remained substantially unchanged.

In the case of magnesium perchlorate, the ${C_1}^{Mg(ClO_4)_2}$ solution exhibited, similarly to the ${C_1}^{NaClO_4}$ solution, a LLCP at a state point close to the bulk one. The equation of state of the supercooled ${C_2}^{Mg(ClO_4)_2}$ solution, instead, did not show the occurrence of any critical point in the temperature range considered. However, for the ${C_2}^{Mg(ClO_4)_2}$ solution, the pressure corresponding to the peaks of the isothermal compressibility decreased, the TMD shifted to lower temperatures and the position of the LG-LMS remained essentially unchanged. The trends in the maxima of isothermal compressibility could imply a potential convergence to a Widom Line and, possibly, anticipate a critical point at lower temperatures. Hence, a similar contraction of the LDL region as the one observed in sodium perchlorate and in methanol (Corradini et al., 2012) is possible.

7.1 WATER-WATER RADIAL DISTRIBUTION FUNCTIONS

The structural features of the systems can be inferred by analysing the radial distribution function (RDF) $g(r)$ as already done in Chapter 5.

Denoted by ρ_C is the density at concentration C, the bulk being ρ_0. Following the approach taken in the sodium perchlorate analysis, three sets of densities were considered for the three systems:

HIGH-DENSITY TRIPLET

$$\begin{cases} \rho_0 = 1110\,\mathrm{kg/m^3} \\ \rho_{C_1} = 1110\,\mathrm{kg/m^3} \\ \rho_{C_2} = 1200\,\mathrm{kg/m^3}\,; \end{cases}$$

MEDIUM-DENSITY TRIPLET

$$\begin{cases} \rho_0 = 990\,\mathrm{kg/m^3} \\ \rho_{C_1} = 990\,\mathrm{kg/m^3} \\ \rho_{C_2} = 1130\,\mathrm{kg/m^3}\,; \end{cases}$$

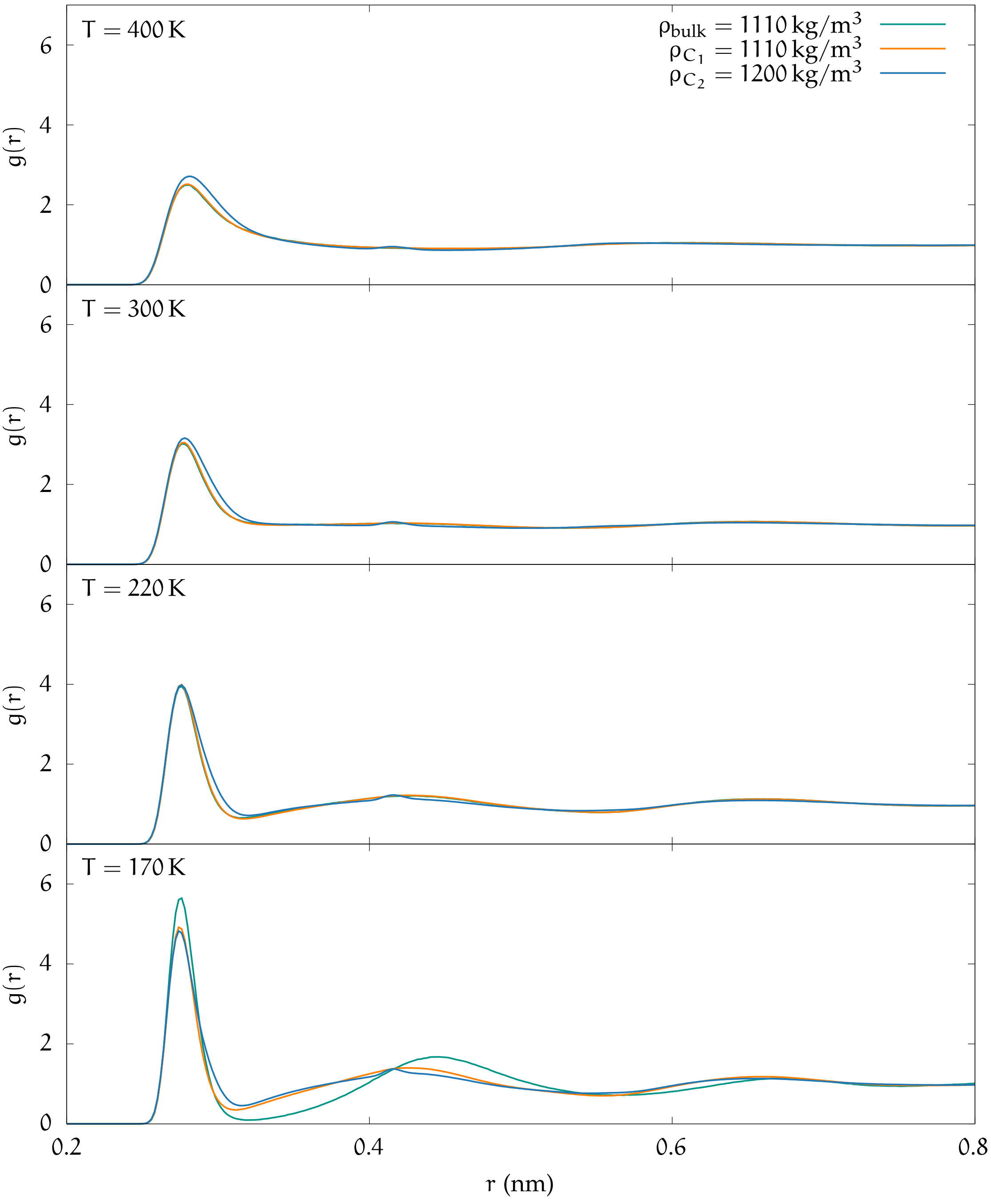

Figure 7.1: Water-Water RDF for the high-density set of the bulk and the $Mg(ClO_4)_2$ solutions. At the lowest temperature investigated the bulk is clearly in the LDL phase.

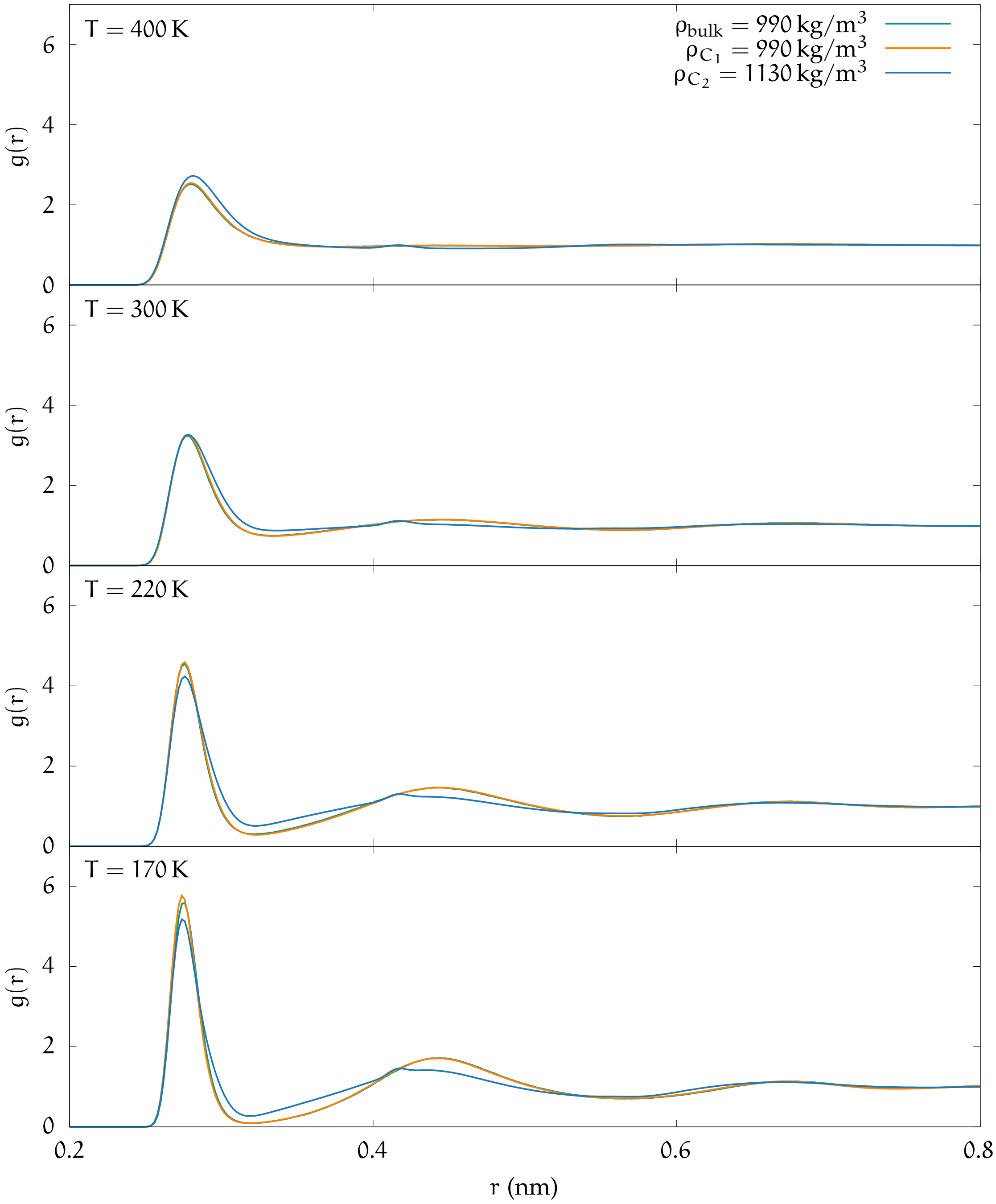

Figure 7.2: Water-Water RDF for the medium-density set of the bulk and the $Mg(ClO_4)_2$ solutions. The bulk and the $C_1{}^{Mg(ClO_4)_2}$ solution have a very similar behaviour and appear to be in the LDL phase at low temperatures. Even though the thermodynamic behaviours of the three systems are similar, structurally the $C_2{}^{Mg(ClO_4)_2}$ solution appears to behave like the higher densities in Fig. 7.1.

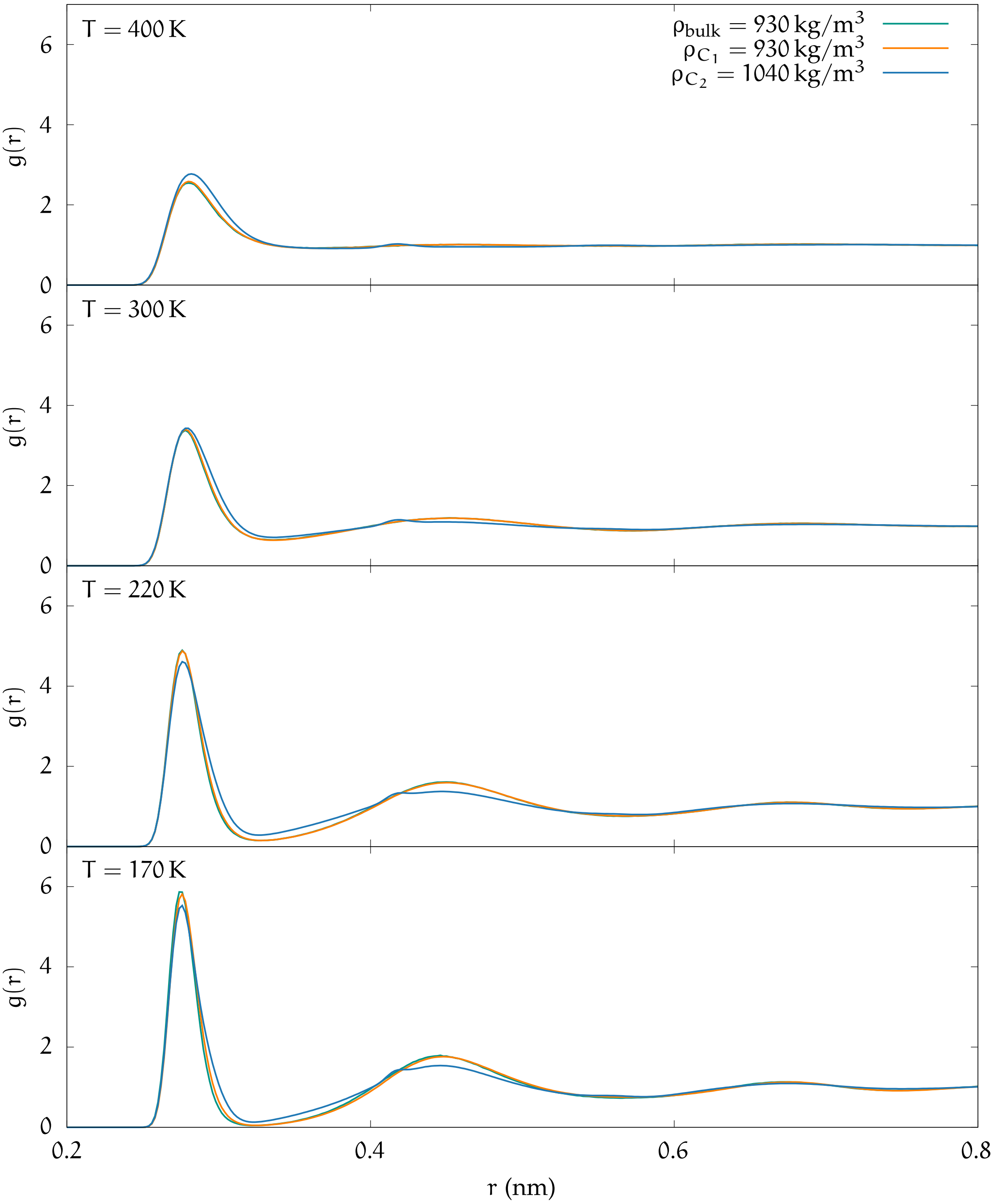

Figure 7.3: Water-Water RDF for the low-density set of the bulk and the $Mg(ClO_4)_2$ solutions. All the systems considered appear to be in the LDL phase at low temperature. The $C_1^{Mg(ClO_4)_2}$ solution closely matches the bulk, as in Fig. 7.2.

LOW-DENSITY TRIPLET

$$\begin{cases} \rho_0 = 930\,\mathrm{kg/m^3} \\ \rho_{C_1} = 930\,\mathrm{kg/m^3} \\ \rho_{C_2} = 1040\,\mathrm{kg/m^3}\,. \end{cases}$$

The densities were chosen by picking the isochores with similar thermodynamic behaviour at low temperature.

Next, the water radial oxygen-oxygen distribution functions $g_{O_W-O_W}(r)$ can be considered.

Reminding that, for these functions, a pronounced first minimum followed by a sharp local maximum indicates the LDL phase, while a gentler first minimum and a less pronounced second maximum are indicative of the HDL phase (Corradini et al., 2011; Gallo et al., 2011; Soper, 2017), their behaviour can be checked in the figures 7.1, 7.2 and 7.3.

The results are quite similar to those of sodium perchlorate.

- Albeit with some differences between the various systems, down to 300 K all the solutions considered are in the HDL phase. By decreasing the temperature, a more LDL-like behaviour gradually begins to appear.
- Such behaviour is very noticeable for the bulk at each of the considered densities and only slightly less so for the $C_1{}^{Mg(ClO_4)_2}$ solution. Actually, except for the last panel in figure 7.1 ($T = 170\,K$), the $g_{O_W-O_W}(r)$ of the $C_1{}^{Mg(ClO_4)_2}$ solution matches the bulk at every density and temperature, with some minor variations that can be attributed to the slight ion-induced shifts in pressure.
- The $C_2{}^{Mg(ClO_4)_2}$ solution, on the other hand, while having a trend not dissimilar to that of the other systems, only exhibits a distinctly LDL behaviour at low temperatures at the lowest of the densities considered.

The liquid is less LDL when the ionic concentration is increased.

Therefore, while increasing the ion concentration, water retains its anomalous structural behaviour and the liquid is more HDL in character.

7.1.1 *Coordination Number*

Using the definitions reported in Eq. (5.2) and Eq. (5.3), it is possible to consider the coordination number for the two solutions currently under investigation.

Figure 7.4 illustrates the $O_W - O_W$ first-shell coordination numbers evaluated at selected temperatures across varying densities. The graphs in Fig. 7.4 resemble those in Fig. 5.4, which is explained by how similar the relative $g_{O_W-O_W}(r)$ behaved both in magnesium and in sodium perchlorate solutions.

Since the first RDF minimum remained almost unchanged at low temperatures for each concentration, a constant cutoff distance r_0 was chosen for all densities: $r_0 = 0.330\,\mathrm{nm}$ for the $C_1{}^{Mg(ClO_4)_2}$ solution and $r_0 = 0.327\,\mathrm{nm}$ for the $C_2{}^{Mg(ClO_4)_2}$ solution.

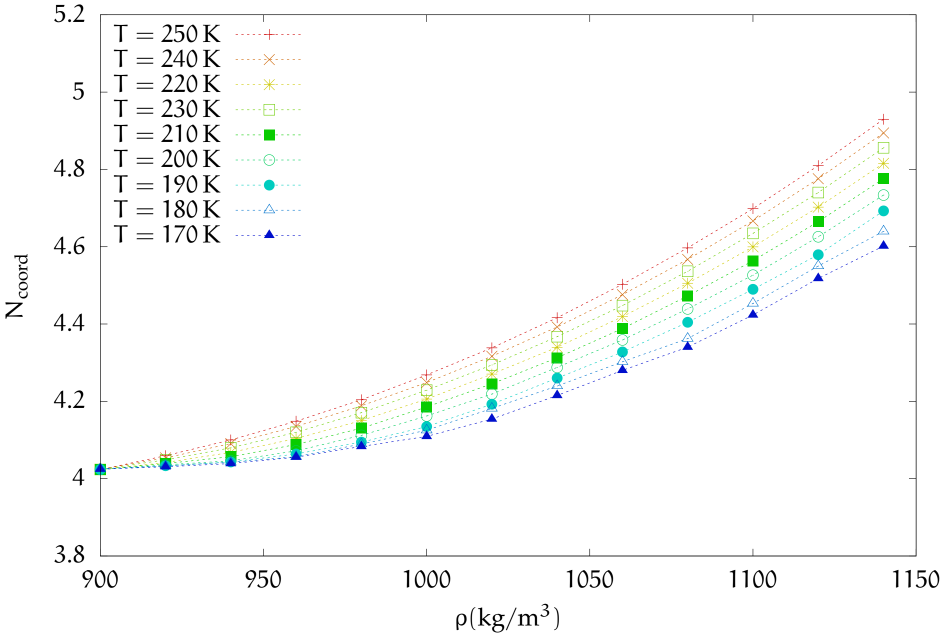

(a) $C_1{}^{Mg(ClO_4)_2} = 2.95$ wt%

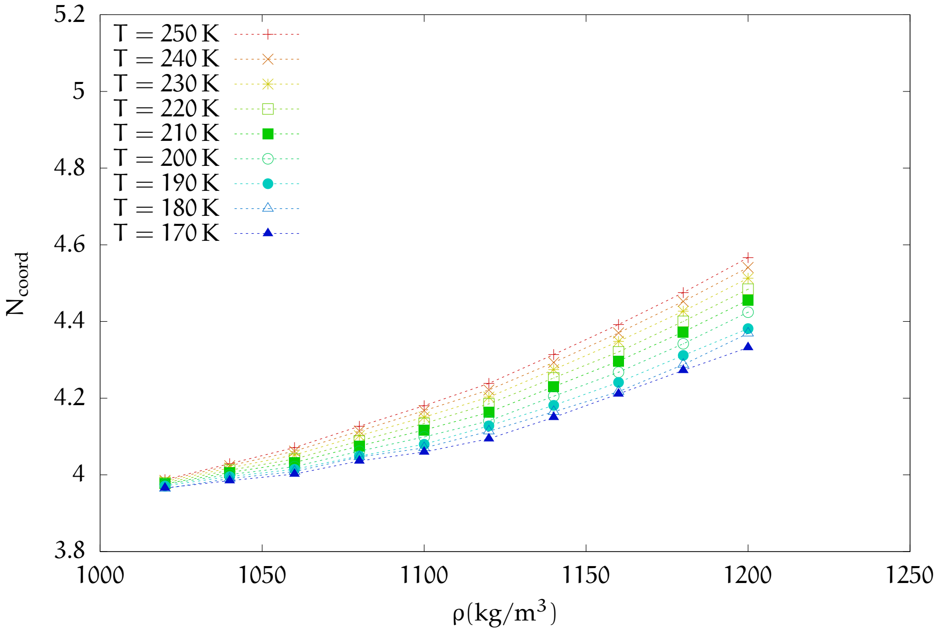

(b) $C_2{}^{Mg(ClO_4)_2} = 24.4$ wt%

Figure 7.4: $O_W - O_W$ first shell coordination numbers for selected temperatures as a function of density for the C_1 and the C_2 $Mg(ClO_4)_2$ solutions.

As densities increase, the coordination numbers for both concentrations exhibit an upward trend with comparable slopes. The curves shift downwards as concentration rises, reflecting the increased solubility of the ions in a more HDL phase.

At lower temperatures, the coordination number approaches 4, thereby confirming the presence of LDL water in both solutions.

7.2 ION-WATER AND ION-ION RADIAL DISTRIBUTION FUNCTIONS

Figure 7.5 and Fig. 7.6 depict the alternation in the arrangement of ions within the $C_2^{Mg(ClO_4)_2}$ solution by considering the $\mathrm{Cl-H}$, $\mathrm{Cl-Mg}$, $\mathrm{Cl-O_W}$ and $\mathrm{Cl-Cl}$ RDFs at densities $\rho_{C_2^{Mg(ClO_4)_2}} = 1200\,\mathrm{kg/m^3}$ (Fig. 7.5) and $\rho_{C_2^{Mg(ClO_4)_2}} = 1040\,\mathrm{kg/m^3}$ (Fig. 7.6). Results were comparable across the two concentrations but only the highest concentration, being more representative, will be shown and discussed.

ION-WATER INTERACTION The feature of the chlorine ion to be surrounded by a cage of water molecules previously observed in sodium perchlorate solutions (Sec. 5.3) is also present here, as can be inferred from the fact that the first ion to appear in Figs. 7.5 and 7.6 is hydrogen, followed in order by magnesium, the oxygen of water, and chlorine.

ION PAIRING The ion pairing first peak rises significantly as the temperature drops. This result is consistent with the reduced solubility of ions in the LDL phase, causing them to be closer. An increase in the ion pairing first peak was observed in sodium perchlorate in section 5.3 upon decreasing the density. This phenomenon is much less pronounced for $Mg(ClO_4)_2$ (Fig. 7.7), since the ion pairing first peak is similarly high at high density, due to the stronger electromagnetic interaction between Mg^{2+} and ClO_4^- ions compared to Na^+ and ClO_4^-.

Ion Pairing is favoured at low temperatures, confirming LDL water is present

$\mathrm{Cl-Cl}$ INTERACTION Focusing on the $\mathrm{Cl-Cl}$ interaction, compared to sodium perchlorate, the heights of the peaks, the first of which always appears around $0.48\,\mathrm{nm}$, are lower: this is consistent with the stronger interaction between the magnesium ion and the perchlorate ion. The absence of ordering at low temperatures should be highlighted, in line with experimental observations showing that the supercooled phase of magnesium perchlorate is more stable than that of sodium perchlorate (Toner et al., 2014).

No ordering effects are evident in the $\mathrm{Cl-Cl}$ RDF.

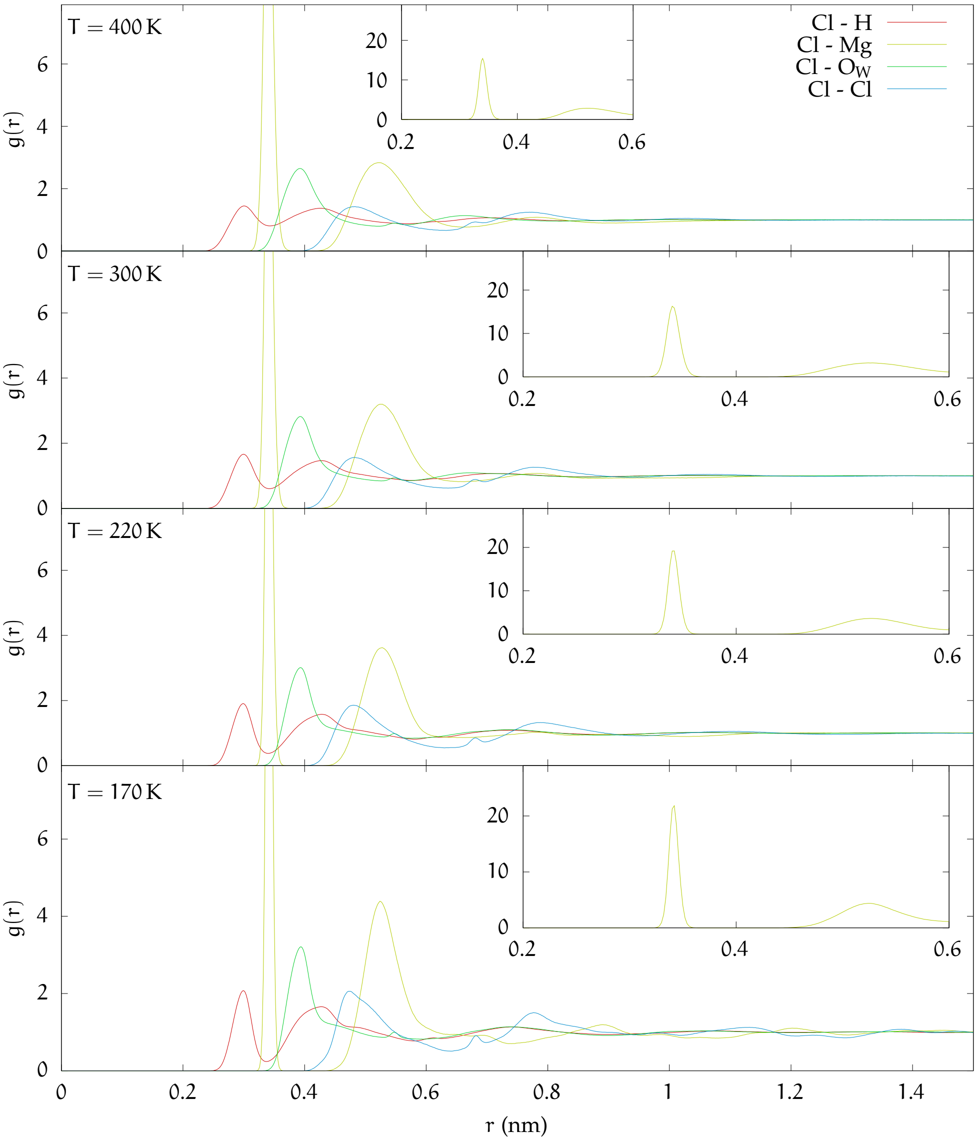

Figure 7.5: Radial distribution functions for Cl − H, Cl − Mg, Cl − O_W and Cl − Cl in the $C_2^{Mg(ClO_4)_2}$ solution at $\rho = 1200\,kg/m^3$. The insets display the Cl–Mg RDF separately, using different scales to emphasise the height of the first peak.

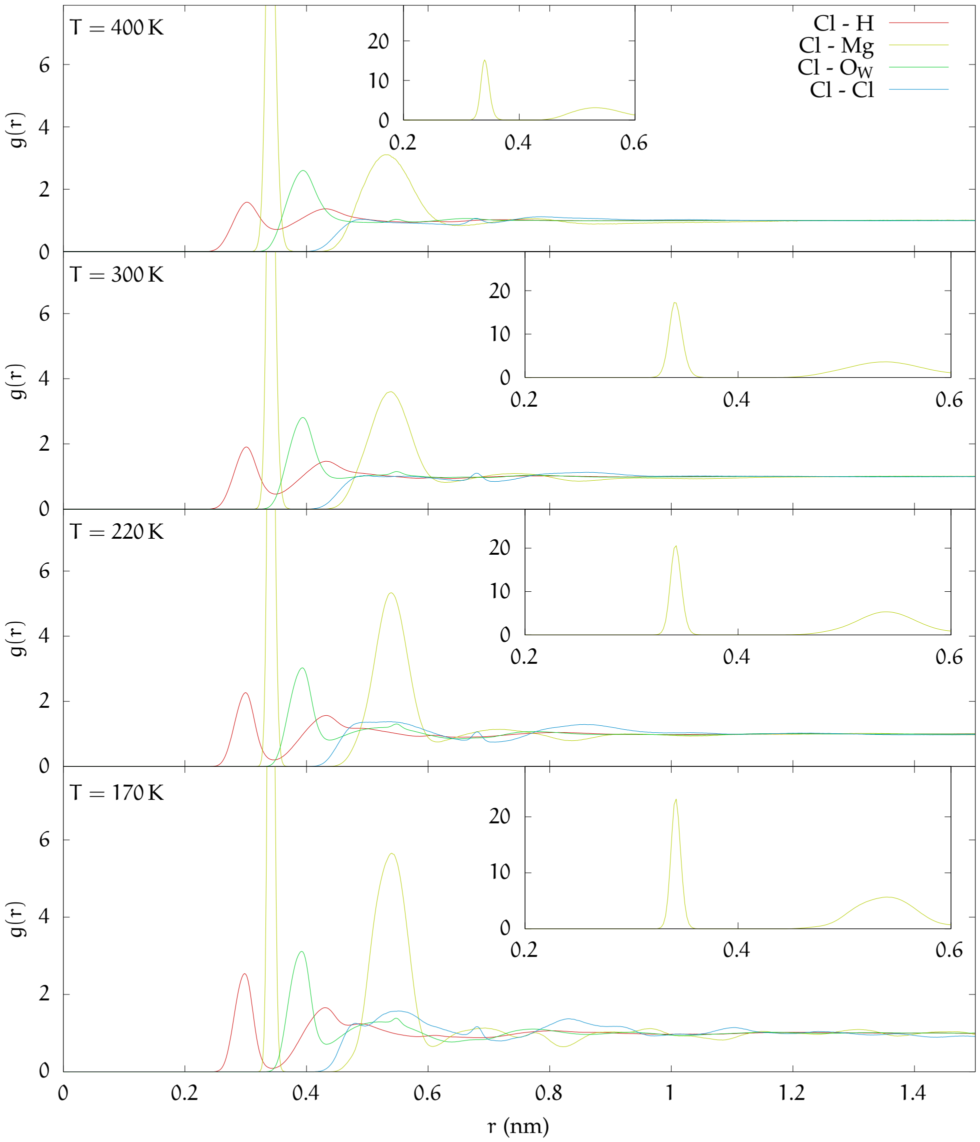

Figure 7.6: Radial distribution functions for $Cl - H$, $Cl - Mg$, $Cl - O_W$ and $Cl - Cl$ in the $C_2{}^{Mg(ClO_4)_2}$ solution at density $\rho = 1040\,kg/m^3$. The insets display the Cl–Mg RDF separately, using different scales to emphasise the height of the first peak.

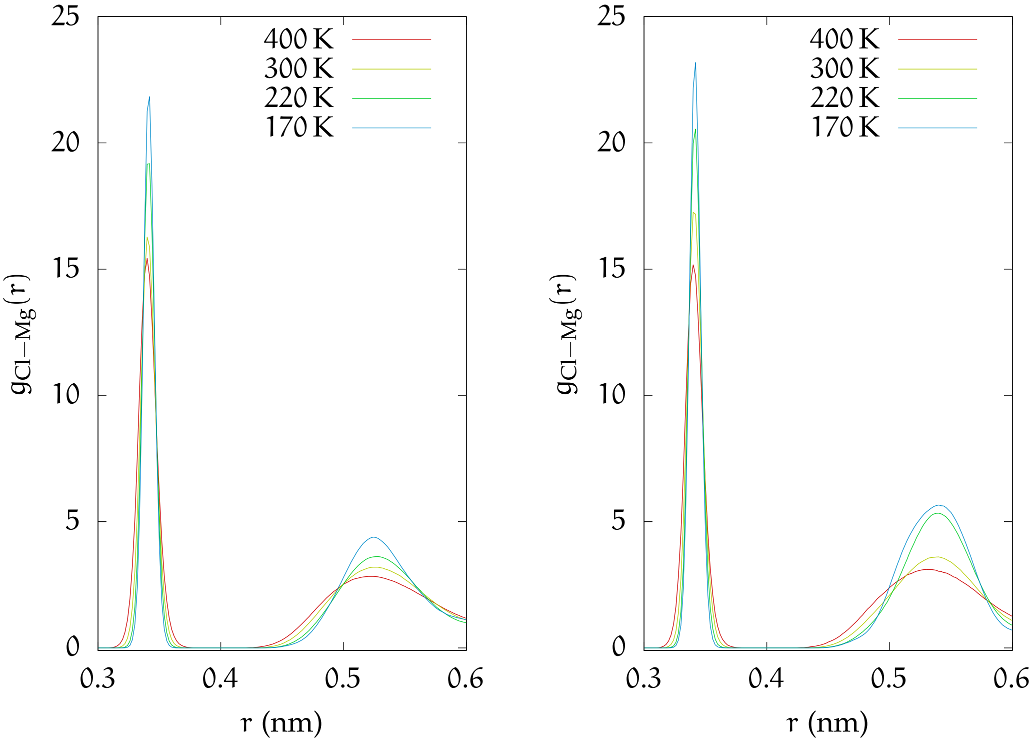

(a) $\rho = 1200\,kg/m^3$ (b) $\rho = 1040\,kg/m^3$

Figure 7.7: Ion Pairing Cl−Mg for the $C_2^{Mg(ClO_4)_2}$ solution.

7.3 COMPARISONS AND STRUCTURAL REMARKS

Water's anomalous behaviour persits.

The structural analysis, carried out through the examination of the Radial Distribution Functions (RDFs) as defined by equation (5.1) (Gallo and Rovere, 2021; Allen and Tildesley, 2017), has shown that in the solutions studied, water's anomalous behaviour persists despite significant alterations to the phase diagram caused by the ions. Investigating the water-water RDFs, as well as the ion-ion and ion-water RDFs, regions characterised by distinctly High-Density Liquid (HDL) and Low-Density Liquid (LDL) behaviours were observed.

The ion pairing behaviour confirmed the presence of LDL water at low densities and low temperatures

Specifically, analysing the ion-ion RDFs, the shifts from HDL to LDL were inferred by the behaviours of the $Cl-Na$ and $Cl-Mg$ ion pairings, which exhibited a significant rise in the first peak in response to a decrease in temperature. This phenomenon is attributed to the fact that water in the LDL phase is known for excluding ions, leading to a higher likelihood of them to approach each other. For sodium perchlorate, this effect was also distinctly observable when the density was lowered; in contrast, the impact of the density was much less apparent in magnesium perchlorate, due to the more intense electromagnetic interactions between the ions.

The water-water RDFs show the LDL region being less favoured upon increasing the concentration

In the water-water structural analysis, the $g_{O_w-O_W}(r)$ exhibited a gradual shift in trend from an HDL-like to an LDL-like behaviour, both by lowering the density and by lowering the temperature. Crucially, it should be emphasised that the LDL behaviours at the highest concentrations examined only manifested at low temperatures and densities and were, nonetheless, less pronounced than in the bulk. The C_1 solutions, instead, were consistently similar to the bulk, except at high densities and low temperatures where their LDL-like behaviour was less evident. This pattern was remarkably similar both in $NaClO_4$ and in $Mg(ClO_4)_2$ solutions.

The implication is that both in the case of sodium perchlorate and in the case of magnesium perchlorate, the LDL region is less favoured upon increasing the ionic concentration. This observation offers an insight into why water may retain its liquid form in the Martian subsurface at temperatures around 180 K, given that perchlorate solutions are ubiquitous on Mars (Orosei et al., 2018; Lauro et al., 2021) and that nucleation is more favoured in the LDL phase (Gallo et al., 2016).

Part IV

CONCLUSIONS

8

CONCLUSIONS

In light of the growing interest in perchlorate aqueous solutions for studying water behaviour on Mars, driven by recent experimental evidence strongly suggesting the presence of supercooled liquid water in these solutions beneath the Martian soil (Orosei et al., 2018; Lauro et al., 2021), it was crucial to examine their thermodynamic and structural features and the role of water anomalies in this context.

This thesis focused on solutions of sodium perchlorate ($NaClO_4$) and magnesium perchlorate ($Mg(ClO_4)_2$), as they are among the most abundant salts found on the Martian soil. In particular, a concentration-dependent study of these solutions was carried out in the canonical ensemble based on molecular dynamics (MD) simulations (Gallo and Rovere, 2021; Allen and Tildesley, 2017).

Two concentrations for each solute were considered:

- ${C_1}^{NaClO_4} = 1.63$ wt%;
- ${C_2}^{NaClO_4} = 15.4$ wt%;
- ${C_1}^{Mg(ClO_4)_2} = 2.95$ wt%;
- ${C_2}^{Mg(ClO_4)_2} = 24.4$ wt%.

The choice of the concentrations for $NaClO_4$ and $Mg\left(ClO_4\right)_2$ was made with the aim to achieve a comparable number fraction among magnesium and sodium perchlorate solutions (see Table 6.1 for more details).

The study of the phase diagram by the numerical calculation of the systems equation of state revealed the persistence of several water anomalies.

Specifically, the liquid-liquid critical point (LLCP) that was hypothesised in Poole et al., 1992, was found in the ${C_1}^{NaClO_4}$, the ${C_2}^{NaClO_4}$ and in the ${C_1}^{Mg(ClO_4)_2}$ solution. Compared to the bulk (as per Debenedetti et al., 2020), the LLCP in the ${C_1}^{NaClO_4}$ and the ${C_1}^{Mg(ClO_4)_2}$ solution was found to be at approximately the same temperature and slightly shifted downwards in pressure. In the ${C_2}^{NaClO_4}$ solution the LLCP was found at a slightly higher temperature and significantly lower pressure. Upon increasing the concentrations of the solutes, across all the systems considered, when a LLCP was found, ρ_C always shifted upwards in densities.

An important anomaly shared with bulk water that was found in all the solutions considered is the occurrence of maxima in the isothermal compressibility. This is extremely significant, as lines of maxima of thermodynamic response functions near the LLCP (or other second-order critical points) tend to converge towards the Widom Line. The Widom Line is an important precursor of the LLCP as it converges to it and then its extension into the two-phase region is the HDL-LDL coexistence line.

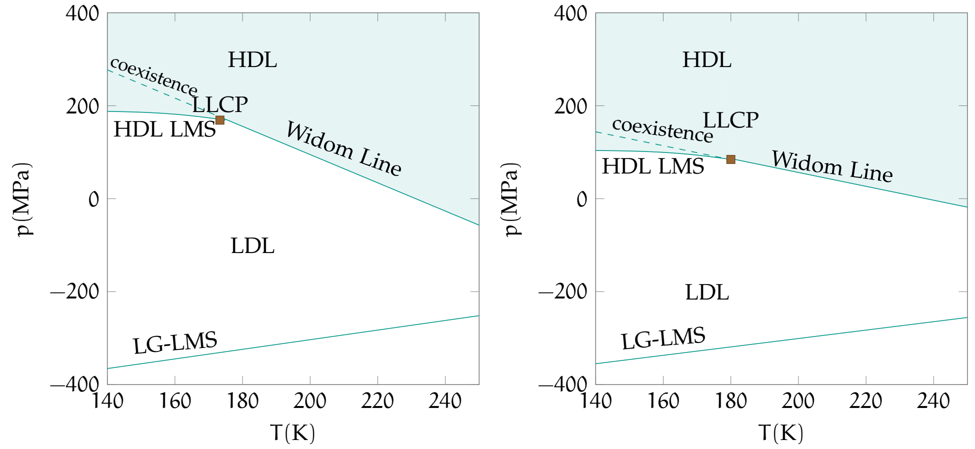

(a) $C_1{}^{NaClO_4} = 1.63\,\mathrm{wt\%}$

(b) $C_2{}^{NaClO_4} = 15.4\,\mathrm{wt\%}$

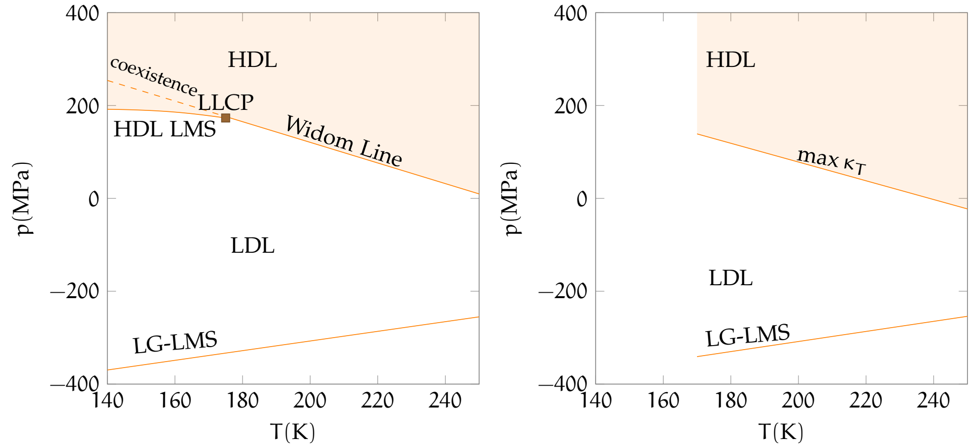

(c) $C_1{}^{Mg(ClO_4)_2} = 2.95\,\mathrm{wt\%}$

(d) $C_2{}^{Mg(ClO_4)_2} = 24.4\,\mathrm{wt\%}$

Figure 8.1: Schematic phase diagrams of the considered solutions, clearly showing the LDL region shrinking upon increasing the ionic concentrations. The positions of the HDL-LDL coexistence line and the HDL LMS here shown are hypothesised, as equilibration to eccessively low temperature is not possible in MD simulations (see Sec. 3.3.3). No state points were simulated below $T = 170\,\mathrm{K}$.

The existence of a line of maxima for isothermal compressibility in the $C_2^{Mg(ClO_4)_2}$ solution, marked by increasingly prominent peaks as the temperature drops down to the lowest temperature where equilibration with MD was possible, allows us to conclude that the presence of a second-order critical point at temperatures lower than those investigated cannot be dismissed. The significance of this is given by the fact that the presence of magnesium perchlorate far exceeds that of sodium perchlorate on Mars. A downward shift in temperature of the LLCP could be associated with a reduction in the glass transition temperature, potentially leading to a greater stabilisation of the supercooled phase of water. This could be a factor in explaining the detection of liquid water in the Martian subsurface at temperatures as low as 180 K.

Additionally, shifts towards lower temperatures and pressures in the TMD (Temperature of Maximum Density) and TmD (Temperature of Minimum Density) curves were observed. Notably, the shift in pressure was considerably more pronounced for sodium perchlorate compared to magnesium perchlorate.

These observed anomalies, along with a largely unchanged liquid-gas limit of mechanical stability (LG-LMS) result in a reduction of the LDL phase, where nucleation is more likely and, hence, in a consequently increased stabilisation of the supercooled phase of water.

Schematic phase diagrams highlighting this phenomenon along with the position of several thermodynamic quantities for the considered solutions are reported in Fig. 8.1.

The persistence of water anomalies is also evident from the water-water, water-ion and ion-ion radial distribution functions (RDFs). Specifically, ion pairing was found to be favoured by the reduction in density (mostly for $NaClO_4$) and temperature (for $NaClO_4$ and $Mg(ClO_4)_2$). Such a behaviour typically occurs in the LDL region, whilst the ions tend to be more favourably solvated in HDL water.

From the water-water RDFs also an interplay between the HDL and the LDL phases of water was observed.

The structural analysis of the systems under investigations further backed up the observation that water is less LDL upon increasing the concentration.

The water-water RDFs showed a shift from HDL to LDL behaviour at lower densities and temperatures. Notably, at high concentrations, LDL characteristics emerged only at very low temperatures and densities, being less pronounced than in bulk. The pattern was similar in $NaClO_4$ and $Mg(ClO_4)_2$ solutions.

A more stabilised supercooled phase of water is also evident from the Cl-Cl RDFs in which at low densities and temperatures in the case of magnesium perchlorate, that again is much more prevalent on Mars than sodium perchlorate, the occurrence of order is not observed.

Given the recent findings strongly indicating the presence of liquid water on Mars, it is important to have shown that water can retain its anomalies at moderate concentrations of typically Martian solutes. These anomalies could play a crucial role in explaining the existence of liquid water on Mars.

Further developments of this work have already been outlined, with the intent of extending the thermodynamic and structural study to other solutes and increasing concentrations. Calcium perchlorate and potassium perchlorate are also abundant on Mars and their behaviour in solution with water is worth investigating. Further studies are also crucial to better understand the behaviour of the critical point in these solutions.

Another line of research that is intended to be pursued is the development of further potentials, for instance by using machine learning techniques, with the aim of improving the comparability of results between different solutes and more easily extend the analysis to other perchlorates.

Part V

APPENDIX

A

PUBLICATIONS AND POSTERS

PUBLICATIONS

2023 Supercooled solutions of sodium perchlorate in TIP4P/2005 water: The effect of martian solutes on thermodynamics and structure

Authors: Paolo La Francesca, prof. Paola Gallo

Article

La Francesca and Gallo, 2023

We study the thermodynamic behaviour of sodium perchlorate solutions in supercooled water through molecular dynamics numerical simulations. These solutions are of special interest because of the recent experimental results that led to hypothesise the presence of liquid water in perchlorate solutions beneath the Martian soil. We model water using the TIP4P/2005 potential. The results we obtain for solutions with concentrations 1.63 wt% and 15.4 wt% are in agreement with those of a system undergoing a liquid-liquid phase transition where the liquid-liquid critical point shifts to slightly higher temperatures and lower pressures. The structure of the system is also analysed and we come to the conclusion that even at the highest concentration considered, water retains its anomalous behaviour.

The Journal of Chemical Physics, 159, 124501 (2023); doi: 10.1063/5.0168587

— Molecular Dynamics Computational Study of Magnesium Perchlorate in TIP4P/2005 water

Authors: Paolo La Francesca, prof. Paola Gallo,
In preparation.

Article

La Francesca and Gallo, 2024

POSTERS

2022 Aqueous Perchlorate Solutions: a Numerical Study

Presented at *CCP5 Summer School*.
Durham University, 19th of July 2022.
Authors: Paolo La Francesca, prof. Paola Gallo

Poster

2023 Molecular Dynamics Simulations of $NaClO_4$ in TIP4P/2005 water

Presented at *Frontiers in Water Biophysics*.
Centro Di Cultura Scientifica Ettore Majorana, Erice 19th-24th of May 2023.
Authors: Paolo La Francesca, prof. Paola Gallo

Poster

2023 Aqueous Perchlorate Solutions: a Numerical Study

Presented at *Roma Tre Congress on Water under Extreme Conditions*.
Università degli studi Roma Tre, 8th of June 2023.
Authors: Paolo La Francesca, prof. Paola Gallo

Poster

2023 Aqueous Perchlorate Solutions: a Numerical Study

Poster

Presented at *XXVII National Conference on Statistical Physics and Complex Systems and III Conference of the Italian Society of Statistical Physics*.
Università degli studi di Parma, 22nd-23rd of June 2023.
Authors: Paolo La Francesca, prof. Paola Gallo

2023 Molecular Dynamics Simulations of $NaClO_4$ in TIP4P/2005 water

Poster

Presented at CCP5 Annual General Meeting.
University of Warwick, 12th of September 2023.
Authors: Paolo La Francesca, prof. Paola Gallo

ORGANISATION OF MEETINGS

Local Organising Committee

Roma Tre Congress on Water under Extreme Conditions
Università degli studi Roma Tre, 7-9 June 2023

BIBLIOGRAPHY

BIBLIOGRAPHY

La Francesca, Paolo and Paola Gallo

2023 'Supercooled solutions of sodium perchlorate in TIP4P/2005 water: The effect of martian solutes on thermodynamics and structure', *The Journal of Chemical Physics*, 159, 12 [Sept. 2023], p. 124501, ISSN: 0021-9606, DOI: 10.1063/5.0168587, eprint: https://pubs.aip.org/aip/jcp/article-pdf/doi/10.1063/5.0168587/18136708/124501_1_5.0168587.pdf, https://doi.org/10.1063/5.0168587.

2024 In preparation.

Gallo, Paola, Katrin Amann-Winkel, Charles Austen Angell, Mikhail Alexeevich Anisimov, Frédéric Caupin, Charusita Chakravarty, Erik Lascaris, Thomas Loerting, Athanassios Zois Panagiotopoulos, John Russo, Jonas Alexander Sellberg, Harry Eugene Stanley, Hajime Tanaka, Carlos Vega, Limei Xu and Lars Gunnar Moody Pettersson

2016 'Water: A Tale of Two Liquids', *Chemical Reviews*, 116, 13, PMID: 27380438, pp. 7463–7500, DOI: 10.1021/acs.chemrev.5b00750, eprint: https://doi.org/10.1021/acs.chemrev.5b00750, https://doi.org/10.1021/acs.chemrev.5b00750.

Gallo, Paola and H. Eugene Stanley

2017 'Supercooled water reveals its secrets', *Science*, 358, 6370, pp. 1543–1544, DOI: 10.1126/science.aar3575, eprint: https://www.science.org/doi/pdf/10.1126/science.aar3575, https://www.science.org/doi/abs/10.1126/science.aar3575.

Angell, C A

1983 'Supercooled Water', *Annual Review of Physical Chemistry*, 34, 1, pp. 593–630, DOI: 10.1146/annurev.pc.34.100183.003113, eprint: https://doi.org/10.1146/annurev.pc.34.100183.003113, https://doi.org/10.1146/annurev.pc.34.100183.003113.

Debenedetti, Pablo G

2003 'Supercooled and glassy water', *Journal of Physics: Condensed Matter*, 15, 45 [Oct. 2003], R1669–R1726, DOI: 10.1088/0953-8984/15/45/r01, https://doi.org/10.1088/0953-8984/15/45/r01.

Gallo, Paola and Mauro Rovere

2021 *Physics of Liquid Matter*, Soft and Biological Matter, Springer International Publishing, ISBN: 9783030683498, https://books.google.it/books?id=aT83EAAAQBAJ.

Parisi, Giorgio

1998 *Statistical Field Theory*, Avalon Publishing, ISBN: 9780738200514, https://books.google.it/books?id=bivTswEACAAJ.

Debenedetti, P.G.

1996 *Metastable Liquids: Concepts and Principles*, Physical Chemistry: Science and Engineering, Princeton University Press, ISBN: 9780691085951, https://books.google.it/books?id=tzvvsltE6Y8C.

Parisi, Giorgio

1989 'Transizioni di fase', in, *Treccani - Enciclopedia del Novecento, Supplemento I.*

1992 'Slow dynamics of glassy systems', in *Complex Behaviour of Glassy Systems*, Springer Berlin Heidelberg, pp. 111–121, DOI: 10.1007/bfb0104821, https://doi.org/10.1007%2Fbfb0104821.

Mishima, Osamu

1996 'Relationship between melting and amorphization of ice', *Nature*, 384, 6609, pp. 546–549.

Kanno, H, RJ Speedy and CA Angell

1975 'Supercooling of water to-92 C under pressure', *Science*, 189, 4206, pp. 880–881.

Tombari, E, C Ferrari, G Salvetti and GP Johari

1999 'Water-ice transformation in micron-size droplets in emulsions', *The Journal of chemical physics*, 111, 7, pp. 3115–3120.

Krämer, B, O Hübner, H Vortisch, L Wöste, T Leisner, M Schwell, E Rühl and H Baumgärtel

1999 'Homogeneous nucleation rates of supercooled water measured in single levitated microdroplets', *The Journal of Chemical Physics*, 111, 14, pp. 6521–6527.

Krämer, B, M Schwell, O Hübner, H Vortisch, T Leisner, E Rühl, H Baumgärtel and L Wöste

1996 'Homogeneous ice nucleation observed in single levitated micro droplets', *Berichte der Bunsengesellschaft für physikalische Chemie*, 100, 11, pp. 1911–1914.

Kim, Kyung Hwan, Alexander Späh, Harshad Pathak, Fivos Perakis, Daniel Mariedahl, Katrin Amann-Winkel, Jonas A Sellberg, Jae Hyuk Lee, Sangsoo Kim, Jaehyun Park et al.

2017 'Maxima in the thermodynamic response and correlation functions of deeply supercooled water', *Science*, 358, 6370, pp. 1589–1593.

Kim, Kyung Hwan, Katrin Amann-Winkel, Nicolas Giovambattista, Alexander Späh, Fivos Perakis, Harshad Pathak, Marjorie Ladd Parada, Cheolhee Yang, Daniel Mariedahl, Tobias Eklund, Thomas. J. Lane, Seonju You, Sangmin Jeong, Matthew Weston, Jae Hyuk Lee, Intae Eom, Minseok Kim, Jaeku Park, Sae Hwan Chun, Peter H. Poole and Anders Nilsson

2020 'Experimental observation of the liquid-liquid transition in bulk supercooled water under pressure', *Science*, 370, 6519, pp. 978–982, DOI: `10.1126/science.abb9385`, eprint: `https://www.science.org/doi/pdf/10.1126/science.abb9385`, `https://www.science.org/doi/abs/10.1126/science.abb9385`.

Seidl, Markus, Alice Fayter, Josef N Stern, Gerhard Zifferer and Thomas Loerting

2015 'Shrinking water's no man's land by lifting its low-temperature boundary', *Physical Review B*, 91, 14, p. 144201.

Speedy, Robin J, Pablo G Debenedetti, R Scott Smith, Chen Huang and Bruce D Kay

1996 'The evaporation rate, free energy, and entropy of amorphous water at 150 K', *The Journal of chemical physics*, 105, 1, pp. 240–244.

Allen, M.P. and D.J. Tildesley

2017 *Computer Simulation of Liquids*, Oxford science publications, Oxford University Press, ISBN: 9780198803195, `https://books.google.it/books?id=nlExDwAAQBAJ`.

Poole, Peter H., Francesco Sciortino, Ulrich Essmann and H. Eugene Stanley

1992 'Phase behaviour of metastable water', *Nature*, 360, pp. 324–328, DOI: `https://doi.org/10.1038/360324a0`.

Stillinger, Frank H and Aneesur Rahman

1974 'Improved simulation of liquid water by molecular dynamics', *The Journal of Chemical Physics*, 60, 4, pp. 1545–1557.

Palmer, Jeremy C, Fausto Martelli, Yang Liu, Roberto Car, Athanassios Z Panagiotopoulos and Pablo G Debenedetti

2014 'Metastable liquid–liquid transition in a molecular model of water', *Nature*, 510, 7505, pp. 385–388.

Liu, Yang, Jeremy C Palmer, Athanassios Z Panagiotopoulos and Pablo G Debenedetti

2012 'Liquid-liquid transition in ST2 water', *The Journal of chemical physics*, 137, 21, p. 214505.

Liu, Yang, Athanassios Z Panagiotopoulos and Pablo G Debenedetti

2009 'Low-temperature fluid-phase behavior of ST2 water', *The Journal of Chemical Physics*, 131, 10, p. 104508.

Sciortino, Francesco, Ivan Saika-Voivod and Peter H. Poole

2011 'Study of the ST2 model of water close to the liquid–liquid critical point', *Phys. Chem. Chem. Phys.*, 13 [44 2011], pp. 19759–19764, DOI: 10.1039/C1CP22316J, http://dx.doi.org/10.1039/C1CP22316J.

Kesselring, Tobias A, Erik Lascaris, Giancarlo Franzese, Sergey V Buldyrev, Hans J Herrmann and H Eugene Stanley

2013 'Finite-size scaling investigation of the liquid-liquid critical point in ST2 water and its stability with respect to crystallization', *The Journal of Chemical Physics*, 138, 24, p. 244506.

Smallenburg, Frank and Francesco Sciortino

2015 'Tuning the Liquid-Liquid Transition by Modulating the Hydrogen-Bond Angular Flexibility in a Model for Water', *Phys. Rev. Lett.*, 115 [1 July 2015], p. 015701, DOI: 10.1103/PhysRevLett.115.015701, https://link.aps.org/doi/10.1103/PhysRevLett.115.015701.

Gallo, Paola and Francesco Sciortino

2012 'Ising universality class for the liquid-liquid critical point of a one component fluid: A finite-size scaling test', *Physical review letters*, 109, 17, p. 177801.

Jagla, E. A.

2001 'Low-temperature behavior of core-softened models: Water and silica behavior', *Phys. Rev. E*, 63 [6 May 2001], p. 061509, DOI: 10.1103/PhysRevE.63.061509, https://link.aps.org/doi/10.1103/PhysRevE.63.061509.

Abascal, Jose LF and Carlos Vega

2005 'A general purpose model for the condensed phases of water: TIP4P/2005', *The Journal of chemical physics*, 123, 23, p. 234505.

Abascal, JLF, E Sanz, R García Fernández and C Vega

2005 'A potential model for the study of ices and amorphous water: TIP4P/Ice', *The Journal of chemical physics*, 122, 23.

Debenedetti, Pablo, Francesco Sciortino and Gül Zerze

2020 'Second critical point in two realistic models of water', *Science*, 369, 6501, pp. 289–292, DOI: 10.1126/science.abb9796, eprint: https://www.science.org/doi/pdf/10.1126/science.abb9796, https://www.science.org/doi/abs/10.1126/science.abb9796.

Mishima, Osamu and H Eugene Stanley

1998a 'Decompression-induced melting of ice IV and the liquid–liquid transition in water', *Nature*, 392, 6672, pp. 164–168.

Woutersen, Sander, Bernd Ensing, Michiel Hilbers, Zuofeng Zhao and C Austen Angell

2018 'A liquid-liquid transition in supercooled aqueous solution related to the HDA-LDA transition', *Science*, 359, 6380, pp. 1127–1131.

Winkel, Katrin, Erwin Mayer and Thomas Loerting

2011 'Equilibrated high-density amorphous ice and its first-order transition to the low-density form', *The Journal of Physical Chemistry B*, 115, 48, pp. 14141–14148.

Corradini, Dario, Mauro Rovere and Paola Gallo

2010 'A route to explain water anomalies from results on an aqueous solution of salt', *The Journal of chemical physics*, 132 [Apr. 2010], p. 134508, DOI: `10.1063/1.3376776`.

Corradini, Dario, Zhiqiang Su, H Eugene Stanley and Paola Gallo

2012 'A molecular dynamics study of the equation of state and the structure of supercooled aqueous solutions of methanol', *The Journal of chemical physics*, 137, 18, p. 184503.

Corradini, Dario, Mauro Rovere and Paola Gallo

2011 'Structural properties of high and low density water in a supercooled aqueous solution of salt', *The Journal of Physical Chemistry B*, 115, 6, pp. 1461–1468.

Orosei, R., S. E. Lauro, E. Pettinelli, A. Cicchetti, M. Coradini, B. Cosciotti, F. Di Paolo, E. Flamini, E. Mattei, M. Pajola, F. Soldovieri, M. Cartacci, F. Cassenti, A. Frigeri, S. Giuppi, R. Martufi, A. Masdea, G. Mitri, C. Nenna, R. Noschese, M. Restano and R. Seu

2018 'Radar evidence of subglacial liquid water on Mars', *Science*, 361, 6401, pp. 490–493, DOI: `10.1126/science.aar7268`, eprint: `https://www.science.org/doi/pdf/10.1126/science.aar7268`, `https://www.science.org/doi/abs/10.1126/science.aar7268`.

Lauro, Sebastian Emanuel, Elena Pettinelli, Graziella Caprarelli, Luca Guallini, Angelo Pio Rossi, Elisabetta Mattei, Barbara Cosciotti, Andrea Cicchetti, Francesco Soldovieri, Marco Cartacci, Federico Di Paolo, Raffaella Noschese and Roberto Orosei

2021 'Multiple subglacial water bodies below the south pole of Mars unveiled by new MARSIS data', *Nature Astronomy*, 5, pp. 63–70, DOI: `10.1038/s41550-020-1200-6`.

Toner, J.D., D.C. Catling and B. Light

2014 'The formation of supercooled brines, viscous liquids, and low-temperature perchlorate glasses in aqueous solutions relevant to Mars', *Icarus*, 233, pp. 36–47, ISSN: 0019-1035, DOI: `https://doi.org/10.1016/j.icarus.2014.01.018`, `https://www.sciencedirect.com/science/article/pii/S0019103514000499`.

Hess, Berk, Carsten Kutzner, David Van Der Spoel and Erik Lindahl

2008 'GROMACS 4: algorithms for highly efficient, load-balanced, and scalable molecular simulation', *Journal of chemical theory and computation*, 4, 3, pp. 435–447.

GRID-Roma Tre cluster

n.d. https://web-cluster.fis.uniroma3.it/, Accessed: 2023-01-16.

Nieszporek, Krzysztof, Jolanta Nieszporek and Magdalena Trojak

2016 'Calculations of shear viscosity, electric conductivity and diffusion coefficients of aqueous sodium perchlorate solutions from molecular dynamics simulations', *Computational and Theoretical Chemistry*, 1090, pp. 52–57.

Agieienko, Vira N., Yaroslav V. Kolesnik and Oleg N. Kalugin

2014 'Structure, solvation, and dynamics of Mg2+, Ca2+, Sr2+, and Ba2+ complexes with 3-hydroxyflavone and perchlorate anion in acetonitrile medium: A molecular dynamics simulation study', *The Journal of Chemical Physics*, 140, 19 [May 2014], p. 194501, ISSN: 0021-9606, DOI: 10.1063/1.4875591, eprint: https://pubs.aip.org/aip/jcp/article-pdf/doi/10.1063/1.4875591/9543311/194501_1_online.pdf, https://doi.org/10.1063/1.4875591.

Williams, Thomas and Colin et al. Kelley

2023 *Gnuplot 5.4.10: an interactive plotting program*, http://gnuplot.sourceforge.net/.

Humphrey, William, Andrew Dalke and Klaus Schulten

1996 'VMD: Visual molecular dynamics', *Journal of Molecular Graphics*, 14, 1, pp. 33–38, ISSN: 0263-7855, DOI: https://doi.org/10.1016/0263-7855(96)00018-5, https://www.sciencedirect.com/science/article/pii/0263785596000185.

Császár, Attila G, Gábor Czakó, Tibor Furtenbacher, Jonathan Tennyson, Viktor Szalay, Sergei V Shirin, Nikolai F Zobov and Oleg L Polyansky

2005 'On equilibrium structures of the water molecule', *The Journal of chemical physics*, 122, 21.

Hasted, JB

1972 'Liquid water: Dielectric properties', in *The Physics and Physical Chemistry of Water*, Springer, pp. 255–309.

Martin, F and Hendrik Zipse

2005 'Charge distribution in the water molecule—A comparison of methods', *Journal of computational chemistry*, 26, 1, pp. 97–105.

Bachler, Johannes, Philip H Handle, Nicolas Giovambattista and Thomas Loerting

2019 'Glass polymorphism and liquid–liquid phase transition in aqueous solutions: experiments and computer simulations', *Physical Chemistry Chemical Physics*, 21, 42, pp. 23238–23268.

Chaplin, Martin

2022 *Water Structure and Science*, https://water.lsbu.ac.uk/water/water_anomalies.html.

Petrenko, Victor F and Robert W Whitworth

1999 *Physics of ice*, OUP Oxford.

Salzmann, Christoph G, Paolo G Radaelli, Erwin Mayer and John L Finney

2009 'Ice XV: A new thermodynamically stable phase of ice', *Physical review letters*, 103, 10, p. 105701.

Cavagna, Andrea

2009 'Supercooled liquids for pedestrians', *Physics Reports*, 476, 4-6, pp. 51–124.

Debenedetti, Pablo G. and H. Eugene Stanley

2003 'Supercooled and Glassy Water', *Physics Today*, 56, 6 [June 2003], pp. 40–46, ISSN: 0031-9228, DOI: `10.1063/1.1595053`, eprint: `https://pubs.aip.org/physicstoday/article-pdf/56/6/40/11298569/40\_1\_online.pdf`, `https://doi.org/10.1063/1.1595053`.

Mishima, Osamu and H Eugene Stanley

1998b 'The relationship between liquid, supercooled and glassy water', *Nature*, 396, 6709, pp. 329–335.

Angell, CA

2002 'Liquid fragility and the glass transition in water and aqueous solutions', *Chemical reviews*, 102, 8, pp. 2627–2650.

Loerting, Thomas, Christoph Salzmann, Ingrid Kohl, Erwin Mayer and Andreas Hallbrucker

2001 'A second distinct structural "state" of high-density amorphous ice at 77 K and 1 bar', *Physical Chemistry Chemical Physics*, 3, 24, pp. 5355–5357.

Mishima, O, LD Calvert and E Whalley

1985 'An apparently first-order transition between two amorphous phases of ice induced by pressure', *Nature*, 314, 6006, pp. 76–78.

Winkel, Katrin, Michael S Elsaesser, Erwin Mayer and Thomas Loerting

2008 'Water polyamorphism: Reversibility and (dis) continuity', *The Journal of chemical physics*, 128, 4.

Angell, CA and H Kanno

1976 'Density maxima in high-pressure supercooled water and liquid silicon dioxide', *Science*, 193, 4258, pp. 1121–1122.

Liu, Dazhi, Yang Zhang, Chia-Cheng Chen, Chung-Yuan Mou, Peter H Poole and Sow-Hsin Chen

2007 'Observation of the density minimum in deeply supercooled confined water', *Proceedings of the National Academy of Sciences*, 104, 23, pp. 9570–9574.

Mallamace, Francesco, Caterina Branca, Matteo Broccio, Carmelo Corsaro, Chung-Yuan Mou and Sow-Hsin Chen

2007 'The anomalous behavior of the density of water in the range 30 K< T< 373 K', *Proceedings of the National Academy of Sciences*, 104, 47, pp. 18387–18391.

Gallo, P, M Rovere and S-H Chen

2010 'Dynamic crossover in supercooled confined water: Understanding bulk properties through confinement', *The Journal of Physical Chemistry Letters*, 1, 4, pp. 729–733.

Gallo, P., M. Rovere and E. Spohr

2000a 'Supercooled Confined Water and the Mode Coupling Crossover Temperature', *Phys. Rev. Lett.*, 85 [20 Sept. 2000], pp. 4317–4320, DOI: `10.1103/PhysRevLett.85.4317`, `https://link.aps.org/doi/10.1103/PhysRevLett.85.4317`.

2000b 'Glass transition and layering effects in confined water: A computer simulation study', *The Journal of Chemical Physics*, 113, 24 [Dec. 2000], pp. 11324–11335, ISSN: 0021-9606, DOI: `10.1063/1.1328073`, eprint: `https://pubs.aip.org/aip/jcp/article-pdf/113/24/11324/10829009/11324\_1\_online.pdf`, `https://doi.org/10.1063/1.1328073`.

Paschek, Dietmar

2005 'How the liquid-liquid transition affects hydrophobic hydration in deeply supercooled water', *Physical review letters*, 94, 21, p. 217802.

Landau, L.D. and E.M. Lifshitz

1958 *Statistical Physics: Volume 5*, v. 5, Elsevier Science, ISBN: 9780080570464, `https://books.google.it/books?id=VzgJN-XPTRsC`.

Errington, Jeffrey R and Pablo G Debenedetti

2001 'Relationship between structural order and the anomalies of liquid water', *Nature*, 409, 6818, pp. 318–321.

Speedy, RJ and CA Angell

1976 'Isothermal compressibility of supercooled water and evidence for a thermodynamic singularity at- 45 C', *The Journal of Chemical Physics*, 65, 3, pp. 851–858.

Xu, Limei, Sergey V Buldyrev, C Austen Angell and H Eugene Stanley

2006 'Thermodynamics and dynamics of the two-scale spherically symmetric Jagla ramp model of anomalous liquids', *Physical Review E*, 74, 3, p. 031108.

De Oliveira, Alan Barros, Giancarlo Franzese, Paulo A Netz and Marcia C Barbosa

2008 'Waterlike hierarchy of anomalies in a continuous spherical shouldered potential', *The Journal of Chemical Physics*, 128, 6.

Yan, Zhenyu, Sergey V Buldyrev, Pradeep Kumar, Nicolas Giovambattista, Pablo G Debenedetti and H Eugene Stanley

2007 'Structure of the first-and second-neighbor shells of simulated water: Quantitative relation to translational and orientational order', *Physical Review E*, 76, 5, p. 051201.

Nilsson, Anders and Lars GM Pettersson

2015 'The structural origin of anomalous properties of liquid water', *Nature communications*, 6, 1, p. 8998.

Xu, Limei, Pradeep Kumar, Sergey V Buldyrev, S-H Chen, Peter H Poole, Francesco Sciortino and H Eugene Stanley

2005 'Relation between the Widom line and the dynamic crossover in systems with a liquid–liquid phase transition', *Proceedings of the National Academy of Sciences*, 102, 46, pp. 16558–16562, DOI: `10.1073/pnas.0507870102`, eprint: `https://www.pnas.org/content/102/46/16558.full.pdf`.

Franzese, Giancarlo and H Eugene Stanley

2007 'The Widom line of supercooled water', *Journal of Physics: Condensed Matter*, 19, 20, p. 205126.

Anisimov, Mikhail A, Jan V Sengers and Johanna MH Levelt Sengers

2004 'Near-critical behavior of aqueous systems', in *Aqueous Systems at Elevated Temperatures and Pressures*, Elsevier, pp. 29–71.

Gallo, P, D Corradini and M Rovere

2014 'Widom line and dynamical crossovers as routes to understand supercritical water', *Nature communications*, 5, 1, p. 5806.

Ito, Kaori, Cornelius T Moynihan and C Austen Angell

1999 'Thermodynamic determination of fragility in liquids and a fragile-to-strong liquid transition in water', *Nature*, 398, 6727, pp. 492–495.

Nilsson, Anders

2022 'Origin of the anomalous properties in supercooled water based on experimental probing inside "no-man's land"', *Journal of Non-Crystalline Solids: X*, 14, p. 100095.

Soper, Alan K. and Maria Antonietta Ricci

2000 'Structures of High-Density and Low-Density Water', *Phys. Rev. Lett.*, 84 [13 Mar. 2000], pp. 2881–2884, DOI: `10.1103/PhysRevLett.84.2881`, `https://link.aps.org/doi/10.1103/PhysRevLett.84.2881`.

Banerjee, D, SN Bhat, SV Bhat and Dino Leporini

2009 'ESR evidence for 2 coexisting liquid phases in deeply supercooled bulk water', *Proceedings of the National Academy of Sciences*, 106, 28, pp. 11448–11453.

Liu, Li, Sow-Hsin Chen, Antonio Faraone, Chun-Wan Yen and Chung-Yuan Mou

2005 'Pressure Dependence of Fragile-to-Strong Transition and a Possible Second Critical Point in Supercooled Confined Water', *Physical review letters*, 95 [Oct. 2005], p. 117802, DOI: `10.1103/PhysRevLett.95.117802`.

Liu, Li, Sow-Hsin Chen, Antonio Faraone, Chun-Wan Yen, Chung-Yuan Mou, Alexander I Kolesnikov, Eugene Mamontov and Juscelino Leao

2006 'Quasielastic and inelastic neutron scattering investigation of fragile-to-strong crossover in deeply supercooled water confined in nanoporous silica matrices', *Journal of Physics: Condensed Matter*, 18, 36, S2261.

Zhang, Yang, Antonio Faraone, William A. Kamitakahara, Kao-Hsiang Liu, Chung-Yuan Mou, Juscelino B. Leão, Sung Chang and Sow-Hsin Chen

2011a *Unusual Phase Behavior of Confined Heavy Water*, arXiv: `1005.5387 [cond-mat.soft]`.

Harrington, Stephen, Peter H Poole, Francesco Sciortino and H Eugene Stanley

1997 'Equation of state of supercooled water simulated using the extended simple point charge intermolecular potential', *The Journal of chemical physics*, 107, 18, pp. 7443–7450.

Poole, Peter H, Francesco Sciortino, Ulrich Essmann and H Eugene Stanley

1993 'Spinodal of liquid water', *Physical Review E*, 48, 5, p. 3799.

Sciortino, Francesco, Peter H Poole, Ulrich Essmann and HE Stanley

1997 'Line of compressibility maxima in the phase diagram of supercooled water', *Physical Review E*, 55, 1, p. 727.

Tanaka, Hideki

1996 'Phase behaviors of supercooled water: Reconciling a critical point of amorphous ices with spinodal instability', *The Journal of chemical physics*, 105, 12, pp. 5099–5111.

Kumar, Pradeep, Sergey V Buldyrev, Francis W Starr, Nicolas Giovambattista and H Eugene Stanley

2005 'Thermodynamics, structure, and dynamics of water confined between hydrophobic plates', *Physical Review E*, 72, 5, p. 051503.

Yamada, Masako, Stefano Mossa, H. Eugene Stanley and Francesco Sciortino

2002 'Interplay between Time-Temperature Transformation and the Liquid-Liquid Phase Transition in Water', *Phys. Rev. Lett.*, 88 [19 Apr. 2002], p. 195701, DOI: `10.1103/PhysRevLett.88.195701`, `https://link.aps.org/doi/10.1103/PhysRevLett.88.195701`.

Paschek, Dietmar, Andreas Rüppert and Alfons Geiger

2008 'Thermodynamic and Structural Characterization of the Transformation from a Metastable Low-Density to a Very High-Density Form of Supercooled TIP4P-Ew Model Water', *ChemPhysChem*, 9, 18, pp. 2737–2741.

Jedlovszky, Pál and Renzo Vallauri

2005 'Liquid–vapor and liquid–liquid phase equilibria of the Brodholt–Sampoli–Vallauri polarizable water model', *The Journal of chemical physics*, 122, 8.

Gartner III, Thomas E, Linfeng Zhang, Pablo M Piaggi, Roberto Car, Athanassios Z Panagiotopoulos and Pablo G Debenedetti

2020 'Signatures of a liquid–liquid transition in an ab initio deep neural network model for water', *Proceedings of the National Academy of Sciences*, 117, 42, pp. 26040–26046.

Sastry, Srikanth, Pablo G. Debenedetti, Francesco Sciortino and H. E. Stanley

1996 'Singularity-free interpretation of the thermodynamics of supercooled water', *Physical Review E*, 53, 6 [June 1996], pp. 6144–6154, ISSN: 1095-3787, DOI: `10.1103/physreve.53.6144`, `http://dx.doi.org/10.1103/PhysRevE.53.6144`.

Rebelo, Luis Paulo N., Pablo G. Debenedetti and Srikanth Sastry

1998 'Singularity-free interpretation of the thermodynamics of supercooled water. II. Thermal and volumetric behavior', *The Journal of Chemical Physics*, 109, 2 [July 1998], pp. 626–633, ISSN: 1089-7690, DOI: `10.1063/1.476600`, `http://dx.doi.org/10.1063/1.476600`.

Angell, C. Austen

2008 'Insights into Phases of Liquid Water from Study of Its Unusual Glass-Forming Properties', *Science*, 319, 5863 [Feb. 2008], pp. 582–587, ISSN: 1095-9203, DOI: `10.1126/science.1131939`, `http://dx.doi.org/10.1126/science.1131939`.

Miyata, K, H Kanno, T Niino and K Tomizawa

2002 'Cationic and anionic effects on the homogeneous nucleation of ice in aqueous alkali halide solutions', *Chemical physics letters*, 354, 1-2, pp. 51–55.

Souda, Ryutaro

2006 'Liquid-liquid transition in supercooled water investigated by interaction with LiCl and Xe', *The Journal of chemical physics*, 125, 18.

Mishima, Osamu

2007 'Phase separation in dilute LiCl–H2O solution related to the polyamorphism of liquid water', *The Journal of chemical physics*, 126, 24.

Archer, Donald G. and Richard W. Carter

2000 'Thermodynamic Properties of the NaCl + H2O System. 4. Heat Capacities of H2O and NaCl(aq) in Cold-Stable and Supercooled States', *The Journal of Physical Chemistry B*, 104, 35, pp. 8563–8584, DOI: `10.1021/jp0003914`, eprint: `https://doi.org/10.1021/jp0003914`, `https://doi.org/10.1021/jp0003914`.

Carter, Richard W and Donald G Archer

2000 'Heat capacity of NaNO 3 (aq) in stable and supercooled states. Ion association in the supercooled solution', *Physical Chemistry Chemical Physics*, 2, 22, pp. 5138–5145.

Corradini, Dario and Paola Gallo

2011 'Liquid–liquid coexistence in NaCl aqueous solutions: a simulation study of concentration effects', *The Journal of Physical Chemistry B*, 115, 48, pp. 14161–14166.

Perin, Leonardo and Paola Gallo

2023 'Phase Diagram of Aqueous Solutions of LiCl: a Study of Concentration Effects on the Anomalies of Water', *The Journal of Physical Chemistry B*, 127, 20, PMID: 37167579, pp. 4613–4622, DOI: `10.1021/acs.jpcb.3c00703`, eprint: `https://doi.org/10.1021/acs.jpcb.3c00703`, `https://doi.org/10.1021/acs.jpcb.3c00703`.

Mishima, Osamu

2005 'Application of polyamorphism in water to spontaneous crystallization of emulsified LiCl-H2O solution', *The Journal of chemical physics*, 123, 15.

Ruiz, GN, LIVIA ELEONORA Bove, Horacio Roberto Corti and T Loerting

2014 'Pressure-induced transformations in LiCl–H 2 O at 77 K', *Physical Chemistry Chemical Physics*, 16, 34, pp. 18553–18562.

Le, Ly and Valeria Molinero

2011 'Nanophase segregation in supercooled aqueous solutions and their glasses driven by the polyamorphism of water', *The Journal of Physical Chemistry A*, 115, 23, pp. 5900–5907.

Hribar, Barbara, Noel T Southall, Vojko Vlachy and Ken A Dill

2002 'How ions affect the structure of water', *Journal of the American Chemical Society*, 124, 41, pp. 12302–12311.

Gallo, Paola, Dario Corradini and Mauro Rovere

2011 'Ion hydration and structural properties of water in aqueous solutions at normal and supercooled conditions: a test of the structure making and breaking concept', *Physical Chemistry Chemical Physics*, 13, 44, pp. 19814–19822.

Smith, Jared D, Richard J Saykally and Phillip L Geissler

2007 'The effects of dissolved halide anions on hydrogen bonding in liquid water', *Journal of the American Chemical Society*, 129, 45, pp. 13847–13856.

Soper, Alan K and Kristian Weckström

2006 'Ion solvation and water structure in potassium halide aqueous solutions', *Biophysical chemistry*, 124, 3, pp. 180–191.

Franks, Felix

2000 *Water: a matrix of life*, Royal Society of Chemistry, vol. 21.

Chevrier, Vincent F, Jennifer Hanley and Travis S Altheide

2009 'Stability of perchlorate hydrates and their liquid solutions at the Phoenix landing site, Mars', *Geophysical Research Letters*, 36, 10.

Laurent, Harrison, Alan K. Soper and Lorna Dougan

2020 'Trimethylamine N-oxide (TMAO) resists the compression of water structure by magnesium perchlorate: terrestrial kosmotrope vs. Martian chaotrope', *Phys. Chem. Chem. Phys.*, 22 [9 2020], pp. 4924–4937, DOI: `10.1039/C9CP06324B`, `http://dx.doi.org/10.1039/C9CP06324B`.

Laurent, Harrison, Alan Soper and Lorna Dougan

2019 'Biomolecular self-assembly under extreme Martian mimetic conditions', *Molecular Physics*, 117, 22, pp. 3398–3407, DOI: `10.1080/00268976.2019.1649485`, eprint: `https://doi.org/10.1080/00268976.2019.1649485`, `https://doi.org/10.1080/00268976.2019.1649485`.

Lenton, Samuel, Natasha H Rhys, James J Towey, Alan K Soper and Lorna Dougan

2017 'Highly compressed water structure observed in a perchlorate aqueous solution', *Nature communications*, 8, 1, p. 919.

Calvagna, Chiara, Andrea Lapini, Andrea Taschin, Samuele Fanetti, Marco Pagliai, Paolo Bartolini, Roberto Bini, Roberto Righini and Renato Torre

2021 'Modification of local and collective dynamics of water in perchlorate solution, induced by pressure and concentration', *Journal of Molecular Liquids*, 337, p. 116273, ISSN: 0167-7322, DOI: `https://doi.org/10.1016/j.molliq.2021.116273`, `https://www.sciencedirect.com/science/article/pii/S0167732221009971`.

Goldstein, H.

2002 *Classical Mechanics*, Pearson Education, ISBN: 9788177582833, `https://books.google.it/books?id=Spy6xHWFJIEC`.

Arnold, V.I., K. Vogtmann and A. Weinstein

1989 *Mathematical Methods of Classical Mechanics*, Graduate texts in mathematics, Springer, ISBN: 9783540968900, https://books.google.it/books?id=cJ3BQgAACAAJ.

Huang, K.

1987 *Statistical Mechanics*, Wiley, ISBN: 9780471815181, https://books.google.it/books?id=M8PvAAAAMAAJ.

Gallavotti, G.

2014 *Statistical Mechanics: A Short Treatise*, Theoretical and Mathematical Physics, Springer Berlin Heidelberg, ISBN: 9783662039533, https://books.google.it/books?id=IF0hswEACAAJ.

Cencini, M., F. Cecconi and A. Vulpiani

2010 *Chaos: From Simple Models to Complex Systems*, Series on advances in statistical mechanics, World Scientific, ISBN: 9789814277655, https://books.google.it/books?id=YTepwrrU4a0C.

Barone, L.M., E. Marinari, G. Organtini and F. Ricci-Tersenghi

2013 *Scientific Programming: C-language, Algorithms and Models in Science*, G - Reference,Information and Interdisciplinary Subjects Series, World Scientific, ISBN: 9789814513401, https://books.google.it/books?id=mh2kngEACAAJ.

Verlet, Loup

1967 'Computer "Experiments" on Classical Fluids. I. Thermodynamical Properties of Lennard-Jones Molecules', *Phys. Rev.*, 159 [1 July 1967], pp. 98–103, DOI: 10.1103/PhysRev.159.98, https://link.aps.org/doi/10.1103/PhysRev.159.98.

Hockney, R W

1970 'The potential calculation and some applications.' *Methods Comput. Phys.*, 9 [Jan. 1970], pp. 135–211, https://www.osti.gov/biblio/4079632.

Berendsen, H. J. C., J. P. M. Postma, W. F. van Gunsteren, A. DiNola and J. R. Haak

1984 'Molecular dynamics with coupling to an external bath', *The Journal of Chemical Physics*, 81, 8 [Oct. 1984], pp. 3684–3690, ISSN: 0021-9606, DOI: 10.1063/1.448118, eprint: https://pubs.aip.org/aip/jcp/article-pdf/81/8/3684/11352370/3684_1_online.pdf, https://doi.org/10.1063/1.448118.

Zhou, Kun and Bo Liu

2022 'Preface', in *Molecular Dynamics Simulation*, ed. by Kun Zhou and Bo Liu, Elsevier, pp. xxv–xxvii, ISBN: 978-0-12-816419-8, DOI: https://doi.org/10.1016/B978-0-12-816419-8.00015-5, https://www.sciencedirect.com/science/article/pii/B9780128164198000155.

Abraham, Mark, Andrey Alekseenko, Cathrine Bergh, Christian Blau, Eliane Briand, Mahesh Doijade, Stefan Fleischmann, Vytautas Gapsys, Gaurav Garg, Sergey Gorelov, Gilles Gouaillardet, Alan Gray, M. Eric Irrgang, Farzaneh Jalalypour, Joe Jordan, Christoph Junghans, Prashanth Kanduri, Sebastian Keller, Carsten Kutzner, Justin A. Lemkul, Magnus Lundborg, Pascal Merz, Vedran Miletić, Dmitry Morozov, Szilárd Páll, Roland Schulz, Michael Shirts, Alexey Shvetsov, Bálint Soproni, David van der Spoel, Philip Turner, Carsten Uphoff, Alessandra Villa, Sebastian Wingbermühle, Artem Zhmurov, Paul Bauer, Berk Hess and Erik Lindahl

2023 *GROMACS 2023.3 Manual*, version 2023.3, DOI: `10.5281/zenodo.10017699`, `https://doi.org/10.5281/zenodo.10017699`.

Frenkel, D. and B. Smit

2023 *Understanding Molecular Simulation: From Algorithms to Applications*, Elsevier Science, ISBN: 9780323913188, `https://books.google.it/books?id=jyipEAAAQBAJ`.

Bussi, Giovanni, Davide Donadio and Michele Parrinello

2007 'Canonical sampling through velocity rescaling', *The Journal of chemical physics*, 126, 1, p. 014101.

Gardiner, C.W.

1985 *Handbook of Stochastic Methods for Physics, Chemistry, and the Natural Sciences*, Proceedings in Life Sciences, Springer-Verlag, ISBN: 9780387113579, `https://books.google.it/books?id=cRfvAAAAMAAJ`.

Boffetta, G. and A. Vulpiani

2012 *Probabilità in Fisica: Un'introduzione*, UNITEXT, Springer Milan, ISBN: 9788847024304, `https://books.google.it/books?id=HRQaN8AuDs8C`.

Bekker, Henk, HJC Berendsen, EJ Dijkstra, S Achterop, R Vondrumen, David VANDERSPOEL, A Sijbers, H Keegstra and MKR Renardus

1993 'Gromacs-a parallel computer for molecular-dynamics simulations', in *4th International Conference on Computational Physics (PC 92)*, World Scientific Publishing, pp. 252–256.

Berendsen, Herman JC, David van der Spoel and Rudi van Drunen

1995 'GROMACS: A message-passing parallel molecular dynamics implementation', *Computer physics communications*, 91, 1-3, pp. 43–56.

Altieri, Ada, Felix Roy, Chiara Cammarota and Giulio Biroli

2021 'Properties of Equilibria and Glassy Phases of the Random Lotka-Volterra Model with Demographic Noise', *Phys. Rev. Lett.*, 126 [25 June 2021], p. 258301, DOI: `10.1103/PhysRevLett.126.258301`, `https://link.aps.org/doi/10.1103/PhysRevLett.126.258301`.

Berendsen, H. J. C., J. P. M. Postma, W. F. van Gunsteren and J. Hermans

1981 'Interaction Models for Water in Relation to Protein Hydration', in, *Intermolecular Forces: Proceedings of the Fourteenth Jerusalem Symposium on Quantum Chemistry and Biochemistry Held in Jerusalem, Israel, April 13–16, 1981*, ed. by Bernard Pullman, Springer Netherlands, Dordrecht, pp. 331–342, ISBN: 978-94-015-7658-1, DOI: `10.1007/978-94-015-7658-1_21`, `https://doi.org/10.1007/978-94-015-7658-1_21`.

Berendsen, Herman JC, J Raul Grigera and Tjerk P Straatsma

1987 'The missing term in effective pair potentials', *Journal of Physical Chemistry*, 91, 24, pp. 6269–6271.

Mahoney, Michael W. and William L. Jorgensen

2000 'A five-site model for liquid water and the reproduction of the density anomaly by rigid, nonpolarizable potential functions', *The Journal of Chemical Physics*, 112, 20 [May 2000], pp. 8910–8922, ISSN: 0021-9606, DOI: `10.1063/1.481505`, eprint: `https://pubs.aip.org/aip/jcp/article-pdf/112/20/8910/10806193/8910\_1\_online.pdf`, `https://doi.org/10.1063/1.481505`.

Jorgensen, William L, Jayaraman Chandrasekhar, Jeffry D Madura, Roger W Impey and Michael L Klein

1983 'Comparison of simple potential functions for simulating liquid water', *The Journal of chemical physics*, 79, 2, pp. 926–935.

Horn, Hans W, William C Swope, Jed W Pitera, Jeffry D Madura, Thomas J Dick, Greg L Hura and Teresa Head-Gordon

2004 'Development of an improved four-site water model for biomolecular simulations: TIP4P-Ew', *The Journal of chemical physics*, 120, 20, pp. 9665–9678.

Essmann, Ulrich, Lalith Perera, Max L Berkowitz, Tom Darden, Hsing Lee and Lee G Pedersen

1995 'A smooth particle mesh Ewald method', *The Journal of chemical physics*, 103, 19, pp. 8577–8593.

Vega, Carlos, Jose LF Abascal, MM Conde and JL Aragones

2009 'What ice can teach us about water interactions: a critical comparison of the performance of different water models', *Faraday discussions*, 141, pp. 251–276.

Vega, Carlos and Jose LF Abascal

2011 'Simulating water with rigid non-polarizable models: a general perspective', *Physical Chemistry Chemical Physics*, 13, 44, pp. 19663–19688.

Lascaris, Erik
2022 'The effect of intra-molecular bonds on the liquid–liquid critical point in modified-WAC models', *The Journal of Chemical Physics*, 157, 20, p. 204501.

Biddle, John W., Rakesh S. Singh, Evan M. Sparano, Francesco Ricci, Miguel A. González, Chantal Valeriani, José L. F. Abascal, Pablo G. Debenedetti, Mikhail A. Anisimov and Frédéric Caupin
2017 'Two-structure thermodynamics for the TIP4P/2005 model of water covering supercooled and deeply stretched regions', *The Journal of Chemical Physics*, 146, 3, p. 034502, ISSN: 0021-9606.

Abascal, José LF and Carlos Vega
2010 'Widom line and the liquid–liquid critical point for the TIP4P/2005 water model', *The Journal of Chemical Physics*, 133, 23, p. 234502.

Gallo, Paola and Mauro Rovere
2012 'Mode coupling and fragile to strong transition in supercooled TIP4P water', *The Journal of Chemical Physics*, 137, 16, p. 164503.

De Marzio, Margherita, Gaia Camisasca, Mauro Rovere and Paola Gallo
2016 'Mode coupling theory and fragile to strong transition in supercooled TIP4P/2005 water', *The Journal of chemical physics*, 144, 7, p. 074503.

Lupi, Laura, Benjamín Vázquez Ramírez and Paola Gallo
2021 'Dynamical crossover and its connection to the Widom line in supercooled TIP4P/Ice water', *The Journal of Chemical Physics*, 155, 5, p. 054502.

Soper, Alan K
2017 'The Structure of Water and Aqueous Systems', in *Experimental Methods in the Physical Sciences*, Elsevier, vol. 49, pp. 135–211.

Abraham, Mark James, Teemu Murtola, Roland Schulz, Szilárd Páll, Jeremy C. Smith, Berk Hess and Erik Lindahl
2015 'GROMACS: High performance molecular simulations through multi-level parallelism from laptops to supercomputers', *SoftwareX*, 1-2, pp. 19–25, ISSN: 2352-7110, DOI: `https://doi.org/10.1016/j.softx.2015.06.001`, `https://www.sciencedirect.com/science/article/pii/S2352711015000059`.

Poole, Peter H, Ivan Saika-Voivod and Francesco Sciortino
2005 'Density minimum and liquid–liquid phase transition', *Journal of Physics: Condensed Matter*, 17, 43 [Oct. 2005], p. L431, DOI: `10.1088/0953-8984/17/43/L01`, `https://dx.doi.org/10.1088/0953-8984/17/43/L01`.

General, Ignacio J, Eliana K Asciutto and Jeffry D Madura
2008 'Structure of aqueous sodium perchlorate solutions', *The Journal of Physical Chemistry B*, 112, 48, pp. 15417–15425.

Zhang, Yang, Antonio Faraone, William A. Kamitakahara, Kao-Hsiang Liu, Chung-Yuan Mou, Juscelino B. Leão, Sung Chang and Sow-Hsin Chen

2011b ‘Density hysteresis of heavy water confined in a nanoporous silica matrix’, *Proceedings of the National Academy of Sciences*, 108, 30 [July 2011], pp. 12206–12211, ISSN: 1091-6490, DOI: 10.1073/pnas.1100238108, http://dx.doi.org/10.1073/pnas.1100238108.